

## ABSTRACT

JOHNSTON-PECK, AARON CHARLES. Synthesis, Processing, and Characterization of Magnetic Nanoparticles for use in Bit-Patterned Media. (Under the direction of Dr. Joseph B. Tracy).

Self-assembled monolayer arrays of ferromagnetic nanoparticles (NPs) may enable future magnetic recording with areal densities in the terabits per square inch regime. A transition from conventional granular media to bit patterned media (BPM) presents numerous engineering challenges to which unsatisfactory solutions will result in read and write errors and self-erasing media. To successfully implement monolayer arrays of ferromagnetic NPs as BPM, the following are required: (1) NPs assembled into a regular pattern with circumferential periodicity and equal spacing between bits, (2) uniform magnetic response, which requires uniform volume, shape, composition, crystalline phase, magnetic anisotropy constant and orientation of the crystal axes, (3) minimal interparticle magnetostatic interactions, and (4) thermal stability for extended periods of time (resistance to superparamagnetism).

This dissertation presents a series of studies that address several of the aforementioned engineering challenges. The basis of these studies is the wet-chemical synthesis of ligand-stabilized Ni, Co, and FePt NPs. Two projects examine the synthetic control of Ni(core)/NiO(shell) and Co(core)/CoO(shell) NPs and their magnetic properties. Control of synthetic reactions conditions, specifically ligand type and concentration, dictates NP size. Subsequent magnetic characterization revealed that magnetic properties and exchange bias in particular strongly depend on NP size and oxide shell thickness. In another

project, the feasibility of self-assembly of NP monolayers via spin-casting and the implementation of analytical techniques to quantitatively characterize the structure of NP monolayers was investigated. The final two projects involve incorporation of FePt NPs into alumina thin films. The alumina thin film stabilizes monolayers of FePt NPs and facilitates sinter-free phase transformation into FePt intermetallic phases. Transmission electron microscopy characterization reveals that phase transformations from the alloy into intermetallic phases strongly depend on the NP composition.

The application of analytical, structural and magnetic characterization techniques to magnetic NPs elucidated how NP synthetic and self-assembly conditions determine the material structure and properties. These studies provide solutions and insight into overcoming superparamagnetism, controlling the structures of NPs, and fabricating periodic NP assemblies for the application of BPM.

© Copyright 2011 by Aaron Charles Johnston-Peck

All Rights Reserved

Synthesis, Processing, and Characterization of Magnetic Nanoparticles for use in Bit-  
Patterned Media

by  
Aaron Charles Johnston-Peck

A dissertation submitted to the Graduate Faculty of  
North Carolina State University  
in partial fulfillment of the  
requirements for the degree of  
Doctor of Philosophy

Materials Science and Engineering

Raleigh, North Carolina

2011

APPROVED BY:

---

Joseph B. Tracy  
Committee Chair

---

Jon-Paul Maria

---

Dr. Justin Schwartz

---

Dr. Orlin D. Velev

## **DEDICATION**

To my parents, William and Cynthia, for their never-ending love and support.

## **BIOGRAPHY**

Aaron Charles Johnston-Peck was born on October 11, 1984 to parents Cynthia Peck and William Johnston. For his undergraduate studies he attended Case Western Reserve University and graduated in 2007 with a B.S. in Materials Science and Engineering. Aaron then continued his education at North Carolina State University pursuing a doctorate under the tutelage of Dr. Joseph B. Tracy. In the fall of 2011 Aaron defended his thesis, “Synthesis, Processing, and Characterization of Magnetic Nanoparticles for use in Bit-Patterned Media” and received his Ph.D. in Materials Science and Engineering from North Carolina State University. Following graduation, Aaron became a post-doctoral researcher in the field of transmission electron microscopy.

## ACKNOWLEDGMENTS

I sincerely thank my advisor Dr. Joseph B. Tracy for introducing me to the fascinating world of magnetic nanoparticles and helping me grow as a researcher. His inquisitive nature provided me with an endless stream of ideas for me to pursue and helped me formulate my own hypotheses for routes of inquiry. His flexible nature allowed me to pursue my personal research interests in the field of transmission electron microscopy even if they were not central to his research goals and ambitions, for which I am grateful.

Several research groups at NCSU were very welcoming and generous with both their time and resources. I thank Dr. Jon-Paul Maria and his graduate students, Elizabeth Paisley, Peter Lam, David Hook, Michelle Casper, Hasan Akyildiz, and Nicole Estrich who provided training and assistance to me in the lab. Having access to Dr. Maria's suite of deposition chambers and characterization tools were critical in realizing my research goals. I thank Dr. Gregory Parsons and his post-doctoral researchers, Dr. Giovanna Scarel and Dr. Christopher Oldham, for providing me samples and the benefit of their group's expertise in atomic layer deposition. I'm very grateful to have worked with Dr. Thomas Rawdanowicz who helped me develop as an electron microscopist. His dedication and enthusiasm as a lab manager kept the transmission electron microscope facilities in great working order and as a teacher he always had useful dialogue and suggestions on all things EM related.

I thank, former groupmate, Dr. Junwei Wang for introducing to nanoparticle chemistry and my current groupmates, Peter Krommenhoek, Mehmet Sarac, and Wei-Chen "Ivy" Wu for their support and insightful conversations on research. To my friends at

NCSU, thank you for making my time here all that more enjoyable. Finally, I thank my family for their seemingly infinite encouragement and love.

## TABLE OF CONTENTS

List of Tables .....	vii
List of Figures .....	viii
Chapter 1. Bit-Patterned Media .....	1
1.1 Introduction to Magnetic Storage Media .....	1
1.2 Introduction to Bit-Pattern Media .....	3
1.3 Technological Challenges of Bit-Patterned Media .....	4
1.4 Nanoparticles as a Bit-Patterned Media .....	5
1.5 Thesis Goals and Overview .....	8
REFERENCES .....	9
Chapter 2. Introduction to Magnetic Materials .....	11
2.1 Origin of Magnetism .....	11
2.2 Magnetic Anisotropy .....	14
2.2.1 Magnetocrystalline Anisotropy .....	14
2.2.2 Exchange Anisotropy .....	15
2.3 Superparamagnetism .....	16
2.4 Single Domain Limit .....	17
2.5 Magnetic Measurements .....	19
2.5.1 Temperature Dependent Measurements .....	19
2.5.2 Field-Dependent Measurements .....	20
2.6 Stoner-Wohlfarth Model .....	21
2.7 Magnetic Materials .....	23
REFERENCES .....	26
Chapter 3. Self-Assembly of Nanoparticles .....	28
3.1 Forces Guiding Self-Assembly .....	28
3.2 Self-Assembly of Nanoparticle Monolayers .....	32
REFERENCES .....	36
Chapter 4. Thin Film Growth .....	38
4.1 Atomic Layer Deposition .....	38
4.2 Growth of Al <sub>2</sub> O <sub>3</sub> by Atomic Layer Deposition .....	41
4.3 Atomic Layer Deposition of Al <sub>2</sub> O <sub>3</sub> on Nanoparticles .....	42
4.4 Pulsed Layer Deposition .....	42
4.5 Pulsed Layer Deposition Coating of Nanomaterials .....	43
REFERENCES .....	44
Chapter 5. Transmission Electron Microscopy .....	46
5.1 Transmission Electron Microscopy .....	46
5.1.1 Imaging Modes in Transmission Electron Microscopy .....	47

5.2 Scanning Transmission Electron Microscopy .....	49
5.2.1 Imaging Modes in Scanning Transmission Electron Microscopy .....	50
REFERENCES .....	53
Chapter 6. Size Controlled Synthesis of Cobalt Nanoparticles .....	54
6.1 Introduction.....	54
6.2 Methods.....	55
6.2.1 Nanoparticle Synthesis.....	56
6.2.2 Structural Characterization .....	56
6.2.3 Magnetic Characterization.....	57
6.3 Results and Discussions.....	58
6.3.1 Structural Properties and Cobalt Nanoparticle Growth Mechanism.....	58
6.3.2 Magnetic Properties .....	62
6.4 Conclusions.....	68
REFERENCES .....	70
Chapter 7. Synthesis and Structural and Magnetic Characterization of Ni(core)/NiO(shell) Nanoparticles .....	72
7.1 Motivation.....	72
7.2 Manuscript Reprint .....	73
Chapter 8. Formation and Grain Analysis of Spin-Cast Magnetic Nanoparticle Monolayers	88
8.1 Motivation.....	88
8.2 Manuscript Reprint .....	89
8.3 Addendum.....	108
Chapter 9. Sinter-Free Phase Conversion and Scanning Transmission Electron Microscopy of FePt Nanoparticle Monolayers .....	109
9.1 Motivation.....	109
9.2 Manuscript Reprint .....	110
9.3 Addendum.....	127
9.3.1 Methods.....	127
9.3.2 Results and Discussion .....	127
9.4 Conclusions.....	130
9.5 Acknowledgements.....	130
REFERENCES.....	132
Chapter 10. Phase Transformation of Alumina-Coated FePt Nanoparticles .....	133
10.1 Motivation.....	133
10.2 Abstract.....	134
10.3 Introduction.....	134
10.4. Experimental Methods.....	136
10.5 Results and Discussion .....	138

10.6 Conclusions.....	143
10.7 Acknowledgments.....	144
REFERNCES.....	145
Chapter 11. Conclusions and Recommendations for Further Work.....	148
11.1 Summary of Conclusions.....	148
11.2 Recommendations for Further Works.....	149

## LIST OF TABLES

<b>Table 2.1.</b> Magnetic properties of select transition metals and metal oxides that are of interest for use in nanotechnology applications including bit-patterned media. The critical diameter is the minimal stable grain size, $(60k_B T/K)^{1/3}$ ( $\tau=10$ years). <sup>22</sup> Except where noted, all data are from reference. <sup>23</sup> .....	33
<b>Table 6.1.</b> Magnetic and structural properties of cobalt nanoparticles. The saturation magnetization (MS) values listed are those after accounting for the linear susceptibility of CoO. *Indicates this was a calculated value, rather than a value measured by SQUID.....	76
<b>Table 7.1.</b> Average Ni Core Diameter and NiO Shell Thickness .....	84
<b>Table 7.2.</b> Saturation Magnetization and Coercivity at 2.5 K with 50 kOE or Zero-field Cooling.....	86
<b>Table 8.1.</b> Summary of Nanoparticle Sizes and Circularities .....	102

## LIST OF FIGURES

### Chapter 2

**Figure 1.** Schematic temperature dependent-magnetization (M vs. T) curve of a ferromagnetic material .....28

**Figure 2.** Schematic field dependent magnetization (M vs. H) curve of a ferromagnetic material .....29

### Chapter 3

**Figure 1.** Schematic of an entropy-driven depletion region.....40

**Figure 2.** Schematic of ferromagnetic nanoparticles and their associated dipoles arranging themselves into (a) rings and (b) chains, thereby reducing their magnetostatic energy .....43

### Chapter 5

**Figure 1.** Simulated damped contrast transfer function .....57

**Figure 2.** Schematic of overlapping diffraction discs on an high-angle annular dark field detector.....59

### Chapter 6

**Figure 1.** Bright-field TEM images of Co nanoparticles synthesized using (a) docosanoic acid, (b) dodecanoic acid, and (c) hexanoic acid .....67

**Figure 2.** Representative selected area electron diffraction pattern of  $\epsilon$ -Co nanoparticles.....67

**Figure 3.** HRTEM images of Co nanoparticles synthesized using (a) docosanoic acid, (b) dodecanoic acid, and (c) hexanoic acid .....68

**Figure 4.** Schematic representation of LaMer modeled growth of nanoparticles as a function of a supersaturation. The reactivity of the coordinating ligands determines the extent of supersaturation. As the ligand chain length decreases, the monomer reactivity and supersaturation increases .....70

**Figure 5.** Zero-field cooled magnetization as a function of temperature for Co nanoparticles synthesized using carboxylic acids with different chain lengths .....72

**Figure 6.** Zero- and field-cooled magnetization as a function of field measured at 5 K .....75

**Figure 7.** Magnetization as a function of field measured at 300 K.....76

## Chapter 7

**Figure 1.** TEM images of Ni nanoparticles: (top row) native samples; (bottom row) oxidized samples.....83

**Figure 2.**  $M$  vs  $T$  after cooling in zero field for native and oxidized Ni(core)/NiO(shell) NPs. The inset (bottom panel) shows greater detail of the low-temperature region. Labels indicate  $T_B$  for each sample .....85

**Figure 3.**  $M$  vs  $H$  at 2.5 K for native and oxidized Ni(core)/NiO(shell) NPs after cooling from room temperature in 50 kOe field (FC) or zero field (ZFC). Insets show greater detail of the same measurements.....86

**Figure 4.** Ni core-size dependence of the coercivity (zero-field cooled).....86

**Figure 5.** Dependence of  $T_B$  on the Ni core volume. Inset shows the same plot, omitting the two data points for samples with the largest volumes (Ni 5 and Ni 5-ox). Linear fits are shown in green .....87

**Figure S-1.** Photographs of the poly(lauryl methacrylate) cross-linked with ethylene glycol dimethacrylate matrix for SQUID magnetometry measurements: (left) with no nanoparticles added and (right) containing Ni(core)/NiO(shell) nanoparticles .....90

**Figure S-2.** HRTEM images of the native and oxidized Ni nanoparticles .....91

**Figure S-3.** Selected-area electron diffraction of the native and oxidized Ni nanoparticles ..92

**Figure S-4.** Histograms showing the distribution of total  $2(r_{Ni} + t_{NiO})$  nanoparticle diameters measured by TEM for each sample with native oxidation .....93

## Chapter 8

**Figure 1.** (a) TEM image of Monolayer 1 of Ni nanoparticles (7.0 nm diameter) and its (b) color-coded orientation map .....100

**Figure 2.** Defect map of part of Monolayer 1, where defects are colored according to their coordination numbers: 4 (green), 5 (orange), 7 (cyan), 8 (magenta). Colored adjacent nanoparticles signify the presence of a defect. Examples of each type of defect have been highlighted, “V” (vacancy), “I” (interstitial), and “D” (dislocation). The oval surrounds a string of dislocations, demarcating a grain boundary .....100

**Figure 3.** (a) TEM image of Monolayer 2 of FePt nanoparticles (7.2 nm diameter) and its color-coded (b) defect and (c) orientation maps and (d) Delaunay triangulation mesh. Inset (panel a): Fast Fourier transform (FFT) of the image.....101

**Figure 4.** (a) TEM image of Monolayer 3 of FePt nanoparticles (7.2 nm diameter) and its (b) color-coded orientation map. Inset (panel a): Fast Fourier transform (FFT) of the image....101

**Figure 5.** TEM images of (a) Monolayer 4, a disordered monolayer of spherical FePt nanoparticles (4.2 nm diameter), and (b) Monolayer 5, a disordered monolayer of irregularly-shaped FePt nanoparticles (6.4 nm diameter). Color-coded defect maps for (a) and (b) are shown in (c) and (d), respectively. Insets (panels a,b): Fast Fourier transform (FFT) of the image.....102

**Figure S-1.** Comparison of orientation maps for Monolayer 2 generated from Figure 3a (a) using a fast Fourier transform (FFT) mask in the process of converting the raw image to a binary image, and (b) without using the FFT mask in the conversion process. ....106

**Figure S-2.** Radial distribution function of Monolayer 2 (calculated from Figure 3a).....106

**Figure S-3.** Whole defect map of Monolayer 1, where defects are colored according to their coordination numbers: 4 (green), 5 (orange), 7 (cyan), 8 (magenta). Colored adjacent nanoparticles signify the presence of a defect. Examples of each type of defect have been highlighted, “V” (vacancy), “I” (interstitial), and “D” (dislocation). The oval surrounds a string of dislocations, demarcating a grain boundary .....107

**Figure S-4.** Defect map of Monolayer 3 of FePt nanoparticles (7.2 nm diameter) corresponding to the TEM image shown in Figure 4a of the main text .....108

**Figure S-5.** TEM image of FePt nanoparticles (6.4 nm diameter) used to synthesize Monolayer 5 (Figure 5b).....108

**Figure S-6.** TEM image of FePt nanoparticles (7.2 nm diameter) used to synthesize the close-packed Monolayers 2-3 (Figures 3-4) .....109

**Figure S-7.** TEM image of a monolayer of Ni nanoparticles (7.0 nm diameter) covering approximately  $21 \mu\text{m}^2$  .....110

## Chapter 9

**Figure 1.** Models of the unit cells for the different phases of FePt: (a) A1 alloy, face-centered cubic, (b) L1<sub>0</sub> FePt intermetallic, face-centered tetragonal, and (c) L1<sub>2</sub> FePt<sub>3</sub> intermetallic, face-centered cubic .....120

<b>Figure 2.</b> TEM images (common scale bar) of monolayers of 4 nm FePt NPs: (a) with an Al <sub>2</sub> O <sub>3</sub> layer, before annealing, (b) with an Al <sub>2</sub> O <sub>3</sub> layer, after annealing (5 h at 730 °C + 3 h at 600 °C), (c) without an Al <sub>2</sub> O <sub>3</sub> layer, after annealing (700 °C for 15 min), and (d) Al <sub>2</sub> O <sub>3</sub> -coated monolayer of 6 nm FePt NPs that sintered after heating at 900 °C for 1 h. Insets (panels a,b): SAED .....	122
<b>Figure 3.</b> TEM images of Al <sub>2</sub> O <sub>3</sub> -coated monolayers of (a) 5 nm and (b) 6 nm FePt NPs after annealing (5 h at 730 °C + 3 h at 600 °C). Insets (panels a,b): SAED .....	122
<b>Figure 4.</b> TEM images of FePt NPs with diameters of (a) 5 nm, before annealing, (b) 5 nm, after annealing with Al <sub>2</sub> O <sub>3</sub> coating, (c) 6 nm, before annealing, and (d) 6 nm, after annealing with Al <sub>2</sub> O <sub>3</sub> coating .....	123
<b>Figure 5.</b> XRD of an Al <sub>2</sub> O <sub>3</sub> -coated monolayer of 6 nm FePt NPs after annealing for 5 h at 730 °C + 3 h at 600 °C that converted into the L1 <sub>0</sub> phase .....	123
<b>Figure 6.</b> Filtered HAADF-STEM images with corresponding Fourier transforms (before noise filtering) and cartoons illustrating the ordering: (a) L1 <sub>2</sub> -FePt <sub>3</sub> NP from the 4 nm sample, (b) L1 <sub>2</sub> -FePt <sub>3</sub> NP from the 5 nm sample, and (c) L1 <sub>0</sub> -FePt NP from the 6 nm sample. Each NP was imaged along the [001] zone axis .....	123
<b>Figure 7.</b> Filtered HAADF-STEM images with corresponding Fourier transforms (before noise filtering) of (a,c) an A1 NP from the 4 nm sample, imaged along the [011] zone axis, and (b,d) a mixed-phase L1 <sub>0</sub> -FePt/L1 <sub>2</sub> -FePt <sub>3</sub> NP from the 6 nm sample, imaged along the [101] zone axis. Intensity profiles acquired across the NP in panel (b) at three different points show the transition from the L1 <sub>2</sub> to L1 <sub>0</sub> phase.....	124
<b>Figure 8.</b> (a–c) Filtered HAADF-STEM images of 6 nm FePt NPs containing different proportions of the L1 <sub>0</sub> and L1 <sub>2</sub> phases, imaged along the [001] zone axis. Fourier transforms before noise filtering are shown below each NP: (d–i) selected regions corresponding to the (d,f,h) blue squares that indicate the L1 <sub>2</sub> phase and to the (e,g,i) red squares that indicate the L1 <sub>0</sub> phase; (j–l) for each entire NP (cropped on the top and bottom). Structure models, (m,o) simulated projected potentials, and (n,p) simulated HAADF-STEM images along the [001] zone axis for the L1 <sub>0</sub> -FePt and the L1 <sub>2</sub> -FePt <sub>3</sub> phases are provided for comparison .....	125
<b>Figure S-1.</b> Representative TEM image of 4.2 nm FePt nanoparticles.....	127
<b>Figure S-2.</b> Representative TEM image of 4.9 nm FePt nanoparticles.....	128
<b>Figure S-3.</b> Representative TEM image of 5.9 nm FePt nanoparticles.....	128
<b>Figure S-4.</b> EDS spectrum for 4.2 nm FePt nanoparticles .....	129

<b>Figure S-5.</b> EDS spectrum for 4.9 nm FePt nanoparticles .....	130
<b>Figure S-6.</b> EDS spectrum for 5.9 nm FePt nanoparticles .....	131
<b>Figure S-7.</b> TEM image of a spin cast array of a partial multilayer of 4.2 nm diameter FePt nanoparticles .....	131
<b>Figure S-8.</b> HAADF-STEM images used in Figure 6, before noise filtering .....	132
<b>Figure S-9.</b> HAADF-STEM images used in Figure 7, before noise filtering .....	132
<b>Figure S-10.</b> HAADF-STEM images used in Figure 8, before noise filtering .....	133
<b>Figure S-11.</b> (a-b) Filtered and (c-d) the original, unfiltered HAADF-STEM images showing the presence of the FePt <sub>3</sub> phase forming on the edges of the nanoparticles .....	134
<b>Figure 9.</b> A plot of nanoparticle diameter versus composition. The data points in red re those nanoparticles that contain the Pt-rich L <sub>1</sub> <sub>2</sub> phase, while those in black could not have their phase identified because they were not oriented on a zone axis.....	137
<b>Figure 10.</b> Atomic resolution HAADF-STEM images of FePt nanoparticles that contain the Pt-rich L <sub>1</sub> <sub>2</sub> phase. The individual nanoparticle composition is listed with each image .....	137
 <b>Chapter 10</b>	
<b>Figure 1.</b> TEM images (common scale bar) of monolayers of FePt NPs: (a) before deposition of Al <sub>2</sub> O <sub>3</sub> , (b) with an Al <sub>2</sub> O <sub>3</sub> layer, before annealing, (c) with an Al <sub>2</sub> O <sub>3</sub> layer, after annealing ....	146
<b>Figure 2.</b> HAADF-STEM images (common scale bar) of FePt NPs after annealing: (a) cuboctahedron along [001], (b) truncated octahedron along [001], and (c) cuboctahedron along [101]. An antiphase boundary (planar defect) is indicated in the image, and surface steps are also present.....	148
<b>Figure 3.</b> HAADF-STEM image with [001] zone axis of an FePt NP and line intensity profiles from rows of atomic columns parallel to the NP edge, beginning with the outermost row: (1) Pt atomic columns only, (2) alternating Fe and Pt atomic columns, containing a high density of Pt antisite defects, (3) Pt atomic columns only, and (4) alternating Fe and Pt atomic columns with few or no Pt antisite defects. The schematic shows the projection of the L <sub>1</sub> <sub>2</sub> FePt structure along the [001] zone axis without the presence of any defects and indicates the anticipated pattern of atomic columns in the line intensity profiles .....	151

# CHAPTER 1

## **Bit-Patterned Media**

### **1.1 Introduction to Magnetic Storage Media**

Hard disk drives (HDDs) used in devices such as personal computers are possibly the most recognizable and widely implemented form of magnetic storage. Magnetic storage utilizes magnetization patterns in magnetizable media to store data. In digital devices, two stable magnetic states, specifically the positive and negative remnant magnetized states, are used to encode the data in the binary numeral system of 0's and 1's. The first HDD became commercially available in 1956 from IBM, since then the capacity and areal density have dramatically increased while the access time, power consumption, and price have decreased drastically. To continue this trend of ever increasing areal density and associated benefits (cost reductions, faster access times, etc.) intrinsic limitations of the architecture and materials used in the fabrication of HDDs must be addressed.

HDDs consist of a platter made from a non-magnetic material that is supported on a spindle whose function is to spin the platter. The platter is coated with a thin polycrystalline film of magnetic material, in which data is stored. Read and write heads move closely over the surface of the platter and detect and modify the magnetization of the polycrystalline film. Data is encoded by orienting magnetic moments of the ferromagnetic material along specific directions. Therefore the data is stored as binary bits as a function of changes in magnetization direction.

The ferromagnetic polycrystalline film is comprised of non-uniform grains that vary in size and crystallographic orientation. Bits are comprised of assemblies of 50-100 of these grains. The magnetic field of the write head orients the magnetic moments within the individual grains toward the applied field direction, such that the average remnant magnetization within a magnetic bit points along one of two possible directions. The boundary between each bit does not have a straight-line boundary but rather follows grain boundaries in a transition that only approximates a discrete straight line. This results in jitter (modulated noise).<sup>1</sup> Therefore, increasing storage density by decreasing the number of grains that make up a single magnetic bit will increase noise levels because the boundary roughness becomes a greater fraction of the bit length. Consequently, the signal to noise ratio of each magnetic transition would increase preventing accurate readback and therefore is not a feasible option. An alternative approach to increase the storage density necessitates decreasing the grain size. This route has been pursued vigorously, and present grain sizes are now approximately 8-10 nm in diameter. Further reduction in grain size is not an option due to thermally induced instabilities in the magnetization of the individual grains, an effect known as superparamagnetism, whose onset is a function of volume and the magnetic anisotropy of a material. Instabilities of the magnetization directions are unacceptable because this results in data corruption.

To reiterate two significant challenges are posed that inhibit the further increases in storage density of HDDs. The current format of the magnetic media is inherently inefficient due to the fabrication process that produces a random granular film requiring collective averaging of several grains to get predictable and uniform magnetic response. The second is

an intrinsic material property limitation that becomes prevalent as grain sizes are reduced to the nanoscale. This means the architecture of magnetic storage needs to be redesigned as well as the implementation of more thermally stable magnetic materials.

## **1.2 Introduction to Bit-Pattern Media**

Bit-patterned media (BPM) using high magnetic anisotropy materials offers a solution to both these problems. The idea of using discrete ferromagnetic entities in magnetic media and specifically BPM was suggested in the early 1990's.<sup>2-4</sup> BPM consists of a periodic array of discrete single-domain magnetic elements where each element functions as its own bit. Through appropriate material selection each magnetic element can have a uniaxial magnetic anisotropy. This reduces the number of possible magnetization directions to two, for example up and down orthogonal to the plane of the substrate, which could represent 1 and 0.<sup>5</sup> This format has numerous advantages over conventional granular media. First, in some regards the write process is simpler because the location and shape of the magnetic bit is predefined, and only the magnetization direction needs assigning. Second, transition noise is eliminated because the bits are now defined by the discrete isolated physical location of the magnetic elements and not by the contacting irregular grain boundaries in a thin film. Third, very high areal densities are achievable because the onset of superparamagnetism is determined by the volume and anisotropy of the magnetic element representing the entire bit, rather than by individual grains that comprised the bit. Therefore, a bit can be represented by a single entity measuring several nanometers in each dimension rather than 50-100 grains

measuring several nanometers in each dimension. In BPM, bits would be smaller and could be packed more densely, allowing areal densities above 1 Terabit/in<sup>2</sup>.<sup>2-4</sup>

### 1.3 Technological Challenges of Bit-Patterned Media

BPM is a promising solution to overcome the insurmountable limitations of continuous granular magnetic media. The paradigm shift of moving from granular to discrete media presents unique challenges that must be addressed before BPM can be implemented. By switching storage formats from continuous to BPD media, physical limits are traded for engineering challenges.

An important design criterion for any storage media is to minimize the occurrence of read and write errors. Understanding the origins of these errors in BPM will identify the engineering challenges of BPM. In BPM, the bits are now physically defined by the fabrication process, whereas in conventional media, the bit positions are defined by the head position at the time when the write field is applied. This difference will manifest itself in the form of many engineering challenges because during the writing process the applied field must be synchronized with the physical location of the elements.<sup>6</sup> During the read process several sources of noise exist. These sources are due to variations in (1) bit spacing, (2) bit diameter, thickness, and shape, and (3) saturation magnetization this corresponds to a signal to noise ratio (SNR) of

$$SNR = \frac{1}{(\pi^2 - 7)(\sigma_{s_D}/s_D)^2 + (\sigma_D/D)^2} \quad (1.1)$$

where  $\sigma_{s_D}/s_D$  and  $\sigma_D/D$  are the variations in bit spacing and size, and which are treated as Gaussians functions that are considered statistically independent.<sup>5</sup> During the write process, as the write-head travels over the bits only during a small window of time will the intended bit be properly recorded. Deviations from this write window will result in the bit not being properly written or another bit being written instead. As a practical issue one cannot adjust the timing individually for each bit but rather an average time between dots must be defined,<sup>7</sup> therefore necessitating periodic control of bit locations. Write-in errors are a result of (1) variations in dot spacing, (2) variations in switching field (switching field distributions of the individual bits cause variations of the writing position or times which can lead to written-in errors due to lack of synchronization due anisotropy field variations for single domain particles following the model of coherent rotation), (3) if the required switching field is larger than what the write head can apply, and (4) bit interactions (magnetostatics) changing the required switching field.<sup>6-12</sup>

These factors impose several requirements that need to be satisfied when fabricating the media. For an ideal case: First, the magnetic bits must be assembled into a regular pattern with circumferential periodicity with equal spacing between bits. Second, the magnetic bits should have a uniaxial magnetocrystalline anisotropy axis. Third, the magnetic bits should have uniform magnetic response meaning that the volume, shape, composition, crystalline phase, magnetic anisotropy constant and orientation of the crystal axes are the same. Forth, interparticle magnetostatic interactions should be eliminated. In practice, however it is impractical (*e.g.* eliminating all magnetostatic interactions would limit the areal density) and unnecessary, as small levels deviations can be present without introducing

unacceptable levels of writing and reading errors. Fifth, the magnetic bits are thermally stable for extended periods of time.

#### **1.4 Nanoparticles as a Bit-Patterned Media**

Several techniques have been considered for BPM fabrication including lithography (optical, X-ray, and electron beam) and templates. Direct production of BPM by lithography depending on the specific technique used would suffer from one or multiple of the following limitations: expense, resolution limitations with respect to patterning features in the nanometer size range, and long write times. Templating or patterning approaches using diblock copolymers or anodic anodized alumina while cost effective tend to have issues with achieving precise and reproducible long range ordering, and structures with circular geometry has not been reported yet. Using lithography to create a master and then stamp replicas, much like how CDs are produced is another approach that shows promise but may be difficult to implement due to engineering requirements associated with the materials used in magnetic media and the feature size needed in BPM.<sup>13</sup>

Nanoparticles (NPs) provide an exciting and promising opportunity to address the engineering challenges associated with BPM. Self-assembled monolayer arrays of NPs could be implemented as the recoding media where each NP then functions as a bit. NPs have the ability to self-assemble into periodic monolayer structures. Several techniques have been reported to successfully fabricate monolayers structures with long range ordering including Langmuir-Blodgett,<sup>13</sup> dip-coating,<sup>14</sup> spin coating,<sup>15</sup> and assembly at liquid-air interfaces with no lateral pressures applied.<sup>16</sup> Additionally, the presence of ligands on the NP surface

enables engineering of the assembly process and facilitates control over parameters including the packing configuration and interparticle spacing.<sup>17</sup> Size tunable NPs can be achieved through wet-chemical synthesis with narrow size distributions ( $\leq 5\%$ ).<sup>18</sup> NP materials with applications in magnetic storage such as Co<sup>19</sup> and high-magnetic-anisotropy materials including FePt<sup>20</sup> and CoPt<sup>18</sup> have been synthesized.

While immense progress in the field of NP synthesis, assembly, and magnetism has been made, significant hurdles still exist before NPs can be used in BPM. Assembly of NPs into monolayers on the wafer scale remains a challenge. While reports of patterning entire substrates with NPs exists<sup>21</sup> these reported assemblies are closed packed in geometry and contain imperfections such as voids, point and line defects, multiple layers, and domain boundaries. Furthermore, the magnetic easy axis of the NPs when assembled through these techniques is random rather than lying along a preferred direction. Ferromagnetic NPs are susceptible to superparamagnetism. Therefore, there is a lower size limit for NPs, before they are no longer useful for BPM. To address this problem, materials must be used that have very high magnetocrystalline anisotropy such as the L<sub>10</sub> phases of FePt or CoPt. Alternatively, exchange bias can be used to enhance anisotropy thus preventing the onset of superparamagnetism.<sup>22,23</sup> In both cases, several engineering challenges exist. High-anisotropy L<sub>10</sub> NPs they are typically synthesized in the A1 phase rather than the intermetallic phase and must be thermally treated for conversion into the intermetallic phase, which can induce sintering between NPs and a loss of their monodisperse size distribution. To implement exchange bias requires incorporation of an antiferromagnetic material.

In summary, NPs offer great promise for BPM, but additional research is needed to overcome (1) the onset of superparamagnetism, (2) uniform easy axis alignment, (3) synthetic control of NPs, and (4) scale and quality of assembly into monolayers.

## **1. 5 Thesis Goals and Overview**

This thesis covers a series of studies that deal with the synthesis, assembly, and engineering of magnetic NPs with the explicate goal of their incorporation into magnetic storage media. Specifically, the studies here attempt to address or provide solutions to overcoming the superparamagnetic limit, synthetic control of nanoparticle properties, studies of exchange bias, as well as the self assembly of NPs.

Following this chapter on the motivations for this thesis are chapters introducing the basic science of magnetism, assembly of NPs, film growth, and characterization tools. Each project will then be presented in a self-contained chapter that covers pertinent background information, experimental methodology, results, discussions, and conclusions. Two projects examine the synthetic control of Ni and Co NPs and the subsequent control of the magnetic properties. Next a project investigates the feasibility of the formation of NP monolayers by spin-casting. Following these are two projects on the incorporation of NPs and thin films, a relatively unexplored field that holds great potential. Monolayers or multilayers of NPs incorporated into matrices provides many unique properties including extrinsic control of the NPs, high temperature stability, and many other applications not yet realized. Finally, the report will conclude with a summary of the findings and their significance.

## REFERENCES

- <sup>1</sup> C. Jianping, H. J. Richter, W. Li-Ping, and V. B. Minuhin, *Magnetics, IEEE Transactions on* **35**, 2727 (1999).
- <sup>2</sup> T. M. Whitney, J. S. Jiang, P. C. Searson, and C. L. Chien, *Science* **261**, 1316 (1993).
- <sup>3</sup> S. Y. Chou, M. S. Wei, P. R. Krauss, and P. B. Fischer, *Journal of Applied Physics* **76**, 6673 (1994).
- <sup>4</sup> R. L. White, R. M. H. New, and R. F. W. Pease, *Ieee Transactions on Magnetics* **33**, 990 (1997).
- <sup>5</sup> C. Ross, *Annual Review of Materials Research* **31**, 203 (2001).
- <sup>6</sup> H. J. Richter, A. Y. Dobin, O. Heinonen, K. Z. Gao, R. J. M. Van der Veerdonk, R. T. Lynch, J. Xue, D. Weller, P. Asselin, M. F. Erden, and R. M. Brockie, *IEEE Transactions on Magnetics* **42**, 2255 (2006).
- <sup>7</sup> H. J. Richter, A. Y. Dobin, R. T. Lynch, D. Weller, R. M. Brockie, O. Heinonen, K. Z. Gao, J. Xue, R. J. M. van der Veerdonk, P. Asselin, and M. F. Erden, *Applied Physics Letters* **88**, 222512 (2006).
- <sup>8</sup> M. Ranjbar, T. K. G, S. N. Piramanayagam, K. P. Tan, R. Sbiaa, S. K. Wong, and T. C. Chong, *Journal of Physics D: Applied Physics* **44**, 265005 (2011).
- <sup>9</sup> S. Yuanjing, P. W. Nutter, B. D. Belle, and J. J. Miles, *Magnetics, IEEE Transactions on* **46**, 1755 (2010).
- <sup>10</sup> P. Krone, D. Makarov, T. Schrefl, and M. Albrecht, *Journal of Applied Physics* **106**, 103913 (2009).
- <sup>11</sup> J. Kalezhi, J. J. Miles, and B. D. Belle, *Magnetics, IEEE Transactions on* **45**, 3531 (2009).
- <sup>12</sup> J. Kalezhi, B. D. Belle, and J. J. Miles, *Magnetics, IEEE Transactions on* **46**, 3752 (2010).
- <sup>13</sup> B. D. Terris and T. Thomson, *Journal of Physics D: Applied Physics* **38**, R199 (2005).
- <sup>14</sup> D. K. Lee, Y. H. Kim, C. W. Kim, H. G. Cha, and Y. S. Kang, *Journal of Physical Chemistry B* **111**, 9288 (2007).

- 15 T. S. Yoon, J. H. Oh, S. H. Park, V. Kim, B. G. Jung, S. H. Min, J. Park, T. Hyeon,  
and K. B. Kim, *Advanced Functional Materials* **14**, 1062 (2004).
- 16 S. Coe-Sullivan, J. S. Steckel, W. K. Woo, M. G. Bawendi, and V. Bulovic,  
*Advanced Functional Materials* **15**, 1117 (2005).
- 17 T. P. Bigioni, X. M. Lin, T. T. Nguyen, E. I. Corwin, T. A. Witten, and H. M. Jaeger,  
*Nature Materials* **5**, 265 (2006).
- 18 S. Sun, C. B. Murray, D. Weller, L. Folks, and A. Moser, *Science* **287**, 1989 (2000).
- 19 C. B. Murray, C. R. Kagan, and M. G. Bawendi, *Annual Review of Materials Science*  
**30**, 545 (2000).
- 20 V. F. Puntès, K. M. Krishnan, and A. P. Alivisatos, *Science* **291**, 2115 (2001).
- 21 J. I. Park and J. Cheon, *Journal of the American Chemical Society* **123**, 5743 (2001).
- 22 A. Desireddy, C. P. Joshi, M. Sestak, S. Little, S. Kumar, N. J. Podraza, S. Marsillac,  
R. W. Collins, and T. P. Bigioni, *Thin Solid Films* **519**, 6077 (2011).
- 23 M. N. Martin and S. K. Eah, *Materials Research Society Symposium Proceedings*  
**1113**, F03 (2009).

## CHAPTER 2

### **Introduction to Magnetic Materials**

#### **2.1 Origin of Magnetism**

The magnetic properties of a material are dictated by electron motion. Even though the nuclear magnetic moments of the nuclei exist, in a material the magnitude of those moments are negligible by comparison to the electrons' magnetic moments and can be neglected for the purpose of discussing and understanding the macroscopic magnetic properties of bulk materials. Electrons both move around a nucleus (orbital angular momentum) and exhibit spin (spin angular momentum). The manner in which the electrons and their associated momentums interact and align with respect to one another defines the magnetic response. Diamagnetism occurs when all the magnetic moments of all the electrons are oriented such that the vector sum of the magnetic moments is zero. For instance, filled atomic subshells will have no net moment because the electron pairs have opposite spin (Pauli exclusion principle) and the net orbital motion is also zero. Therefore every material has a diamagnetic component which manifests as a magnetic moment opposing the applied field (a linear negative magnetic susceptibility) because an applied field will increase the orbital magnetic moments of those electrons aligned opposite the field, and decreases the ones aligned parallel to the field, as described by Lenz's Law.

However if unpaired electrons exist the diamagnetic component is negligible and the vector sum of all the moments is nonzero, the material is then para-, ferri-, ferro-, or

antiferromagnetic. If the unpaired electrons do not interact, when an external magnetic field is applied the magnetic moments align in the same direction as the applied field (a positive linear magnetic susceptibility), a response known as paramagnetism. If the unpaired electrons interact, the material is ferri-, ferro-, or antiferromagnetic. Unique to these forms of magnetism is the existence of spontaneous ordering of the magnetic moments in a solid below a critical temperature, for both ferro- and ferrimagnets, it is known as the Curie temperature ( $T_C$ ) and for antiferromagnets is the Néel temperature ( $T_N$ ). In the case of ferromagnetism, the spins align parallel to one another, and their moments add. If the spins have antiparallel alignment and their moments cancel, then the material is antiferromagnetic. If there are two different sublattices, where the magnitudes of the opposing moments are different, then the material is ferrimagnetic. Above the Néel and Curie temperatures, magnetic ordering vanishes and the materials become paramagnetic.

This collective response of the moments is the result of exchange interactions. A direct exchange interaction occurs when electron orbitals overlap. This interaction is a quantum mechanical effect between sub-atomic particles, in this case electrons, which influences magnetic behavior.

A model can be assumed of two unpaired electrons on neighboring atoms with wavefunctions  $\psi_a(\mathbf{r}_1)$  and  $\psi_b(\mathbf{r}_2)$ , where  $\mathbf{r}_1$  and  $\mathbf{r}_2$  indicate their positions. Because electrons are fermions and cannot occupy the same quantum state an antisymmetric wave function will be produced. Therefore either a singlet state (antisymmetric spin with a symmetric wave function) or triplet state (symmetric spin with an antisymmetric wave function) will form.

The corresponding wavefunctions and energies are:

$$\Psi_S = \frac{1}{\sqrt{2}} [\psi_a(\mathbf{r}_1)\psi_b(\mathbf{r}_2) + \psi_a(\mathbf{r}_2)\psi_b(\mathbf{r}_1)] \chi_S \quad (2.1)$$

$$\Psi_T = \frac{1}{\sqrt{2}} [\psi_a(\mathbf{r}_1)\psi_b(\mathbf{r}_2) - \psi_a(\mathbf{r}_2)\psi_b(\mathbf{r}_1)] \chi_T \quad (2.2)$$

$$E_S = \int \Psi_S^* \widehat{H} \Psi_S d\mathbf{r}_1 d\mathbf{r}_2 \quad (2.3)$$

$$E_T = \int \Psi_T^* \widehat{H} \Psi_T d\mathbf{r}_1 d\mathbf{r}_2 \quad (2.4)$$

where  $\widehat{H}$  is a Hamiltonian. Then taking into account the spin contributions

$$\mathbf{S}^2 = (\mathbf{S}_1 + \mathbf{S}_2)^2 = S_1^2 + S_2^2 + 2\mathbf{S}_1 \cdot \mathbf{S}_2 \quad (2.5)$$

for which the scalar product is

$$\mathbf{S}_1 \cdot \mathbf{S}_2 = \frac{1}{2} S_{total} (S_{total} + 1) - \frac{3}{4} = \begin{cases} -\frac{3}{4} & \text{if } S_{total}=0 \text{ (singlet)} \\ +\frac{1}{4} & \text{if } S_{total}=1 \text{ (triplet)} \end{cases} \quad (2.6)$$

An effective Hamiltonian describing the energy can be expressed as<sup>1</sup>

$$\widehat{H} = \frac{1}{4} (E_S + 3E_T) - (E_S - E_T) \mathbf{S}_1 \cdot \mathbf{S}_2 \quad (2.7)$$

where the second half the equation is spin dependent. In order to determine which state is

lower in energy, we define a term known as the exchange integral,  $J$ :

$$J = E_S - E_T = 2 \int \psi_a^*(\mathbf{r}_1) \psi_b^*(\mathbf{r}_2) \widehat{H} \psi_a(\mathbf{r}_2) \psi_b(\mathbf{r}_1) d\mathbf{r}_1 d\mathbf{r}_2 \quad (2.8)$$

If the exchange integral  $J$  is positive then the triplet state with  $S_{total} = 1$  is energetically favored and the material is antiferromagnetic or ferrimagnetic. However if the exchange integral  $J$  is negative then the singlet state with  $S_{total} = 0$  is energetically favored and the material is ferromagnetic. However, this model is not suitable for all types of materials due to differences in the nature of bonding within each material. Longer-range indirect exchange

(superexchange, double-exchange, RKKY exchange) is important in specific material classes (e.g., ionic compounds, metal oxides, and rare earths). Therefore multiple models are necessary to describe the different physical phenomena.

## **2.2 Magnetic Anisotropy**

The magnetic anisotropy of a material will strongly influence its response to applied magnetic fields. There are several sources of magnetic anisotropy including magnetocrystalline (crystalline), shape, mechanical stress, processing (annealing, deformation, irradiation), and exchange anisotropy (exchange bias).

### **2.2.1 Magnetocrystalline Anisotropy**

Of particular importance is the magnetocrystalline anisotropy because of its intrinsic nature. Experimentally, a single crystalline material will magnetize differently along crystallographic orientations. The crystal directions along which the moments preferentially point are called “easy” axes; the energetically unfavorable directions are called “hard” axes. This behavior has its origins in the spin-orbit interaction (an interaction of electron spin with its motion). Since electron orbitals are linked to crystal structure, the moments (spins) will tend to align along well-defined (easy) crystal axes. To switch the direction of the moments lying on an easy axis (as would occur when the direction of an applied external field is switched) a certain amount of energy is necessary, known as the magnetocrystalline energy ( $E_A$ ). The magnetocrystalline energy per unit volume is represented by a power series of the form

$$E_a = \frac{E_o}{V_o} = \sum_n K_{un} \sin^{2n} \theta \quad (2.9)$$

but it is generally satisfactory to discard higher order terms, thus simplifying the equation to

$$E_a = K_{u1} \sin^2 \theta \quad (2.10)$$

where  $K_{u1}$  is called the first magnetocrystalline anisotropy constant or when higher order terms are neglected it is rewritten as  $K$ , the magnetocrystalline anisotropy constant. The angle between the magnetization direction and the easy axis is denoted by  $\theta$ . The magnetocrystalline anisotropy constant depends on temperature and decreases to zero upon approaching the Curie or Néel temperature, because the material becomes paramagnetic at these temperatures, and the magnetic ordering is consequently isotropic. Furthermore, the magnitude of the  $K$  can be used to separate materials into the classifications, specifically as hard or soft materials. Hard magnets have large magnetocrystalline anisotropy constants (therefore large coercivities) and soft materials have small magnetocrystalline anisotropy constants (therefore small coercivities) but often have large saturation magnetizations.

### 2.2.2 Exchange Anisotropy

Exchange anisotropy, also known as exchange bias, is of particular technological importance because it can increase the coercivity and superparamagnetic blocking temperature, as well as define an arbitrary unidirectional anisotropy direction in ferromagnetic materials. It is an interfacial phenomenon, in which an exchange interaction occurs between coupled ferromagnetic and antiferromagnetic materials. Exchange bias was first reported in the Co/CoO system by Meiklejohn and Bean in 1956.<sup>2</sup> While the

phenomenological origin of exchange bias is understood, the microscopic manner in which this exchange interaction between the spins then manifests itself into exchange bias is not thoroughly understood, and many competing models explaining this behavior exist.<sup>3-6</sup> In simple terms, exchange bias can be described as the alignment spins at the interface of a ferromagnetic/antiferromagnetic couple. When this couple is field cooled through the Néel temperature of the antiferromagnet, the spins at the interface of both the ferromagnet and antiferromagnet will align parallel to each other. The ferromagnet is strongly exchange-coupled to the antiferromagnet and will have its interfacial spins pinned. Because antiferromagnets generally have higher magnetocrystalline anisotropy than ferromagnets, this pinning requires extra energy to overcome and reverse the moment of the ferromagnet, which increases the coercivity. However, the pinning occurs in one direction only, and this asymmetry causes the hysteresis loop to shift from the origin ( $H=0$ ). A shifted hysteresis loop is the classical signature of exchange bias, but as previously stated, the coercivity and superparamagnetic blocking temperature of the ferromagnet can increase as well.

### **2.3 Superparamagnetism**

Superparamagnetism is a pertinent and persistent phenomenon in the nanoscale regime because it is a volume effect. In bulk ferromagnetic materials, ordering of the moments becomes random above the Curie temperature, but in nanomaterials a transition from the ferromagnetic state to a paramagnet-like (the superparamagnetic state) can occur well below the Curie temperature. Superparamagnetism can have serious implications for products that rely on the moments of the material to be stable (*e.g.* magnetic data storage).

This phenomenon occurs as thermal energy ( $k_B T$ ) becomes comparable to the magnetocrystalline anisotropy energy ( $E_a V$ ), which removes confining energy barriers and allows the moments to fluctuate between easy axes. The average time between flips, known as the Néel relaxation time, is described by:

$$\tau_n = \tau_o \exp\left(\frac{KV}{k_B T}\right) \quad (2.11)$$

where  $\tau_n$  is the average time between flips and  $\tau_o$  is the material-dependent attempt frequency with an approximate value of  $10^{-9}$  s. This equation can be rewritten to give the temperature at which the material will transition from ferromagnetism to superparamagnetism. The temperature at which this occurs is referred to as the superparamagnetic blocking temperature and is defined as:

$$T_b = \left(\frac{KV}{k_B C}\right) \quad (2.12)$$

where  $C = \ln(\tau_n/\tau_o)$  and is typically defined by experimentalists as being equal to 25 (corresponds to  $\sim 1$  min), whereas the magnetic storage industry requires  $C$  to be 50-70 (corresponds to  $> 10$  years).<sup>7</sup> Therefore, for the purposes of magnetic storage, it can be rewritten to estimate the magnetocrystalline anisotropy a material must possess to remain stable at given temperature for a given size

$$K = \frac{T_b C k_b}{V} \quad (2.13)$$

If one assumes room temperature,  $C=50$ , and a spherical particle of 10 nm, a material possessing a magnetocrystalline anisotropy of greater than  $1.2 \times 10^6$  J/m<sup>3</sup> would be necessary.

This means that only intrinsically very hard materials or those with additional anisotropy sources, can be used for ultra-high density BPM.

## 2.4 Single-Domain Limit

In the previous section it was stated of ferromagnetism all the magnetic moments will point in the same direction due to the exchange interaction, but domain formation is a process that must also be considered for sufficiently large NPs and bulk ferromagnets. In the absence of a saturating applied magnetic field, a sufficiently large ferromagnetic material will not be uniformly magnetized but rather will split into domains, individual regions where all the moments align. The net moment of each individual domain will align in different directions with respect to one another. This behavior is driven by energy minimization, specifically from magnetostatics. The moments in a domain generate a dipolar field, which will tend to align moments lying side-by-side in the opposite direction. The formation of domains requires energy to form domain walls. Therefore, small NPs consist of a single domain, if the savings in magnetostatic energy ( $\Delta E_{ms} \approx (4/9)\mu_0 M_s^2 \pi r^3$ , assuming a spherical particle) is less than the energy cost associated with forming a domain wall ( $\sigma_{dw} \pi r^2 = 4\pi r^2 (AK)^{1/2}$ ) where  $M_s$  is the saturation magnetization and  $A$  is the exchange stiffness constant (a measure of strength of coupling between neighboring spins). This assumes the domain wall in the NP is the same structure as that of a bulk material which is an acceptable approximation if the anisotropy of the NP is large enough to maintain the orientation of the moments along the easy axis. If the anisotropy is small, the moments will align along the surface poles and

follow the NP surface and this confinement effect increases the exchange energy contribution and a different equation is needed. Therefore a NP with large  $K$  ( $\geq \mu_0 M_S^2/6$ ) will have a corresponding critical radius of

$$r_c \approx 9 \frac{(AK)^{1/2}}{\mu_0 M_S^2} \quad (2.14)$$

whereas a NP with small  $K$  will have a critical radius of

$$r_c = \sqrt{9 \frac{9A}{\mu_0 M_S^2} \left[ \ln \left( \frac{2r_c}{a} \right) - 1 \right]} \quad (2.15)$$

above which multiple domains will form. Calculated-single domain limits for Co, Ni, and FePt are 80, 85, and 55 nm, respectively. Therefore, all materials reported in this dissertation are in the single domain regime.<sup>8</sup>

## 2.5 Magnetic Measurements

### 2.5.1 Temperature Dependent Measurements

A representative  $M$  vs.  $T$  curve is shown in Figure 1. The DC measurement of magnetization ( $M$ ) versus temperature ( $T$ ) in a small applied field is performed on magnetic NPs in order to determine the transition temperature between ferromagnetism and superparamagnetism. The sample is cooled in zero applied field to low temperature below the superparamagnetic blocking temperature. A small measuring field (100 Oe in our case) is applied, and the sample is heated, while measuring the magnetization as a function of specimen temperature. First, when the sample is cooled it becomes ferromagnetic as the temperature is lowered below the superparamagnetic blocking temperature. When the field

is applied, the magnetic moments are driven to align in the direction of the field due to the Zeeman energy ( $E_Z = -\mu_0 M H V$ ). However, the magnetocrystalline anisotropy dominates at low temperatures and keeps the moments aligned with the randomly-oriented NPs easy axes, which gives a low measured moment. Upon heating, the increased thermal energy provides magnetic moments sufficient energy to overcome the magnetocrystalline anisotropy energy and to point toward the magnetic field direction. However, at the superparamagnetic blocking temperature, there is a greater mean component of the fluctuating moments oriented in the field direction, which causes the magnetization to reach a maximum value. Upon further heating, the proportion of moments pointing in the applied field direction decreases, and the measured magnetization accordingly decreases. The magnetization behavior of superparamagnets obeys a Langevin function, which also describes the behavior of classical paramagnets. The temperature at which the magnetization peaks is assigned as the blocking temperature ( $T_B$ ).

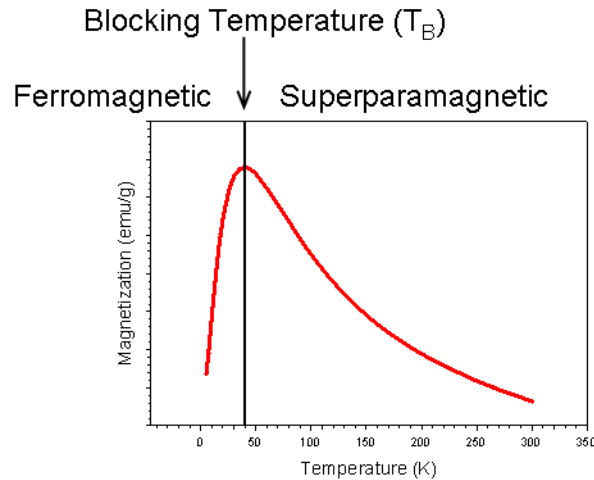


**Figure 1.** Schematic temperature-dependent magnetization ( $M$  vs.  $T$ ) curve of a ferromagnetic material.

### 2.5.2 Field-Dependent Measurements

A representative  $M$  vs.  $H$  curve is shown in Figure 2. As the applied field increases, the magnetization increases when the moments align in the direction of the field. At high fields, if all the moments are aligned in the same direction, the magnetization reaches a maximum value and approaches a constant value, known as the saturation magnetization ( $M_S$ ). Upon decreasing the field, the moments no longer align in the same direction, but there is hysteresis. At zero field, there remains a net magnetization, the remanance or remnant magnetization ( $M_R$ ). Increasing the field in the opposite direction will eventually drive the sample's magnetization to zero; the magnitude of this field is known as the coercivity ( $H_C$ ). This process is then repeated as the loop is traversed going from negative to positive applied field or positive to negative applied field. Below the superparamagnetic blocking temperature, the specimen will present an open loop ( $H_C > 0$ ), while above the

superparamagnetic blocking temperature the specimen will present a closed loop ( $H_C = 0$ ) because the moments are now fluctuating causing a loss of hysteresis.

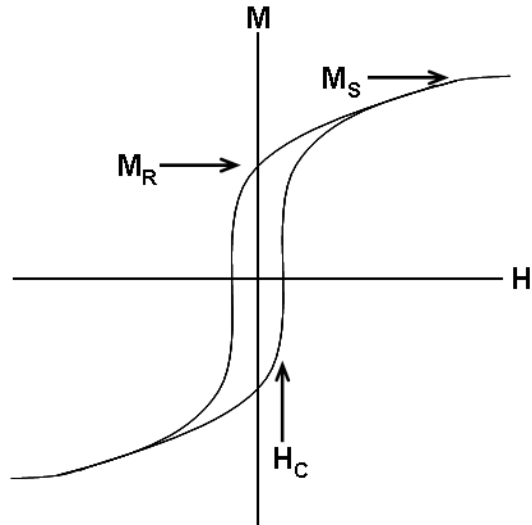


**Figure 2.** Schematic field dependent magnetization ( $M$  vs.  $H$ ) curve of a ferromagnetic material.

## 2.6 Stoner-Wohlfarth Model

In bulk specimens, magnetic hysteresis is understood through domain wall motion and lossy processes known as Barkhausen jumps, as the domain walls jump between local energy minima. However, the materials studied here are single domain and do not have domain walls. Hence, another model for understanding the origin of hysteresis is necessary. In single domain NPs, the magnetic response is described by the Stoner-Wohlfarth (SW) model. The SW model assumes an ellipsoid-shaped particle with uniaxial anisotropy along the long axis. The particle is uniformly magnetized, and the moments have a strong

exchange interaction such that the moments coherently rotate (all moments change direction in unison). The magnetization can be represented by a vector  $\mathbf{M}$  and in the absence of a field would lie along the anisotropy axis. In the presence of an applied field, the magnetization orients in a direction that would serve to minimize the energy of the system. The total energy is the sum of the magnetocrystalline anisotropy energies ( $E_A$ ) and Zeeman energies ( $E_Z$ ):

$$E = E_A + E_Z = K_{eff}V \sin(\phi - \theta) - \mu_0 M_s V H \cos \phi \quad (2.16)$$

where  $\theta$  is the angle between the direction of the magnetization and easy axis, while  $\phi$  is the angle between the direction of the applied field and  $K_{eff} = [K + 2\pi M_s^2(N_{\perp} - N_{\parallel})] \sin^2 \theta$

where  $N$  are demagnetization factors that are determined by the aspect ratio of the ellipsoid.

This equation can be expressed using normalized variables:

$$\eta = -\frac{1}{4} \cos[2(\phi - \theta)] - h \cos \phi \quad (2.17)$$

where  $\eta$  represents the variable energy,  $h = HM_s / 2K_{eff}$ . A stable energy minimum occurs if

$\partial \eta / \partial \phi = 0$  and  $\partial^2 \eta / \partial \phi^2 > 0$ . By solving  $\partial \eta / \partial \phi = (1/2) \sin[2(\phi - \theta)] + h \sin \phi$  for  $h$  as a

function of  $\phi$ , a hysteresis plot can be generated.

## 2.7 Magnetic Materials

Storage media for BPM require a combination of several physical properties. Not only does the material need to have an intrinsically high magnetocrystalline anisotropy (or an additional anisotropy mechanism), but are also stable against oxidation and a remanent magnetization that is sufficient enough for detection. Numerous ferromagnetic materials

exist, some of which are listed with their properties in Table 1. The intermetallic L1<sub>0</sub> FePt phase is an attractive choice, owing to its high saturation magnetization and magnetocrystalline anisotropy. However magnetic properties are not the only characteristic must be taken into consideration and as a result there currently is not an ideal material for ultra-high density BPM.

FePt NPs when synthesized by wet-chemistry techniques typically produce disordered (A1) phase or partially ordered L1<sub>0</sub>, whose magnetic properties are inferior to well-ordered L1<sub>0</sub> FePt. In the L1<sub>0</sub> phase there is a large spin-orbital coupling of the Pt electrons and hybridization between the Fe-d and the Pd-d states that significantly enhances the magnetocrystalline anisotropy.<sup>9</sup> Transforming the NPs to the L1<sub>0</sub> phase while preventing sintering is a significant challenge. Moreover, the complete phase conversion from the A1 phase into the L1<sub>0</sub> phase becomes especially challenging as the size of the NP decreases.<sup>10</sup> The bulk order-disorder reaction in FePt is first order,<sup>11</sup> but it has been shown experimentally<sup>12</sup> and theoretically<sup>13,14</sup> that it is a continuous (second order) transformation in NPs and dependent on size with the smallest dimension being the determining factor.<sup>12,15</sup> This behavior is thought to originate from surface-induced disorder, wherein the reduced bond coordination at the surface reduces the driving forces for ordering, and configurational entropy favors a disordered NP,<sup>13,14</sup> which has been supported experimentally.<sup>16</sup> Furthermore chemically synthesized FePt NPs have a Gaussian-like distribution of individual NP compositions.<sup>17,18</sup> A substantial portion of the NPs will therefore be unable to form a structure with perfect long range order ( $S = 1$ ) since equimolar concentration is required to do

so. Consequently, the magnetocrystalline anisotropy will be reduced from the value expected for perfect ordering.<sup>19,20</sup>

Alternatively, unary ferromagnetic species eliminate these issues of compositional control but have lower magnetocrystalline anisotropy. Fe, Co, and Ni are susceptible to varying extents of oxidation. Fe NPs are generally unstable at room temperature and will oxidize completely, while Co and Ni NPs will form passivating oxide layers of CoO and NiO respectively. Since Co and Ni have lower magnetocrystalline anisotropy than L1<sub>0</sub> FePt, external sources of magnetic anisotropy could be considered for use to augment the intrinsic magnetocrystalline anisotropy. Enhanced anisotropy through shape control (shape anisotropy) is possible but complicates both self-assembly and the NP synthesis. Exchange bias could also be considered; the obvious antiferromagnet coupling choices would be CoO and NiO, whose extent of formation and subsequently magnetic properties can be controlled systematically through intentional oxidization.<sup>21</sup> However, the Néel temperature CoO imposes significant limitations as it is approximately room temperature, and the anisotropy enhancement would not occur or could be easily reset during normal ambient operation conditions.

**Table 1.** Magnetic properties of select transition metals and metal oxides that are of interest for use in nanotechnology applications including bit-patterned media. The critical diameter is the minimal stable grain size,  $(60k_B T/K)^{1/3}$  ( $\tau=10$  years).<sup>22</sup> Except where noted, all data are from reference.<sup>23</sup>

Material	Magnetic Structure	Crystalline Structure	$M_S$ (290K) (emu/cm <sup>3</sup> )	$\mu_B$	$T_C$ or $T_N$ (K)	$K$ (J/m <sup>3</sup> ) @ RT	Critical Diameter (nm)
Co	Ferromagnetic	FCC	1440	1.75	1390 <sup>24</sup>		
Co	Ferromagnetic	HCP	1440	1.72		$4.1 * 10^6$	8.5
Co	Ferromagnetic	Cubic		1.70 <sup>25</sup>		$(1.5 * 10^6)^{26}$	11.8
CoO	Antiferromagnetic	Rocksalt			291 <sup>27</sup>		
Co <sub>3</sub> O <sub>4</sub>	Antiferromagnetic	Spinel			40 <sup>28</sup>		
Ni	Ferromagnetic	FCC	485	0.606	627	$-4.5 * 10^4$	38.1
NiO	Antiferromagnetic	Rocksalt			525 <sup>27</sup>		
Fe	Ferromagnetic	BCC	1707	2.22	1044 <sup>24</sup>	$4.8 * 10^5$	17.3
FePt	Ferromagnetic	FCC				$(1.1 * 10^5)^{29}$	28.3
FePt	Ferromagnetic	FCT	1140 <sup>30</sup>		750 <sup>30</sup>	$(6.6 * 10^7)^{30}$	3.4

## REFERENCES

- 1 R. K. Nesbet, *Physical Review* **122**, 1497 (1961).
- 2 W. H. Meiklejohn and C. P. Bean, *Physical Review* **102**, 1413 (1956).
- 3 J. Nogués, J. Sort, V. Langlais, V. Skumryev, S. Suriñach, J. S. Muñoz, and M. D. Baró, *Physics Reports* **422**, 65 (2005).
- 4 J. Nogués and I. K. Schuller, *Journal of Magnetism and Magnetic Materials* **192**, 203 (1999).
- 5 M. Kiwi, *Journal of Magnetism and Magnetic Materials* **234**, 584 (2001).
- 6 A. E. Berkowitz and K. Takano, *Journal of Magnetism and Magnetic Materials* **200**, 552 (1999).
- 7 C. Ross, *Annual Review of Materials Research* **31**, 203 (2001).
- 8 K. M. Krishnan, A. B. Pakhomov, Y. Bao, P. Blomqvist, Y. Chun, M. Gonzales, K. Griffin, X. Ji, and B. K. Roberts, *Journal of Materials Science* **41**, 793 (2006).
- 9 G. H. O. Daalderop, P. J. Kelly, and M. F. H. Schuurmans, *Physical Review B* **44**, 12054 (1991).
- 10 D. Yi and A. M. Sara, *Applied Physics Letters* **87**, 022508 (2005).
- 11 S. H. Whang, Q. Feng, and Y. Q. Gao, *Acta Materialia* **46**, 6485 (1998).
- 12 D. Alloyeau, C. Ricolleau, C. Mottet, T. Oikawa, C. Langlois, Y. Le Bouar, N. Braidy, and A. Loiseau, *Nat Mater* **8**, 940 (2009).
- 13 B. Yang, M. Asta, O. N. Mryasov, T. J. Klemmer, and R. W. Chantrell, *Acta Materialia* **54**, 4201 (2006).
- 14 M. Müller, P. Erhart, and K. Albe, *Physical Review B* **76**, 155412 (2007).
- 15 W. H. Qi, Y. J. Li, S. Y. Xiong, and S. T. Lee, *Small* **6**, 1996 (2010).
- 16 A. Kovács, K. Sato, V. K. Lazarov, P. L. Galindo, T. J. Konno, and Y. Hirotsu, *Physical Review Letters* **103**, 115703 (2009).
- 17 C. C. Y. Andrew, M. Mizuno, Y. Sasaki, and H. Kondo, *Journal of Applied Physics* **85**, 6242 (2004).

- 18 S. Chandan, E. N. David, and B. T. Gregory, *Journal of Applied Physics* **104**, 104314 (2008).
- 19 J. B. Staunton, S. Ostanin, S. S. A. Razee, B. Gyorffy, L. Szunyogh, B. Ginatempo, and E. Bruno, *Journal of Physics-Condensed Matter* **16**, S5623 (2004).
- 20 S. Ostanin, S. S. A. Razee, J. B. Staunton, B. Ginatempo, and E. Bruno, *Journal of Applied Physics* **93**, 453 (2003).
- 21 J. B. Tracy, D. N. Weiss, D. P. Dinega, and M. G. Bawendi, *Physical Review B* **72**, 064404 (2005).
- 22 D. Weller and M. F. Doerner, *Annual Review of Materials Science* **30**, 611 (2000).
- 23 R. C. O'Handley, *Modern Magnetic Materials: Principles and Applications* (John Wiley & Sons, Inc., New York, 2000).
- 24 H. P. J. Wijn, *Magnetic Properties of Metals: d-Elements, Alloys and Compounds* (Springer-Verlag, New York, 1991).
- 25 D. P. Dinega, Thesis, Massachusetts Institute of Technology, 2001.
- 26 V. F. Puentes and K. M. Krishnan, *IEEE Transactions on Magnetics* **37**, 2210 (2001).
- 27 C. Kittel, *Introduction to Solid State Physics*, 8th ed. (Wiley, Hoboken, NJ, 2005).
- 28 R. W.L, *Journal of Physics and Chemistry of Solids* **25**, 1 (1964).
- 29 B. Stahl, J. Ellrich, R. Theissmann, M. Ghafari, S. Bhattacharya, H. Hahn, N. S. Gajbhiye, D. Kramer, R. N. Viswanath, J. Weissmüller, and H. Gleiter, *Physical Review B* **67**, 014422 (2003).
- 30 T. Klemmer, D. Hoydick, H. Okumura, B. Zhang, and W. A. Soffa, *Scripta Metallurgica et Materialia* **33**, 1793 (1995).

## CHAPTER 3

### **Self-Assembly of Nanoparticles**

Many proposed applications of nanomaterials require organization into ordered structures. It is an immense challenge to controllably arrange potentially trillions of NPs that cannot be seen or controlled using established fabrication methods. Allowing naturally occurring forces to spontaneously organize disordered NPs into ordered structures, a process known as self-assembly, is arguably the most promising method to overcome this challenge. A great deal of research has been conducted in this field, and much progress has been to improve the length scale and quality of assemblies. To fabricate these higher-ordered structures from nanomaterials in a controlled fashion requires both an understanding of interparticle interactions and the ability to modify them.

#### **3.1 Forces Guiding Self-Assembly**

Different interaction forces may exist between NPs whose magnitude and range of interaction will have implications if the NPs assemble into order structures or agglomerate into disordered arrangements. In terms of ferromagnetic ligand-stabilized NPs, the most relevant forces are van der Waals, magnetic dipole-dipole, and steric, but other forces may contribute.

Van der Waals forces originate from electromagnetic fluctuations and therefore exist between any two NPs. Van der Waals interaction can be described by three kinds of interactions, Keesom forces (two permanent dipoles), Debye forces (permanent dipole and a

corresponding induced dipole), and London dispersion forces (two instantaneously induced dipoles). To approximate the net interaction energy, one can integrate these forces over the volumes of two NPs represented by two spheres of radii  $r_1$  and  $r_2$ , separated by a center-to-center distance  $d$ :

$$U_{vdW} = \frac{A}{3} \left[ \frac{r_1 r_2}{d^2 - (r_1 + r_2)^2} + \frac{r_1 r_2}{d^2 - (r_1 - r_2)^2} + \frac{1}{2} \ln \left( \frac{d^2 - (r_1 + r_2)^2}{d^2 - (r_1 - r_2)^2} \right) \right] \quad (3.1)$$

where  $A$  is the Hamaker coefficient which is equal to

$$A = \frac{C_{vdW} \pi^2}{v_1 v_2} \quad (3.2)$$

where  $C_{vdW}$  is a constant and  $v$  is the molar volume of a material.<sup>2</sup> For a monodisperse sample of NPs with radii that are approximately the same ( $r_1 \approx r_2$ ), the interaction energy can be simplified to

$$U_{vdW} = \frac{A}{3} \left[ \frac{r^2}{d^2 - 4r^2} + \frac{r^2}{d^2} + \frac{1}{2} \ln \left( \frac{d^2 - 4r^2}{d^2} \right) \right] \quad (3.3)$$

However, this model may not be completely appropriate for NPs because the faceted surfaces and discrete arrangement of atoms in a NP violates the continuum assumptions made, specifically the presence of smooth geometric surfaces and constant dielectric properties.<sup>3</sup> Therefore, a more rigorous mathematical treatment rather than a simple integration may be more appropriate.<sup>4</sup>

Coulombic forces unexpectedly can occur between ligand stabilized NPs in nonpolar solvents because electric charges may be present<sup>5,6</sup> and are tunable by changing the

chemistry of surface ligands.<sup>7</sup> The interaction energy between two point charges, in this case assumed to be on the surface of two NPs, is described by the Coulombic potential

$$U_{Coul} = \frac{q_1 q_2}{4\pi\epsilon\epsilon_0 D} \quad (3.4)$$

where  $q$  is a point charge,  $\epsilon$  the dielectric constant, and  $D$  the distance between the two charges. Coulombic and charge-dipole forces have been attributed with the formation of ordered structures whose packing is less dense than if van der Waals forces solely dictated the assembly.<sup>8</sup>

Ferromagnetic NPs will experience magnetic dipole-dipole interactions that can also influence the assembly process. The dipole-dipole energy between two spherical NPs can be written as

$$U_{DD} = \frac{1}{4\pi d^3} \left( \mathbf{m}_1 \cdot \mathbf{m}_2 - \frac{3(\mathbf{m}_1 \cdot \mathbf{d})(\mathbf{m}_2 \cdot \mathbf{d})}{d^2} \right) \quad (3.5)$$

where  $\mathbf{m}$  is the moment of each NP and  $\mathbf{d}$  is the separation between the NPs. Depending on the spatial relationship between two NPs and orientation of the dipoles the dipole-dipole interaction may be attractive or repulsive,<sup>9</sup> but if the NPs are sufficiently mobile to reorient, the interactions will generally be attractive. NP size will strongly influence the dipolar coupling behavior because the moment of the single-domain NPs scales with the volume ( $m=M_s V$ ). Moreover, if the NPs are superparamagnetic rather than ferromagnetic the dipolar coupling is weakened due to the fluctuating moments. The interactions of superparamagnetic NPs can be approximated by

$$U_{dd} = -\frac{1}{3k_B T} \left( \frac{m_1 m_2}{4\pi\mu_0 r^3} \right)^2 \quad (3.6)$$

if  $m_1 m_2 / 2\pi\mu_0 r^3 \ll 6k_B T$ .

Between van der Waals and magnetic dipole-dipole interactions, there can be strong ( $\gg k_B T$ ) attractive forces that could cause agglomeration rather than the formation of ordered assemblies. Repulsive forces can balance these attractive forces and enable ordering. Steric repulsion is the force generated when two or more species overlap and occupy less volume than their separated structures. In the case of NPs stabilized with ligands, when NPs are brought into contact the surface ligands begin to interact and the configurational freedom of the ligands is decreased, reducing the configurational entropy, which produces a repulsive force.<sup>10</sup> For two spherical NPs the repulsion would be described by

$$U_s \approx \frac{\pi^3 k_B T \Gamma h_0^3 r_1 r_2}{3N b^2 (r_1 + r_2)} \left[ -\ln u - \frac{9}{5}(1-u) + \frac{1}{3}(1-u^3) - \frac{1}{30}(1-u^6) \right] \quad (3.7)$$

where  $u = d - r_1 - r_2 / 2h_0$ ,  $h_0$  is the equilibrium thickness of the ligand shell,  $\Gamma$  is the density of the ligands on the surface, and  $N$  is the number of “Kuhn monomers” (the basic repeat unit of the ligand) each with a characteristic length  $b$ .<sup>1</sup>

In systems where the NP sample is polydisperse, entropic forces can drive ordering, where the NPs organize into regions of different sizes. If there are two sizes of NPs in a solution, with radii  $r_1$  and  $r_2$  where  $r_1 < r_2$ , as the distance between two NPs of size  $r_2$  decreases such that a NP of size  $r_1$  can no longer insert itself between the two, a depletion layer forms, as shown in Figure 1. The depletion layer, where the ligands shells of the two larger NPs interdigitate, increases volume accessible to the smaller NP, by decreasing the

amount of inaccessible volume to the smaller NP, which decreases the energy of the system.

The interaction energy between spheres of two different sizes is described by

$$U_{dep} = -\frac{\pi p_0}{12} \left[ 2(2r_2 + r_1)^3 - 3(2r_2 + r_1)^2 d + d^3 \right] \quad (3.8)$$

where  $p_0$  is the osmotic pressure ( $p_0 = Nk_B T/V_0$ ,  $N$  is the number of small NPs and  $V_0$  is the volume of the system) and Equation 3.7 is valid over the length scales  $2r_2 < d < 2r_2 + r_1$ .

This force tends to be small for spherical NPs and insufficient to induce aggregation.<sup>1,11</sup>

Nonetheless depletion forces are strong enough to create ordered assemblies such that large NPs will form the center of an assembled region, while the smaller NPs will assemble at the periphery.<sup>12</sup>

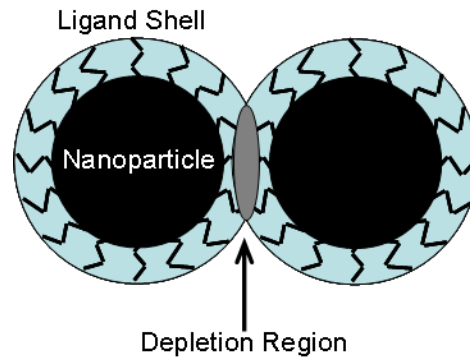


**Figure 1.** Schematic of an entropy-driven depletion region

### 3.2 Self-Assembly of Nanoparticle Monolayers

For the purposes of BPM, the desired structure would be a monolayer of NPs with a fixed interparticle spacing and a circular geometry. The presence of stabilizers, whether they be aliphatic carbon chains with functional head groups (commonly referred as ligands), polymer chains, or DNA on the NP surface provides a facile means of controlling the interparticle spacing from ~1-20 nm.<sup>13,14</sup> Ordered NP monolayers will typically form into close-packed structures, but through control of the surface ligands four-fold (square) close-packed structures can be obtained under certain conditions.<sup>12,15</sup> The use of patterned tracks or templates could conceivably enable arrays with circular geometry.<sup>16</sup>

Perhaps the most difficult engineering challenge associated with the self-assembly of NPs into monolayers for use in BPM is the length scale ( $>cm^2$ ) of defect-free assembly that would be necessary because structural defects would result in read and write errors. Current reports of NP self-assembly on these types of length scales are limited and defects such as multilayer regions, gaps, and domain boundaries.<sup>17-20</sup> All of these reports use the approach of self-assembly at a liquid-air interface, which allows the NPs time to rearrange into a well-ordered structure before the monolayer film is transferred onto the solid substrate. These reports of wafer-scale assembly reportedly took ~5-20 min of assembly time, and increasing the assembly time generally facilitates equilibrium ordering rather than producing assemblies with kinetically trapped states.<sup>21</sup> Such long times for achieving equilibrium could be a bottleneck in a commercial scheme, if each HDD required the self-assembly of its BPM component.

One final consideration is magnetic dipole-dipole interactions and their influence on the assembly process. In the previously cited reports, the large-scale assembly was performed using gold or superparamagnetic NPs, which had weak magnetic dipole-dipole interactions. Ferromagnetic (rather than superparamagnetic) NPs have much stronger magnetic dipole-dipole interactions and consequently will assemble in a different fashion. The NPs tend not to form continuous, close-packed monolayers but instead form chain or ring-like assemblies, as shown in Figure 2, that minimize the magnetic interactions.<sup>9,12,22,23</sup> These types of assemblies are unacceptable in their current form, which presents a significant challenge for BPM because NPs that are ferromagnetic at room temperature are required, but strong dipolar coupling could destabilize bits, when magnetically-coupled neighboring bits are written. Therefore, alternative routes may be necessary to form appropriately patterned monolayer arrays. Hypothesized solutions to the problem may include (1) conducting self-assembly at higher temperatures where the NPs are superparamagnetic, (2) utilizing the flux-closure behavior (which has the added benefit of naturally forming loops with the desired circular geometry) and controllably generating loops of appropriate dimensions and arrangement, or (3) assembling NPs that are superparamagnetic at room temperature and subsequently increasing their anisotropy post assembly through additional processing (*e.g.* phase conversion of FePt from the disordered to intermetallic phase or introduce an antiferromagnetic layer such that exchange bias occurs). In this study, Route 3 was pursued and is discussed further in Chapters 9 and 10.

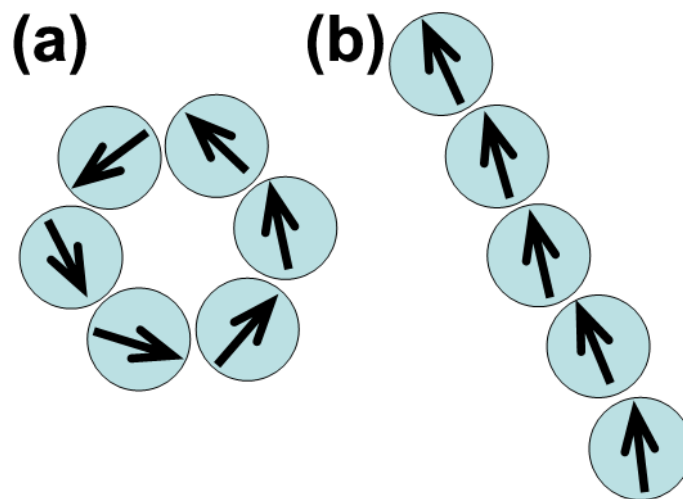


**Figure 2.** Schematic of ferromagnetic nanoparticles and their associated dipoles arranging themselves into (a) rings and (b) chains, thereby reducing their magnetostatic energy.

## REFERENCES

- <sup>1</sup> K. J. M. Bishop, C. E. Wilmer, S. Soh, and B. A. Grzybowski, *Small* **5**, 1600 (2009).
- <sup>2</sup> H. C. Hamaker, *Physica* **4**, 1058 (1937).
- <sup>3</sup> C. Noguez, *Journal of Physical Chemistry C* **111**, 3806 (2007).
- <sup>4</sup> H.-Y. Kim, J. O. Sofo, D. Velegol, M. W. Cole, and A. A. Lucas, *Langmuir* **23**, 1735 (2007).
- <sup>5</sup> S. Moonsub and G.-S. Philippe, *Journal of Chemical Physics* **111**, 6955 (1999).
- <sup>6</sup> T. D. Krauss and L. E. Brus, *Physical Review Letters* **83**, 4840 (1999).
- <sup>7</sup> E. V. Shevchenko, D. V. Talapin, N. A. Kotov, S. O'Brien, and C. B. Murray, *Nature* **439**, 55 (2006).
- <sup>8</sup> D. V. Talapin, E. V. Shevchenko, C. B. Murray, A. V. Titov, and P. Kral, *Nano Letters* **7**, 1213 (2007).
- <sup>9</sup> J. Y. Ku, D. M. Aruguete, A. P. Alivisatos, and P. L. Geissler, *Journal of the American Chemical Society* **133**, 838 (2011).
- <sup>10</sup> D. F. Evans and H. Wennerström, *The Colloidal Domain: Where Physics, Chemistry, Biology, and Technology Meet*, 2nd ed. (Wiley-VCH, New York, 1999).
- <sup>11</sup> P. D. Kaplan, J. L. Rouke, A. G. Yodh, and D. J. Pine, *Physical Review Letters* **72**, 582 (1994).
- <sup>12</sup> Y. P. Bao, M. Beerman, and K. M. Krishnan, *Journal of Magnetism and Magnetic Materials* **266**, L245 (2003).
- <sup>13</sup> J. E. Martin, J. P. Wilcoxon, J. Odinek, and P. Provencio, *The Journal of Physical Chemistry B* **104**, 9475 (2000).
- <sup>14</sup> W. Cheng, M. J. Campolongo, J. J. Cha, S. J. Tan, C. C. Umbach, D. A. Muller, and D. Luo, *Nat Mater* **8**, 519 (2009).
- <sup>15</sup> S. Sun, C. B. Murray, D. Weller, L. Folks, and A. Moser, *Science* **287**, 1989 (2000).
- <sup>16</sup> D. Farrell, Y. Cheng, S. Kan, M. Sachan, Y. Ding, S. A. Majetich, and L. Yang, in *Iron nanoparticle assemblies: structures and magnetic behavior*, Bristol, 2005 (Iop Publishing Ltd), p. 185.

- 17 A. G. Dong, X. C. Ye, J. Chen, and C. B. Murray, *Nano Letters* **11**, 1804 (2011).
- 18 A. Desireddy, C. P. Joshi, M. Sestak, S. Little, S. Kumar, N. J. Podraza, S. Marsillac, R. W. Collins, and T. P. Bigioni, *Thin Solid Films* **519**, 6077 (2011).
- 19 M. N. Martin, J. I. Basham, P. Chando, and S. K. Eah, *Langmuir* **26**, 7410 (2010).
- 20 M. N. Martin and S. K. Eah, *Materials Research Society Symposium Proceedings* **1113**, F03 (2009).
- 21 D. Farrell, Y. Cheng, Y. Ding, S. Yamamuro, C. Sanchez-Hanke, C.-C. Kao, and S. A. Majetich, *Journal of Magnetism and Magnetic Materials* **282**, 1 (2004).
- 22 P. Y. Keng, I. Shim, B. D. Korth, J. F. Douglas, and J. Pyun, *Acs Nano* **1**, 279 (2007).
- 23 S. L. Tripp, R. E. Dunin-Borkowski, and A. Wei, *Angewandte Chemie* **115**, 5749 (2003).

## CHAPTER 4

### **Thin Film Growth**

For this thesis, two deposition techniques were used to grow thin films. Atomic layer deposition (ALD) and pulsed laser deposition (PLD) can be classified under the general deposition methodologies of chemical vapor deposition (CVD) and physical vapor deposition (PVD), respectively. An overview of both techniques follows.

#### **4.1 Atomic Layer Deposition**

ALD has become an attractive choice in the semiconductor industry for the deposition of gate oxides in devices such as metal–oxide–semiconductor field-effect transistors (MOSFETs) because of the high level of control and conformality that ALD films provide. The high quality of the films arises from the growth mechanism. ALD (also sometimes referred to as atomic layer epitaxy though this terminology is less common because not all films grown have an epitaxial relationship) produces films in a stepwise fashion, in which a pair of reactants react in sequential, self-limiting steps. The growth of metal oxides consists primarily of four steps: (1) metal precursor exposure (2) purging residual precursors and by-product molecules from the growth chamber (3) exposure of the other reactant species (the nonmetal precursor) and (4) purging the residual reactants and by-product molecules from the growth chamber. The reactions can only occur at the surface of the growing film because only one of the two gaseous precursors is in the growth chamber at a time. Through appropriate selection of the precursor gases, the surface reactions are self-limiting because

the precursors are only be able to react with a finite number of surface sites. Once an available surface site has reacted with a precursor gas molecule, the site becomes inactive and any additional precursor will not be able to react with the surface. Even if the flux of precursor molecules over the surface is non-uniform, the entire surface will eventually react and create a uniform conformal coating due to this self-limiting behavior.

The ALD growth process depends on the reactions kinetics, precursor adsorption and steric hindrance, self-termination, and growth modes. Precursor molecules can either attach to a surface through physisorption (a weak van der Waals interaction) or chemisorption (a chemical bonding interaction). Physisorbed molecules can form multilayers, while chemisorbed molecules can only form monolayer because chemical bonds are formed with the surface of the deposited film. Furthermore, both physisorption and chemisorption can be reversible but for growth and self-termination to occur, the precursor molecule must irreversibly chemisorb to the surface. The manner in which the precursor molecule attaches to a surface can be described as ligand (organic group) exchange – a ligand reacts with a surface group forming a volatile compound that is release while the remaining portion of the precursor molecule chemisorbs to the surface, dissociation – a precursor molecule is split onto reactive two or more surface sites, or association – a precursor molecule forms a coordinative bond (a dipolar bond) with a reactive site on the surface and is chemisorbed without loss of any ligand.<sup>1,2</sup> The surface becomes saturated when the number of surface sites are completely filled or the ligand steric hindrance impedes any further reactions.<sup>3</sup>

The rate at which the surface becomes saturated can be modeled by assuming reversible adsorption at identical surface sites, no interactions between adsorbed molecules, and only one site can adsorb one molecule. Therefore, the adsorption rate can be defined as

$$\frac{dQ}{dt} = r_a - r_d = k_a p(1-Q) - k_d Q \quad (4.1)$$

where  $Q$  fraction of “filled” surface sites (the site becomes filled by adsorbing a precursor molecule or being unable to react due to the steric hindrance of a precursor molecule adsorbed on an adjacent surface site),  $r_a$  is the adsorption rate,  $r_d$  is the desorption rate,  $p$  is the partial pressure of the precursor,  $k_a$  is the adsorption rate constant, and  $k_d$  is the desorption rate constant. If we integrate equation 4.1 as a function of time and assume irreversible adsorption ( $k_d=0$ , which gives  $Q=1$  at equilibrium)

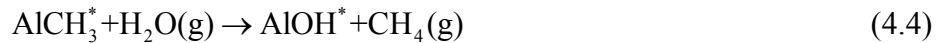
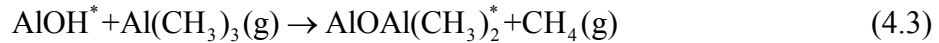
$$Q = 1 - e^{-k_a p t} . \quad (4.2)$$

The surface saturates before all the surface sites have completely reacted with precursor molecules because steric hindrance prevents the formation of a full monolayer. Consequently the growth rates per cycle observed will always be less than a full monolayer (e.g.  $\sim 1.1-1.2 \text{ \AA}$  per cycle for the growth of  $\text{Al}_2\text{O}_3$  in the trimethylaluminum (TMA) and  $\text{H}_2\text{O}$  reaction<sup>4</sup> whereas a full monolayer would be roughly three times as thick). This behavior has been modeled, and the general consensus is that the growth rate increases as the size of the reactant molecules and/or adsorbed species decreases.<sup>5-7</sup> Reaction temperature and density of active surface sites will influence the growth rate per cycle. Both parameters can enhance or retard growth rates, depending on specific details of the reaction.

## 4.2 Growth of Al<sub>2</sub>O<sub>3</sub> by Atomic Layer Deposition

In the reported research, ALD was used to grow amorphous Al<sub>2</sub>O<sub>3</sub>, for which the growth reaction commonly employs TMA as the metal precursor and water vapor as the non-metal precursor (oxygen source). Growth of Al<sub>2</sub>O<sub>3</sub> with TMA and water vapor is a rather ideal reaction, because it is a thermally-activated process that requires no additional activation source, such as plasma or ozone. Furthermore, TMA is a highly reactive (and pyrophoric) precursor whose reactions are truly self-terminating (due to the large, negative reaction enthalpy for the formation of a Al-O bonds), while its by-products (*e.g.* methane) are relatively inert.<sup>8</sup> However TMA is susceptible to decomposition at temperatures above 300 °C which can lead to side reactions<sup>9</sup> and the inclusion of H and C impurities into grown films.<sup>10,11</sup>

The chemical reaction that produces Al<sub>2</sub>O<sub>3</sub> can be described by two half reactions<sup>12,13</sup>



where asterisks indicate surface sites. Under appropriately selected reaction conditions, these half reactions will occur separately (due to avoiding simultaneous exposure to TMA and water) and the growth will occur in a linear fashion.<sup>4</sup> The growth of Al<sub>2</sub>O<sub>3</sub> is regarded as two-dimensional, but initial nucleation and growth of the film may follow another growth mechanism depending on the initial number of reaction sites available. In cases where the number of active sites is limited the initial growth mode is island growth and only after additional growth cycles does the film become uniform.<sup>14</sup>

### 4.3 Atomic Layer Deposition of Al<sub>2</sub>O<sub>3</sub> on Nanoparticles

ALD has been reported to coat both supported NPs<sup>15</sup> and unsupported NPs.<sup>16</sup> Such growth has been reported, on metals,<sup>15,17-19</sup> metal oxides,<sup>16,20,21</sup> as well as non-metals<sup>22</sup> suggesting that the nucleation and growth of Al<sub>2</sub>O<sub>3</sub> using TMA and water vapor is a versatile and robust system for coating applications. Al<sub>2</sub>O<sub>3</sub> coatings grown by ALD have been reported to impart thermal stability<sup>15,18,19</sup> and inhibit oxidation,<sup>17,23</sup> both of which are particularly important for magnetic NPs that may require annealing (*e.g.* to drive phase conversions or restructure morphology or crystallographic orientation) or are susceptible to oxidation, which significantly alters the magnetic properties.

### 4.4 Pulsed Layer Deposition

PLD a non-equilibrium process that provides many unique opportunities when coupled with its versatility. This process can be applied to a wide swath of material classes (*e.g.*, superconductors, ferroelectrics, and semiconductors) to generate many different film structures (*e.g.*, amorphous, polycrystalline, and epitaxial films, meta-stable phases, and discrete islands or embedded structures).

Experimentally, PLD is relatively simple technique. The main components of the process include a high-energy pulsed laser beam that is typically in the ultraviolet optical spectrum. Through the use of optical components the laser beam is focused at a target of the material for deposition, which is located in a vacuum chamber. The focusing optics and windows that the laser beam passes through are constructed from materials such that there is minimum attenuation of the laser light. The target material is vaporized in the region where

the laser struck and forms a plasma plume, which then deposits onto a substrate which is in close proximity opposite from the target. Several experimental parameters are available to control the growth conditions, including interactions of the plume with the vacuum chamber atmosphere (deposition can occur in vacuum or a background gas), interaction between the laser light and target, which depends on both the laser beam parameters (*e.g.* wavelength, pulse duration, power density) and the physical properties (*e.g.* refractive index) of the material.

#### **4.5 Pulsed Layer Deposition Coating of Nanomaterials**

Reports of coating NPs (not grown by PLD in conjunction with the coating) by means of PLD appear to be rather limited.<sup>24</sup> However the ability to grow amorphous metal oxide films such as Al<sub>2</sub>O<sub>3</sub> is well reported.<sup>25-27</sup> Presumably the disconnect between the ability to grow films that could impart attractive properties such as thermal stability and resistance to oxidation as cited in Section 4.3 arises from the line-of-sight nature of PLD, which does not produce highly conformal coatings like ALD. For this reason, ALD has often been chosen for coating NPs.

## REFERENCES

- <sup>1</sup> M. E. Bartram, T. A. Michalske, and J. W. Rogers, *Journal of Physical Chemistry* **95**, 4453 (1991).
- <sup>2</sup> M. E. Bartram, T. A. Michalske, J. W. Rogers, and T. M. Mayer, *Chemistry of Materials* **3**, 953 (1991).
- <sup>3</sup> R. L. Puurunen, A. Root, S. Haukka, E. I. Iiskola, M. Lindblad, and A. O. I. Krause, *Journal of Physical Chemistry B* **104**, 6599 (2000).
- <sup>4</sup> A. W. Ott, J. W. Klaus, J. M. Johnson, and S. M. George, *Thin Solid Films* **292**, 135 (1997).
- <sup>5</sup> R. L. Puurunen, *Chemical Vapor Deposition* **9**, 249 (2003).
- <sup>6</sup> M. Ritala, M. Leskela, and E. Rauhala, *Chemistry of Materials* **6**, 556 (1994).
- <sup>7</sup> Y. Markku, *Thin Solid Films* **279**, 124 (1996).
- <sup>8</sup> R. L. Puurunen, *Journal of Applied Physics* **97**, 52 (2005).
- <sup>9</sup> R. L. Puurunen, M. Lindblad, A. Root, and A. O. I. Krause, *Physical Chemistry Chemical Physics* **3**, 1093 (2001).
- <sup>10</sup> S. J. Yun, K. H. Lee, J. Skarp, H. R. Kim, and K. S. Nam, *Journal of Vacuum Science & Technology a-Vacuum Surfaces and Films* **15**, 2993 (1997).
- <sup>11</sup> J. Kim, K. Chakrabarti, J. Lee, K.-Y. Oh, and C. Lee, *Materials Chemistry and Physics* **78**, 733 (2003).
- <sup>12</sup> C. Soto, R. Wu, D. W. Bennett, and W. T. Tysoe, *Chemistry of Materials* **6**, 1705 (1994).
- <sup>13</sup> A. C. Dillon, A. W. Ott, J. D. Way, and S. M. George, *Surface Science* **322**, 230 (1995).
- <sup>14</sup> R. L. Puurunen, W. Vandervorst, W. F. A. Besling, O. Richard, H. Bender, T. Conard, C. Zhao, A. Delabie, M. Caymax, S. De Gendt, M. Heyns, M. M. Viitanen, M. de Ridder, H. H. Brongersma, Y. Tamminga, T. Dao, T. de Win, M. Verheijen, M. Kaiser, and M. Tuominen, *Journal of Applied Physics* **96**, 4878 (2004).
- <sup>15</sup> J.-Z. Kong, Y.-P. Gong, X.-F. Li, A.-D. Li, J.-L. Zhang, Q.-Y. Yan, and D. Wu, *Journal of Materials Chemistry* **21**, 5046 (2011).

- 16 J. A. McCormick, B. L. Cloutier, A. W. Weimer, and S. M. George, *Journal of Vacuum Science & Technology A* **25**, 67 (2007).
- 17 L. F. Hakim, C. L. Vaughn, H. J. Dunsheath, C. S. Carney, X. Liang, P. Li, and A. W. Weimer, *Nanotechnology* **18**, 7 (2007).
- 18 H. Feng, J. L. Lu, P. C. Stair, and J. W. Elam, *Catalysis Letters* **141**, 512 (2011).
- 19 A. V. Whitney, J. W. Elam, P. C. Stair, and R. P. Van Duyne, *The Journal of Physical Chemistry C* **111**, 16827 (2007).
- 20 L. F. Hakim, J. Blackson, S. M. George, and A. W. Weimer, *Chemical Vapor Deposition* **11**, 420 (2005).
- 21 B. Min, J. S. Lee, J. W. Hwang, K. H. Keem, M. I. Kang, K. Cho, M. Y. Sung, S. Kim, M. S. Lee, S. O. Park, and J. T. Moon, *Journal of Crystal Growth* **252**, 565 (2003).
- 22 X. H. Liang, G. D. Zhan, D. M. King, J. A. McCormick, J. Zhang, S. M. George, and A. W. Weimer, *Diamond and Related Materials* **17**, 185 (2008).
- 23 Y. Zhou, D. M. King, J. Li, K. S. Barrett, R. B. Goldfarb, and A. W. Weimer, *Industrial & Engineering Chemistry Research* **49**, 6964 (2010).
- 24 T. Ning, C. Chen, Y. Zhou, H. Lu, H. Shen, D. Zhang, P. Wang, H. Ming, and G. Yang, *Appl. Opt.* **48**, 375 (2009).
- 25 C. N. Afonso, J. Gonzalo, R. Serna, J. C. G. d. Sande, C. Ricolleau, C. Grigis, M. Gandais, D. E. Hole, and P. D. Townsend, *Applied Physics A: Materials Science & Processing* **69**, S201 (1999).
- 26 V. Resta, *Journal of Applied Physics* **109**, 094302 (2011).
- 27 A. Suárez-García, J. Gonzalo, and C. N. Afonso, *Applied Physics A: Materials Science & Processing* **77**, 779 (2003).

## CHAPTER 5

### **Transmission Electron Microscopy**

Transmission electron microscopy (TEM) is a technique in which a beam of electrons is transmitted through a thin specimen. The electrons interact with the specimen through various mechanisms. An image is then formed from the transmitted electrons collected by sensors, such as a CCD camera. TEM has become an invaluable tool in the field of nanotechnology because of its unique capabilities to provide imaging with atomic-spatial resolution, crystallographic information, and spectroscopic data. Recently, the development of the tools that allow *in-situ* studies now facilitate the observation of processes real-time, thus providing unparalleled insight into physical phenomena.<sup>1</sup>

#### **5.1 Transmission Electron Microscopy**

The wave-particle duality of the electron and strong Columbic interactions are the origin of the electron microscopes' capabilities. Louis de Broglie first presented the idea that electrons have a wave-like nature. Specifically, the electron wavelength is much shorter than that of light and is a function of its energy. This is important because according to the Rayleigh criterion, the smallest feature resolvable is inversely proportional to the wavelength of the probing radiation.

The path of the electrons is determined by electromagnetic lenses that serve to focus the electrons and magnify the image once it has been formed at the objective lens. The condenser lens system controls the illumination of specimen, which is inserted between the

upper and lower pole pieces that make up the objective lens. The objective lens contains the reciprocal space information (diffraction pattern) on its back focal plane, while the real space information (image) is on the image plane. The post objective lenses (intermediate and projection lens system) magnify and determine whether the information from image plane or back focal plane of the objective lens will be projected onto the viewing screen.

### **5.1.1 Imaging Modes in Transmission Electron Microscopy**

Numerous types of electron-specimen interactions occur in the transmission electron microscope that are responsible for provide the contrast in images. Transmitted electrons can experience changes of amplitude and/or phase through specimen interactions. Amplitude contrast can be divided into two classifications, mass-thickness and diffraction. Mass-thickness contrast arises from incoherent (no phase relationship between the incident and scattered electrons) elastic scattering of electrons. Therefore mass-thickness contrast will be generated as a function of changes to atomic number and thickness. Diffraction contrast occurs from coherent elastic scattering. Therefore, diffraction contrast will be generated when Bragg's law ( $n\lambda = 2d \sin \theta$ ) is satisfied. Any change in specimen thickness or crystallographic orientation due to lattice defects, planar defects, and dislocations will produce contrast. Due to diffraction, the electrons will be scattered at specific angles. By inserting an aperture, specifically the objective aperture, into the back-focal plane of the objective lens one can select which electrons will form the final image. By using the objective aperture to select the direct electrons (electrons that remain parallel to the incident beam), the (000) spot, a bright-field image is formed while selecting scattered electrons from

a (hkl) spot will generate a dark-field image. Diffraction can be used not only to generate image contrast but also for structure determination because the angle of scattering in a specimen is directly related to its crystal structure.

Phase contrast is a result of interference of elastically scattered electrons with one another. Therefore multiple beams (electrons that have undergone different scattering events) are required to form an image, and a small objective aperture that prevents multiple beams from being transmitted cannot be used. Since these phase differences of the electron waves after passing through the specimen determine the contrast of the image, it is important that they would remain unperturbed. However the microscope does not do so and convolutes the information as a function of the microscope conditions, as described below. Assuming the sample functions as a weak phase object, the transfer function, in this specific case referred to as the contrast transfer function (CTF) is described by

$$T(\mathbf{u}) = 2A(\mathbf{u})\sin \chi(\mathbf{u}), \quad (5.1)$$

where  $\mathbf{u}$  reciprocal-lattice vector, the spatial frequency for a particular direction,  $A(\mathbf{u})$  is the aperture function and  $\chi(\mathbf{u})$  is the phase distortion function. The phase distortion function strongly depends on how the microscope is configured and is independent of the specimen. The phase distortion function is described by

$$\chi = \pi\Delta f \lambda u^2 + \frac{1}{2} \pi C_s \lambda^3 u^4 \quad (5.2)$$

where  $C_s$  is the coefficient of the spherical aberration and  $\Delta f$  is the extent of defocus. The oscillatory nature of the CTF, as demonstrated in Figure 1, causes contrast reversals, which occur at each zero-crossing. The point resolution is typically expressed in terms of the first

zero crossing of the CTF because it is the smallest directly interpretable spatial frequency, while the information transfer limit is defined as the frequency at which the CTF decays to zero. At each spatial frequency where the CTF crosses zero no information transfer occurs, so to minimize these, the defocus can be balanced against the contribution of the spherical aberration. This defocus value is calculated as

$$\Delta f_{sch} = -1.2(C_s \lambda)^{1/2}, \quad (5.3)$$

and known as the Scherzer defocus. These phase changes coupled with thickness effects make it difficult to directly interpret HRTEM images. The use of computer simulated images and information about the sample are critical for accurate interpretation.

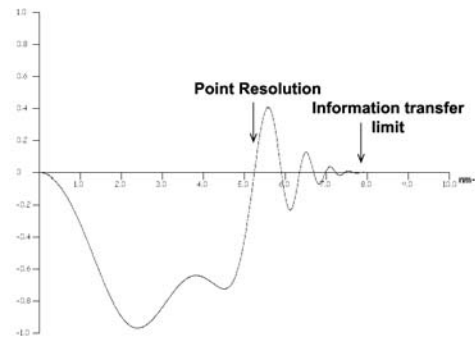


**Figure 1.** Simulated damped contrast transfer function.

## 5.2 Scanning Transmission Electron Microscopy

In scanning transmission electron microscopy (STEM), rather than parallel illumination, a highly focused probe is scanned across the sample. The transmitted electrons are collected by detectors, and an image is generated serially. While the image is made from

scanning the beam across the sample, it still gives an image (contrast) comparable to a TEM image due to the principle of reciprocity, which states that the amplitude of radiation at the point 1 due to a source at point 2 is identical to that, if the source had been placed at point 2 while detecting the radiation at point 1.<sup>2</sup>

### **5.2.1 Imaging Modes in Scanning Transmission Electron Microscopy**

Bright-field images are formed in STEM using the central beam and electrons scattered to low angles ( $< \sim 10$  mrad). These images are similar to bright-field TEM images and contain amplitude and phase contrast. Phase contrast (HRTEM) imaging is possible because interfering beams are present. If an annular detector is used, electrons scattered through specific annular ranges can be collected. If low-angle scattered electrons ( $\sim 10$ -50 mrad) are collected (low-angle annular dark field), the image is analogous to a dark-field TEM image where diffraction contrast dominates. However if images are instead composed of electrons scattered to high angles ( $> 50$  mrad), a technique known as high-angle annular dark-field (HAADF) STEM, the contrast mechanism changes.

In this regime, the image formed is incoherent, and the intensity is a function of atomic number and sample thickness. This imaging mode is appropriately also known as Z-contrast STEM. This occurs because the HAADF detector primarily only collects the electrons that have been scattered through Rutherford and thermal diffuse scattering, which is nearly proportional to the square of the atomic number,  $Z^2$ . The reason for the incoherency in the image, which means no contrast reversals will occur and the atomic positions are directly interpretable, is due to the detector geometry. Lord Rayleigh showed that effectively

incoherent imaging could be achieved with a convergent source of illumination. An analogous situation is obtained in a STEM using a HAADF detector. For each position of the electron probe upon the sample, the detector integrates the distribution of electrons which is analogous to a convergent beam electron diffraction pattern (Figure 2) and gives an image that reflects the total scattered intensity.<sup>3</sup> Integrating over a large annular range essentially averages the transverse coherence effects. Moreover, the thermal vibrations (which cause thermal diffuse scattering) reduce the remaining coherence longitudinal to the beam.<sup>4</sup> The end result is an image whose intensity is directly interpretable, as no contrast reversals exist, and the intensities can be directly correlated to atomic structure.

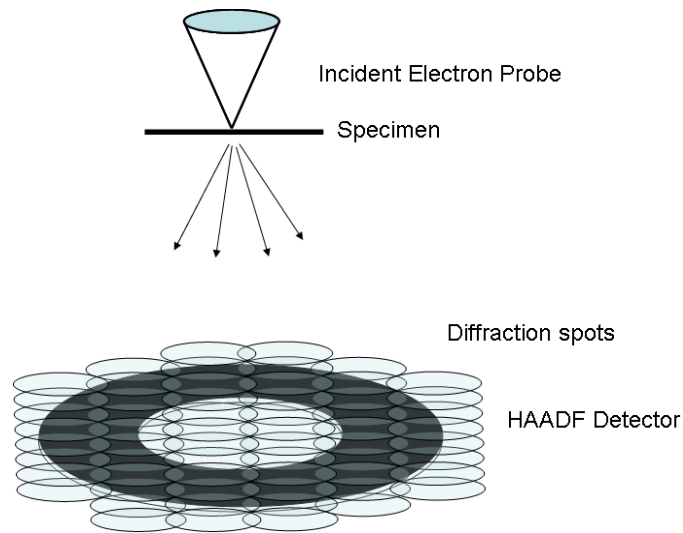


**Figure 2.** Schematic of overlapping diffraction discs on an high-angle annular dark field detector.

The intensity in an incoherent image is the convolution of

$$i(\mathbf{r}) = p^2(\mathbf{r}) \otimes o(\mathbf{r}) \quad (5.4)$$

where  $p(\mathbf{r})$  is the probe function and  $o(\mathbf{r})$  the object function. Since  $i(r)$  depends on  $p(r)$ , the size of the probe is critical for defining the resolution.<sup>5</sup> Therefore, aberrations are the primary factor that limits the resolution. From a wave-optical formulation based on the Scherzer aberration function, one can calculate the best attainable resolution in an uncorrected microscope to be

$$d_0 = 0.43C_s^{1/4} \lambda^{3/4} \quad (5.5)$$

when the convergence angle is optimally tuned.<sup>6</sup>

## REFERENCES

- <sup>1</sup> H. M. Zheng, J. B. Rivest, T. A. Miller, B. Sadtler, A. Lindenberg, M. F. Toney, L. W. Wang, C. Kisielowski, and A. P. Alivisatos, *Science* **333**, 206 (2011).
- <sup>2</sup> J. M. Cowley, *Applied Physics Letters* **15**, 58 (1969).
- <sup>3</sup> S. J. Pennycook and D. E. Jesson, *Physical Review Letters* **64**, 938 (1990).
- <sup>4</sup> P. D. Nellist and S. J. Pennycook, *Ultramicroscopy* **78**, 111 (1999).
- <sup>5</sup> E. M. James and N. D. Browning, *Ultramicroscopy* **78**, 125 (1999).
- <sup>6</sup> M. Weyland and D. A. Muller, *FEI Nanosolutions* **1** (2005).

## CHAPTER 6

### Size-Controlled Synthesis of Cobalt Nanoparticles

#### 6.1 Introduction

Size is a critical parameter in determining the properties of many kinds of materials including magnetic NPs, for which properties such as the superparamagnetic blocking temperature, total moment, coercivity, and interparticle interactions all strongly depend on size. The current prevalent production scheme of monodisperse cobalt NPs can be traced to the late 1990's-early 2000's. In 1999, Sun<sup>1</sup> and Dinega<sup>2</sup> both published reports on the synthesis of a new phase of cobalt, referred to as  $\epsilon$ -cobalt. The structure of  $\epsilon$ -cobalt is cubic (space group  $P4_132$ ) with a unit cell parameter  $a=6.097$  Å and of similar structure to that of  $\beta$ -manganese. The magnetic properties of  $\epsilon$ -cobalt are similar to that of FCC-Co, while the HCP-Co phase has larger magnetocrystalline anisotropy. They cited the tight coordination of alkyl phosphines that were used as the coordinating ligand to change the growth energetics such that this metastable phase formed, though later reports indicate that neither alkyl phosphines<sup>3</sup> nor a wet-chemistry synthetic process<sup>4</sup> are necessary to form the  $\epsilon$ -cobalt phase. A report from 2001 by Puntès<sup>5</sup> integrates the use of trioctylphosphine oxide and oleic acid as the coordinating ligands with the use of dicobalt octacarbonyl as the cobalt precursor and created the synthetic routine that is most widely used and adapted today. The general routine can be described as a hot-injection synthesis where the reagent (dicobalt octacarbonyl) is injected into a hot solvent (1,2 dichlorobenzene) containing coordinating ligands (trioctylphosphine oxide and oleic acid) and rapidly decomposes, thereby producing a

discrete homogeneous nucleation event. The nucleation and subsequent growth is strongly influenced by the coordinating ligands (trioctylphosphine oxide and oleic acid).

The influence of ligands on the growth and nucleation process of Co NPs has been the focus of several previous reports. Both the size and morphology of cobalt nanoparticles can be tuned via the ligands because they influence decomposition of the precursor and NP nucleation and growth. The ratio of the trialkylphosphine ligand (typically trioctylphosphine) and carboxylic acid ligand (typically oleic acid) controls the size. Increasing the ratio of carboxylic acid to trialkylphosphine decreases NP size,<sup>6,7</sup> which has been attributed to the carboxylic acid binding more tightly to the NP surface, thereby slowing the rate of material addition.<sup>1,7</sup> Morphology control is possible as well. Formation of non-spherical NPs has been reported through the use of amine ligands which interact differently with different crystallographic planes of the NPs, hence altering growth rates along specific crystallographic directions.<sup>8-10</sup>

Here, another experimental parameter that can be used to control size of Co NPs is reported. Holding all reaction parameters the same but varying the carbon chain length of unsaturated carboxylic acid-terminated ligands enables direct control of the Co NP size. Subsequently, the size-dependent magnetic properties of the Co NPs were measured, which showed that exchange interactions between the Co core and native oxide shell influence the magnetic properties.

## 6.2 Methods

### 6.2.1 Nanoparticle Synthesis

Co NPs were synthesized by modifying a method by Puntès et al.<sup>5</sup> Syntheses were performed using standard airless (Schlenk) techniques and as-purchased reagents without any further purification. First 11 ml 1,2 dichlorobenzene (DCB, anhydrous, EMD Chemicals) and 0.20 g (0.51 mmol) of trioctylphosphine oxide (TOPO, 99%, Strem) were added to a 100 mL three-necked, round-bottomed flask equipped with a magnetic stir bar. The contents of the flask were degassed for 60 min at room temperature before backfilling with nitrogen. A mixture of 1 ml DCB and 0.62 mmol aliphatic carboxylic acid terminated ligand were then added by syringe. Hexanoic acid (99% Alfa Aesar), dodecanoic acid (99.5%, Alfa Aesar), and docosanoic acid (97%, TCI) were used, which are linear carboxylic acids that consist of chains of 6, 12, and 22 carbons atoms, respectively. Upon heating to 181 °C (the boiling point of DCB), 0.54 g (1.50 mmol) dicobalt octacarbonyl (stabilized with 1-5% hexane, Strem) freshly dissolved in 3.0 mL DCB was quickly injected by syringe. After injection the temperature of the reaction dropped ~30 °C and returned to boiling after ~3 min. The reaction was carried out for a total of ~6 min and was then quenched to room temperature using a water bath. Methanol was added to flocculate the NPs, followed by centrifugation to separate the NPs through sedimentation. The supernatant was discarded, and the NPs were dispersed in hexanes. This process was repeated once more to ensure removal of reaction by-products.

### 6.2.2 Structural Characterization

TEM was used to determine the phase, structure, and size of the NPs. A JEOL 2000FX microscope operating at 200 kV was used to acquire bright-field (BF) images and selected area electron diffraction (SAED) patterns. The camera length was calibrated using an evaporated Al standard (Ted Pella). HRTEM images were acquired on a JEOL 2010F operating at 200kV.

### 6.2.3 Magnetic Characterization

The magnetic properties of the Co NPs were measured using a super conduction quantum interference device (SQUID) magnetometer (Quantum Design MPMS-XL). For magnetometry, NPs were dispersed in a diamagnetic polymer (poly(lauryl methacrylate) cross-linked with ethyleneglycol dimethacrylate) to minimize dipolar coupling.<sup>11</sup> Dried Co NPs were dispersed into a ~1 mL solution of 83% lauryl methacrylate and 17% ethylene glycol, by mass, to which an initiator, 0.40% (by mass), 2,2'-azobisisobutyronitrile (AIBN) was added. The sample was sonicated vigorously to ensure the NPs were dispersed before initiating polymerization. The glass vial containing the solution was then placed in an oven set at 120 °C until the solution had polymerized (~5 min). The sample cooled before it was removed from the vial, cut into small pieces (~ 3 mm × 3 mm × 5 mm) and placed into a plastic drinking straw, which is a standard sample holder for SQUID measurements. The concentration of the NPs was low (~0.1 wt %) and quantitatively measured by inductively coupled plasma optical emission spectroscopy (ICP-OES, conducted by Galbraith Laboratories, Inc.).

Two general types of measurements were performed, magnetization as functions variable or applied field. Temperature-dependent measurements were conducted after first cooling the sample from 300 K to 5 K in zero field. After cooling, a small field of 100 Oe was applied and the moment was measured a function of temperature while warming the samples to 300 K. Use of zero-field during cooling results in “zero-field cooled” measurements, while application of a field during cooling gives “field-cooled” measurements. For field-dependent measurements, ZFC and FC measurements were also performed, in these measurements, the sample was cooled from 300 K to 5 K in zero or an applied field of 50 kOe, respectively. A field of 50 kOe was then applied and the field was incrementally stepped from 50 kOe to -50 kOe and back to 50 kOe, while measuring the magnetic moment of the sample.

## **6.3 Results and Discussions**

### **6.3.1 Structural Properties and Cobalt Nanoparticle Growth Mechanism**

Representative BF TEM images are shown in Figure 1. The average size was determined for each batch of NPs by measuring the diameters of 100 NPs in Image J.<sup>12</sup> The measured NP diameter decreases as the number of carbons atoms in the ligand reduced from 22 (docosanic acid, Figure 1a), 15.6 nm ( $\sigma = 11.7\%$ ), to 12 (dodecanoic acid, Figure 1b), 11.3 nm ( $\sigma = 11.5\%$ ), to 6 (hexanoic acid, Figure 1c), 9.0 nm ( $\sigma = 8.7\%$ ), the relative standard deviation is provided. Electron diffraction indicates the NPs are in the  $\epsilon$ -cobalt phase. A representative diffraction pattern is shown in Figure 2. HRTEM indicates the NPs

have a core-shell structure with a single crystalline  $\epsilon$ -cobalt core and a polycrystalline shell comprised of rocksalt CoO.<sup>13</sup> Representative HRTEM images are shown in Figure 3.

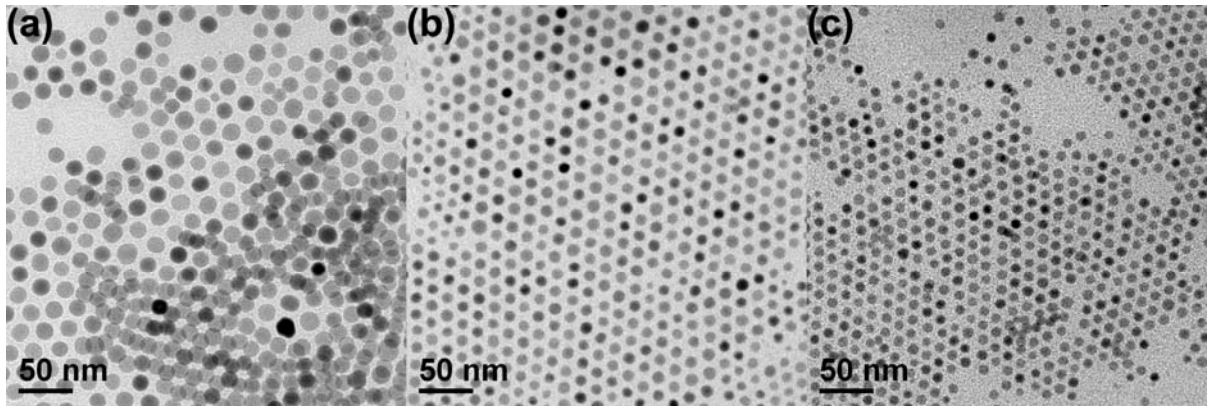


**Figure 1.** Bright-field TEM images of Co nanoparticles synthesized using (a) docosanoic acid, (b) dodecanoic acid, and (c) hexanoic acid.

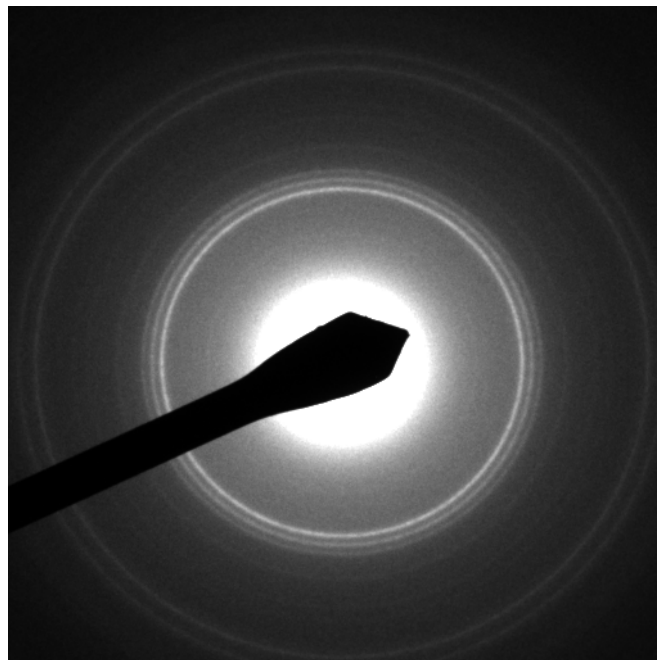


**Figure 2.** Representative selected area electron diffraction pattern of  $\epsilon$ -Co nanoparticles

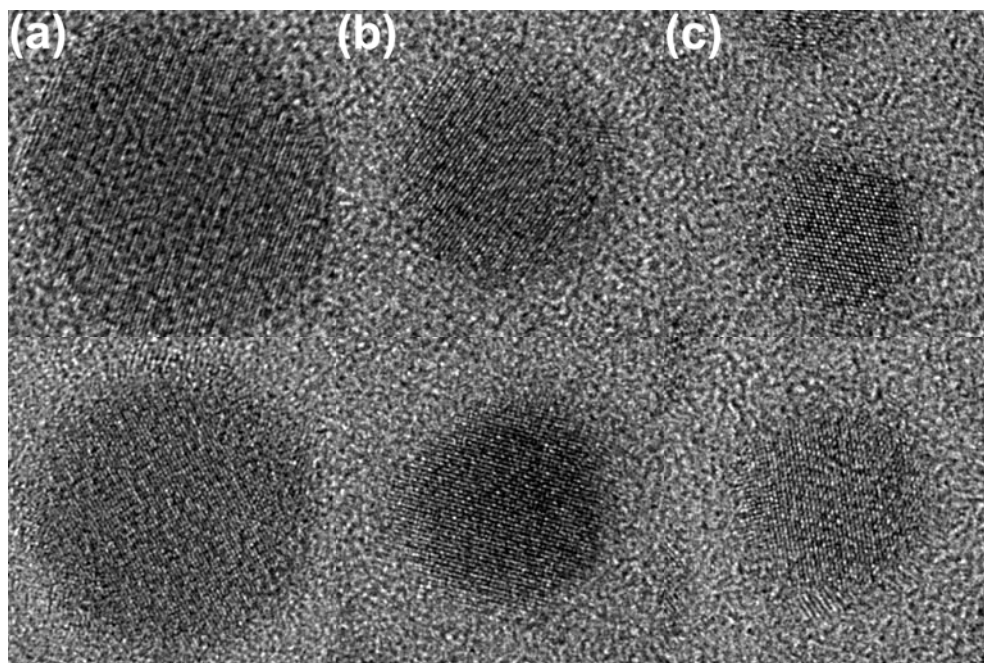


**Figure 3.** HRTEM images of Co nanoparticles synthesized using (a) docosanic acid, (b) dodecanoic acid, and (c) hexanoic acid.

The LaMer model has frequently been used to describe the growth of monodisperse NPs. The model describes a two step process, where a temporally discrete nucleation event is followed by diffusional growth. The single, discrete nucleation step causes uniform growth of all of the NPs, causing a narrow size distribution.<sup>14</sup> The ligands control both the nucleation and growth steps of the process by influencing the decomposition of the precursors, forming ligand-metal complexes, adsorbing to the surfaces of the growing NPs, and facilitating interparticle mass transfer. Since all the of the carboxylic acids have the same structure (linear) expect for the carbon chain length, one can reliably assume that the

strength of bonding interactions between the ligands and cobalt atoms will be the same, but the reactivity will be different because a shorter chain has less steric bulk and is more reactive. The stability of the ligand-metal complexes is expected to depend on the ligand chain length, and the chain length could plausibly alter the structures of the complexes. Furthermore, due to the difference in chain length, the diffusion rate of the species in solution will be different according to the Stokes-Einstein equation. A shape factor applied to the equation will account for changes in hydrodynamic behavior if the ligand does not behave as a sphere.<sup>15,16</sup> As the chain length increases, the self-diffusion coefficient is expected to decrease.

From these considerations, as the carbon chain length of the carboxylic acid decreases, the reactivity of the metal-complexes increases. For shorter chains, this could conceivably provide more free Co atoms for the nucleation event, thereby increasing the level of supersaturation, because ligand-metal complexes are more readily decomposed.<sup>17</sup> Increasing the extent of supersaturation increases the number of NPs formed during the nucleation step.<sup>18</sup> Therefore, as the NPs grow there are more NPs competing for the remaining additional unreacted precursors, and the NPs will not grow as large. Therefore, decreasing carboxylic acid chain length while holding all other reaction parameters constant causes the NP size to decrease. This trend is depicted schematically in Figure 4.

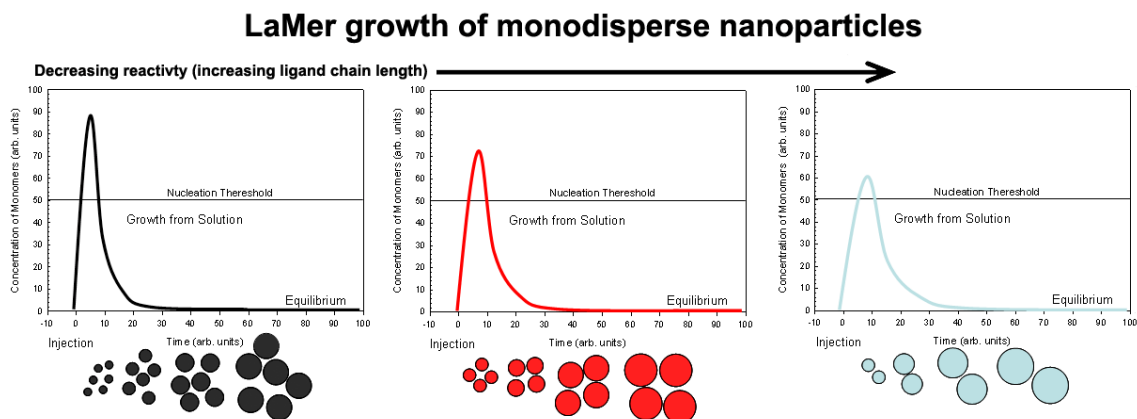


**Figure 4.** Schematic representation of LaMer modeled growth of nanoparticles as a function of a supersaturation. The reactivity of the coordinating ligands determines the extent of supersaturation. As the ligand chain length decreases, the monomer reactivity and supersaturation increases.

### 6.3.2 Magnetic Properties

In SQUID measurements, the polymer contributes a diamagnetic moment to the measurements that must be corrected in the field-dependent measurements. A blank piece of polymer was measured and a correction was applied to remove the diamagnetic background of the polymer from the measurements. The ZFC temperature-dependent magnetization curves are shown in Figure 5. The superparamagnetic blocking temperature of the sample synthesized with hexanoic acid is 150 K, while the superparamagnetic blocking temperatures of the remaining samples are greater than 300 K. Experimental limitations (warping of the plastic straw) prevent measurement of these above 300 K, but approximate superparamagnetic blocking temperatures can be estimated. The magnetic anisotropy constant (assumed to arise from the magnetocrystalline anisotropy) of the hexanoic acid-stabilized Co NPs can be calculated:

$$K = \frac{25T_b k_B}{V} \quad (6.1)$$

where  $T_b$  is the measured superparamagnetic blocking temperature and  $V$  is the NP core (ferromagnet) volume, the NPs were assumed to be spheres and the diameter was determined from the BF-TEM micrographs and magnetic measurements (discussion to follow). The magnetic anisotropy was calculated to be  $3.6 \times 10^6$  erg/cm<sup>3</sup>, which is slightly higher than a previously reported<sup>19</sup> value of  $1.5 \times 10^6$  erg/cm<sup>3</sup>. The magnetocrystalline anisotropy constant depends on temperature, however. The previously reported value was measured at 300 K; generally,  $K$  is expected to decrease as temperature increases. Other anisotropy sources may also influence the measurement, such as exchange anisotropy. Using this value for  $K$  equation 6.1 can be rearranged and solved for approximate  $T_b$  of the other samples. Such calculations give approximate  $T_b$  of 597 K and 1373 K for the dodecanoic and docosanoic acid samples, respectively, which is still below the bulk Curie temperature of Co (1390 K).

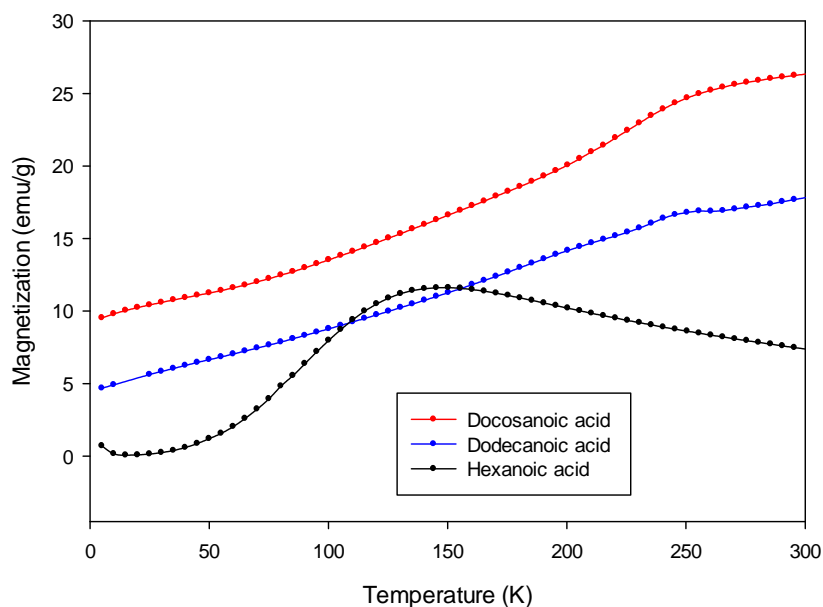


**Figure 5.** Zero-field cooled magnetization as a function of temperature for Co nanoparticles synthesized using carboxylic acids with different chain lengths.

Field-dependent magnetization measurements were performed at 5 K and 300 K (Figures 6 and 7, respectively). At 5 K both ZFC and FC measurements were conducted to discern the presence of exchange bias. The hexanoic acid-stabilized NPs were not measured at 300 K because they are superparamagnetic at that temperature. The saturation magnetization ( $M_s$ ) of each sample was measured to be 59.8, 108.1, and 124.2 emu/g for the hexanoic, dodecanoic, and docosanoic acid samples respectively. These values are significantly less than the  $M_s$  of cobalt, which is 162 emu/g.<sup>20</sup> The significant decrease in  $M_s$  results from formation of an antiferromagnetic surface oxide (CoO) layer that has a very small linear susceptibility. After correcting for the contribution from the CoO shell,  $M_s$  can be used to approximate its thickness using the equation,

$$\frac{N_{Co}}{N_{Co} + N_{CoO}} = \frac{M_{S,measured}}{M_{S,bulkCo}}, \quad (6.2)$$

where  $N_{Co}$  is the average number of Co atoms in an unoxidized core,  $N_{CoO}$  is the average number of Co atoms in the CoO shell, and  $M_{S,BulkCo} = 162$  emu/g. The linear contribution of the antiferromagnetic CoO shells was removed by fitting a straight line to the magnetization curve at high fields and subsequently removing this linear contribution to reveal the saturation magnetization value of the ferromagnetic core. If spherical NPs are assumed then the shell thickness is then given by

$$t_{CoO} = r_{total} \left[ 1 - \left( \frac{M_{S,bulkCo}}{cM_{S,measured}} + 1 - \frac{1}{c} \right)^{\frac{1}{3}} \right] \quad (6.3)$$

where  $c = (\delta_{CoO}/\delta_{Co})(MW_{Co}/MW_{CoO})$  and  $MW$  is the molecular weight and  $\delta$  is the density.

Using the average NP diameter measured from the BF-TEM micrographs, CoO shell thickness (core diameter in parentheses) of 1.6 (5.7), 0.7 (9.8), and 1.4 (12.7) nm were determined for the hexanoic, dodecanoic, and docosanoic acid synthesized samples, respectively.

At 5 K, the coercivity ( $H_C$ ) of the samples increases as the NP diameter decreases (Table 1 and Figure 6). NPs with diameters below the superparamagnetic limit will have coercivities of zero. Upon increasing the NP diameter, the NPs will become ferromagnetic and have non-zero  $H_C$ . Assuming the NP moments reverse magnetization directions coherently, the  $H_C$  will increase with increasing size as described by the Stoner-Wohlfarth model. This increase will continue up to the single domain limit, whereupon multiple

domains form, and the  $H_C$  will decrease. Since the single domain limit of Co (~80 nm) is much larger than the diameters of the NPs reported here, the observed behavior (Table 1) is unexpected. This trend might possibly originate from a transition in the mode of magnetization reversal from coherent to more energetically favorable rotation modes, such as curling,<sup>20</sup> which might cause  $H_C$  to decrease even if the size increases. A more likely explanation, thought to be the case due to the results of the FC field-dependent measurements, is that there is significant exchange anisotropy due to the presence of CoO shells. FC measurements reveal the presence of exchange bias in the hexanoic and dodecanoic acid-stabilized samples but not the docosanoic acid-stabilized sample (Table 1 and Figure 6). In the hexanoic acid-stabilized sample both the increased  $H_C$  and loop shift upon field cooling indicate the presence of exchange coupling. The dodecanoic acid-stabilized sample has an increase in  $H_C$  but no loop shift, regardless, this indicates the presence of exchange coupling. This exchange coupling between the ferromagnetic core and antiferromagnetic shell would increase the magnetic anisotropy of the samples. The docosanoic acid-stabilized sample has neither a significant  $H_C$  enhancement nor loop shift, indicating that exchange coupling is not sufficient to influence the magnetic behavior of the NPs.

While there have been numerous studies on exchange bias in NPs, there are many conflicting accounts. Wide structural variations between or even within studies themselves make it difficult to clearly define structure-property relationships.<sup>21</sup> The general consensus for core/shell NPs is that exchange bias becomes stronger as the core size decreases because direct exchange coupling is an interfacial phenomenon. It is also generally accepted that

exchange bias will increase as the oxide shell thickness increases, up to a critical thickness. These trends agree with the results reported. Furthermore, variations other than differences besides thickness (*e.g.* crystallinity, grain size, and defect density) of the oxide shell will influence the behavior.

Field dependent measurements at 300 K of the dodecanoic and docosanoic acid-stabilized samples reveal the  $H_C$  has significantly decreased in both samples (Table 1 and Figure 7) due to increasing thermal energy. However, the NPs still have finite  $H_C$ , which indicates ferromagnetic behavior and is consistent with values of  $T_b$  above 300 K.

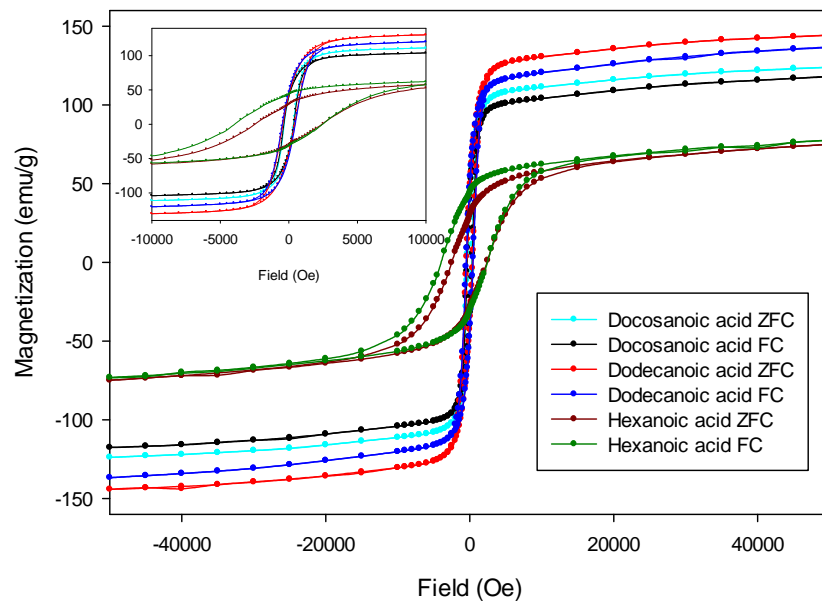


**Figure 6.** Zero- and field-cooled magnetization as a function of field measured at 5 K.

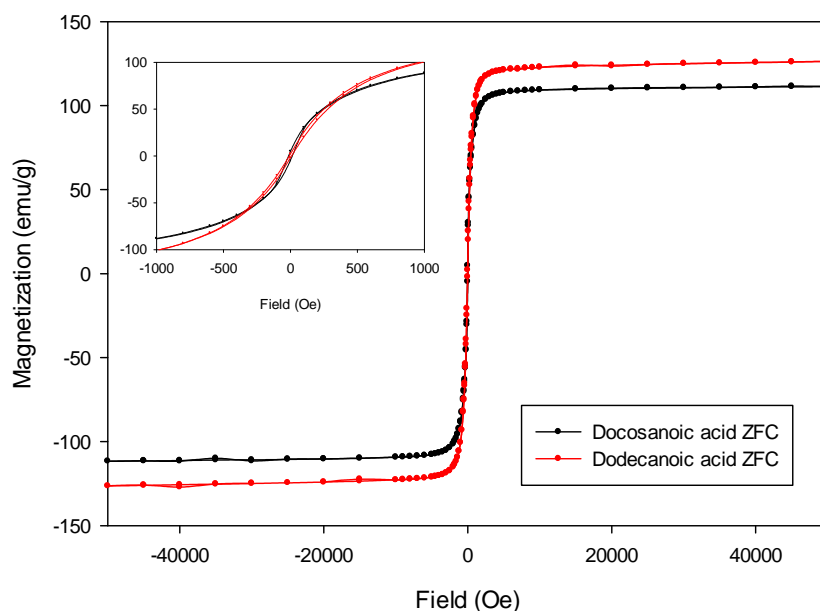


**Figure 7.** Magnetization as a function of field measured at 300 K.

**Table 1.** Magnetic and structural properties of cobalt nanoparticles. The saturation magnetization ( $M_S$ ) values listed are those after accounting for the linear susceptibility of CoO. \*Indicates this was a calculated value, rather than a value measured by SQUID.

	5 K			300 K		$M_S$ (emu/g)	Core Diameter measured from a SQUID and TEM (nm)	Diameter measured by TEM (nm)
	$H_C$ ZFC (Oe)	$H_C$ FC (Oe)	$H_{EB}$ FC (Oe)	$H_C$ ZFC (Oe)	$T_b$ (K)			
Hexanoic	2446	3198	578	-	150	59.8	5.7	9.0
Dodecanoic	432	474	3	9	597*	108.1	9.8	11.3
Docosanoic	332	332	0	14	1373*	124.2	12.7	15.6

## 6.4 Conclusions

Monodisperse Co NPs can be produced by modifying an existing synthetic method. The NP size can be controlled by varying the chain length of the linear carboxylic acid ligand used during synthesis. The chain length influences the reactivity of the ligand-metal complex intermediates, that form which controls the supersaturation level of the solution before nucleation and dictates the number of nuclei formed and the eventual size of the NPs after growth. Magnetic measurements reveal significant size-dependent magnetic properties. As the NPs increase in size, they become less susceptible to superparamagnetism. The magnetic anisotropy of the NPs increases with decreasing size due to presence of exchange anisotropy. Exchange bias was observed in the two samples with the smallest NP sizes, while no effects were observed for the largest sample NP sizes. This is due variations in the NP structure (CoO oxide shell thickness, Co/CoO interface, the ratio of ferromagnetic core diameter to antiferromagnetic shell thickness) which manifest itself in the ability of the antiferromagnetic shell to facilitate exchange bias.

## REFERENCES

- 1 S. Sun and C. B. Murray, *Journal of Applied Physics* **85**, 4325 (1999).
- 2 D. P. Dinega and M. G. Bawendi, *Angewandte Chemie-International Edition* **38**, 1788 (1999).
- 3 P. Y. Keng, I. Shim, B. D. Korth, J. F. Douglas, and J. Pyun, *Acs Nano* **1**, 279 (2007).
- 4 X. Nie, J. C. Jiang, E. I. Meletis, L. D. Tung, and L. Spinu, *Journal of Applied Physics* **93**, 4750 (2003).
- 5 V. F. Puentes, K. M. Krishnan, and A. P. Alivisatos, *Science* **291**, 2115 (2001).
- 6 Y. K. Su, C. M. Shen, T. Z. Yang, H. T. Yang, H. J. Gao, and H. L. Li, *Applied Physics a-Materials Science & Processing* **81**, 569 (2005).
- 7 C. B. Murray, S. H. Sun, W. Gaschler, H. Doyle, T. A. Betley, and C. R. Kagan, *IBM Journal of Research and Development* **45**, 47 (2001).
- 8 N. Shukla, E. B. Svedberg, J. Ell, and A. J. Roy, *Materials Letters* **60**, 1950 (2006).
- 9 R. M. de Silva, V. Palshin, K. M. N. de Silva, L. L. Henry, and C. Kumar, *Journal of Materials Chemistry* **18**, 738 (2008).
- 10 V. F. Puentes, D. Zanchet, C. K. Erdonmez, and A. P. Alivisatos, *Journal of the American Chemical Society* **124**, 12874 (2002).
- 11 J. B. Tracy, D. N. Weiss, D. P. Dinega, and M. G. Bawendi, *Physical Review B* **72**, 064404 (2005).
- 12 W. S. Rasband, (U. S. National Institutes of Health, Bethesda, MD, 1997-2011).
- 13 N. Braidy, S. Behal, A. Adronov, and G. A. Botton, *Micron* **39**, 717 (2008).
- 14 V. K. Lamer and R. H. Dinegar, *Journal of the American Chemical Society* **72**, 4847 (1950).
- 15 J. G. Delatorre and V. A. Bloomfield, *Quarterly Reviews of Biophysics* **14**, 81 (1981).
- 16 D. F. Evans and H. Wennerström, *The Colloidal Domain: Where Physics, Chemistry, Biology, and Technology Meet*, 2nd ed. (Wiley-VCH, New York, 1999).

- <sup>17</sup> Y. Bao, W. An, C. H. Turner, and K. M. Krishnan, *Langmuir* **26**, 478 (2010).
- <sup>18</sup> J. Park, J. Joo, S. G. Kwon, Y. Jang, and T. Hyeon, *Angewandte Chemie-International Edition* **46**, 4630 (2007).
- <sup>19</sup> V. F. Puentes and K. M. Krishnan, *IEEE Transactions on Magnetics* **37**, 2210 (2001).
- <sup>20</sup> R. C. O'Handley, *Modern Magnetic Materials: Principles and Applications* (John Wiley & Sons, Inc., New York, 2000).
- <sup>21</sup> J. Nogués, J. Sort, V. Langlais, V. Skumryev, S. Suriñach, J. S. Muñoz, and M. D. Baró, *Physics Reports* **422**, 65 (2005).

## CHAPTER 7

# **Synthesis and Structural and Magnetic Characterization of Ni(core)/NiO(shell) Nanoparticles**

The following material was published in *ACS Nano* (Vol. 3, No. 5, pp. 1074-1084, 2009) as “Synthesis and Structural and Magnetic Characterization of Ni(Core)/NiO(Shell) Nanoparticles” by Aaron C. Johnston-Peck, Junwei Wang, and Joseph B. Tracy. Johnston-Peck’s contribution to the manuscript included collecting and analyzing the TEM and SQUID data and writing the manuscript.

### **7.1 Motivation**

In BPM, decreasing the bit size significantly increases the storage density. Therefore, small bits are highly desirable, but bit size reduction must not cause the NPs to become superparamagnetic. Therefore, it is imperative that the magnetic anisotropy of the NPs be sufficiently large to support ferromagnetism at room-temperature and above. The intrinsic anisotropy of a ferromagnetic is its magnetocrystalline anisotropy. If one would only consider materials with exceptionally high magnetocrystalline anisotropy, the number of potential materials is extremely limited. Rather than utilizing such a limited set of materials, other ways exist to increase the magnetic anisotropy. For instance, exchange anisotropy, a result of the exchange interaction between a ferromagnet and antiferromagnet, could also be used to increase the magnetic anisotropy of a ferromagnet. Antiferromagnets generally have

higher magnetocrystalline anisotropies than ferromagnets, which make this approach feasible, such that the coupled ferromagnets will have the requisite extrinsic magnetic anisotropy for BPM. The objective of was to demonstrate control of NP size and oxide shell thickness and to investigate their influence on the magnetic properties of the Ni/NiO NPs.

## **7.2 Manuscript Reprint**

# Synthesis and Structural and Magnetic Characterization of Ni(Core)/NiO(Shell) Nanoparticles

Aaron C. Johnston-Peck, Junwei Wang, and Joseph B. Tracy\*

Department of Materials Science and Engineering, North Carolina State University, Raleigh, North Carolina 27695

Core/shell nanoparticles (NPs) composed of cores and shells with distinctly different compositions can be engineered for special properties that are not available in unary-core NPs. Important examples of useful core/shell NPs include (1) CdSe(core)/ZnS(shell), where the ZnS shell confines excitons to the CdSe, which increases the quantum yield and reduces luminescence from surface traps;<sup>1,2</sup> (2) Fe<sub>3</sub>O<sub>4</sub>(core)/Au(shell) NPs, where the Au imparts a tunable surface plasmon resonance absorbance and facile surface coupling chemistry through use of thiols;<sup>3</sup> (3) Co(core)/CoO(shell) NPs exhibiting exchange bias,<sup>4–12</sup> an effect in which the anti-ferromagnetic CoO shells enhance the effective magnetic anisotropy of the Co cores.<sup>13–18</sup> Ferromagnet(core)/antiferromagnet(shell) NPs are of particular interest for their potential to overcome the superparamagnetic limit for ultrahigh-density magnetic recording,<sup>7</sup> to enhance contrast in magnetic resonance imaging,<sup>19</sup> and for potential uses in spintronic devices, such as spin valves.<sup>20</sup>

Here, we report the *solution-phase* synthesis and controlled oxidation of *ligand-stabilized* Ni NPs of different sizes to form Ni(core)/NiO(shell) NPs with different core sizes and shell thicknesses. The magnetic properties of these NPs are of particular interest, because ferromagnetic Ni is converted to antiferromagnetic NiO, which can give rise to exchange bias. Ligand-stabilized NPs may also self-assemble into highly ordered superlattice crystals or films, or they may be biofunctionalized for medical applications.<sup>21</sup> Most of the Ni/NiO NPs previously studied cannot self-assemble or undergo biofunctionalization, because they lack ligand stabilization and are already agglomerated or pinned to surfaces. Detailed

www.acsnano.org

**ABSTRACT** A size series of ligand-stabilized Ni nanoparticles (NPs) with diameters between 8–24 nm was prepared by solution chemistry, followed by solution-phase oxidation with atmospheric oxygen at 200 °C to form Ni(core)/NiO(shell) NPs with shell thicknesses of 2–3 nm. In comparison with the oxidation of Fe and Co NPs, Ni NPs require higher temperatures for significant conversion to NiO. Transmission electron microscopy and electron diffraction show polycrystalline cores with predominantly amorphous shells. SQUID magnetometry measurements were performed to assess the effects of coupling between the ferromagnetic Ni cores and antiferromagnetic NiO shells. After intentional oxidation, the Ni(core)/NiO(shell) NPs have decreased superparamagnetic blocking temperatures ( $T_B$ ) and no exchange shift ( $H_{EB}$ ), but a small enhancement in the coercivity ( $H_C$ ) signifies weak exchange bias. These effects originate from the amorphous structure of the NiO shells and their thin layer thickness that renders the NiO moments incapable of pinning the core moment in moderate applied fields. The magnetocrystalline anisotropy constants before and after oxidation approach the value for bulk Ni and depend on the Ni core size and NiO shell thickness.

**KEYWORDS:** magnetic nanoparticles · exchange bias · nickel · nickel oxide · superparamagnetism · magnetic anisotropy

structural and magnetic characterization of our Ni(core)/NiO(shell) NPs is presented, and the relationship between the magnetic properties and nanostructure is discussed. Beyond magnetism, there is substantial interest in Ni NPs for catalysis of chemical reactions<sup>22</sup> and growth of carbon nanotubes<sup>23</sup> and nanofibers.<sup>24</sup> NiO has also been used as a hole-transport layer in LEDs.<sup>25</sup>

Exchange bias occurs when a ferromagnet (FM) shares an interface with an antiferromagnet (AFM) having a larger magnetic anisotropy, and the AFM pins the orientation of the moment in the FM layer (through the exchange interaction). Despite vigorous research into the microscopic mechanism of EB since its initial discovery<sup>26</sup> and renewed interest following the advent of spin valves, in which EB can be used to pin one magnetic layer, much understanding of EB at the microscopic level and the factors determining the strength of its pinning interaction remain incomplete. EB is manifested in field-dependent magnetometry

\*Address correspondence to jbracy@ncsu.edu.

Received for review January 8, 2009 and accepted April 02, 2009.

Published online April 10, 2009.  
10.1021/nn900019x CCC: \$40.75

© 2009 American Chemical Society

VOL. 3 ■ NO. 5 ■ 1077–1084 ■ 2009 ACSNANO

1077

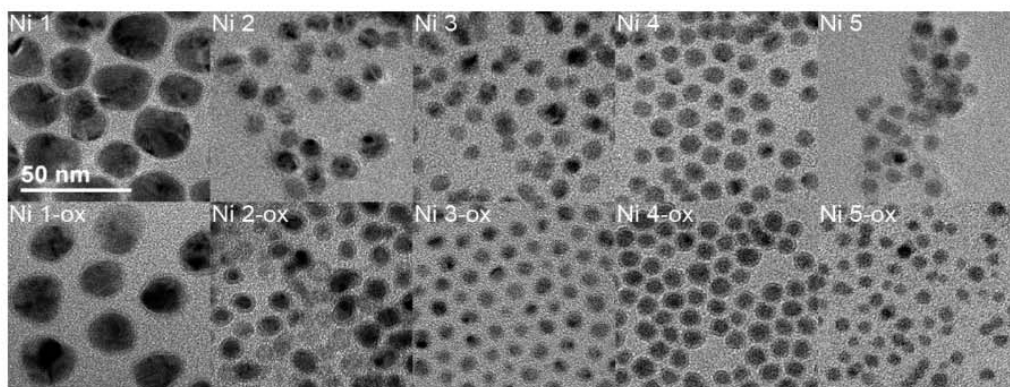


Figure 1. TEM images of Ni nanoparticles: (top row) native samples; (bottom row) oxidized samples.

as an enhanced coercivity ( $H_C$ ) and an asymmetric shift in the center of the hysteresis loop, the exchange shift ( $H_{EB}$ ), that depends on the magnitude and direction of an externally applied field during cooling.<sup>4,27</sup> To obtain nonzero  $H_{EB}$ , the pinning must be maintained at all field strengths,  $H < H_{max}$  that are applied during the measurement of a hysteresis loop. If the pinning fails at an intermediate field,  $0 < H_{int} < H_{max}$ , then  $H_{EB} = 0$ , and  $H_C$  cannot be enhanced above  $H_{int}$ . EB depends on temperature:  $H_C$  and  $H_{EB}$  usually decrease as temperature increases. EB is not possible above the Néel temperature ( $T_N$ ) of the AFM, at which the antiferromagnetic moments disorder and become paramagnetic.

Previous studies of Co/CoO<sup>4–12</sup> and Fe<sub>x1</sub>O<sub>y1</sub>/Fe<sub>x2</sub>O<sub>y2</sub><sup>28–32</sup> NPs and Ni/NiO NPs<sup>33–45</sup> and nanowires<sup>46</sup> have shown that the antiferromagnetic layer can enhance the magnetic anisotropy of the ferromagnet and, in some cases, can stabilize the fixed orientations of ferromagnetic moments to higher temperatures before thermal energy causes the moments' orientations to fluctuate (superparamagnetism). Moreover, oxides of Co, Fe, and Ni can be prepared through oxidation in air (sometimes requiring elevated temperatures). Although oxidized Fe and Co NPs exhibit novel and potentially useful magnetic properties, both systems also have significant limitations: Controlled oxidation of Fe NPs is challenging, owing to the high reactivity of metallic iron and the diverse iron oxide stoichiometries available.<sup>47</sup> Large EB effects are observed in Co/CoO, but  $T_N$  for bulk Co of 290 K<sup>16</sup> severely limits its potential for use in devices that operate at room temperature. In contrast, NiO is a candidate for producing useful EB at room temperature, because bulk NiO has  $T_N$  of 520 K.<sup>16</sup> Values for  $T_N$  are known to depend on the layer thickness; for crystalline NiO thin films of thickness 2 nm,  $T_N \approx 400$  K.<sup>48,49</sup> There have also been several reports of the synthesis and magnetic properties of NiO NPs.<sup>22,50–57</sup>

For this investigation, several sizes of Ni(core)/NiO(shell) NPs with diameters of 8–24 nm were synthesized through thermolysis of nickel acetylacetonate in the presence of oleylamine and trioctylphosphine to generate ligand-stabilized Ni NPs.<sup>21</sup> Through controlled oxidation with air, two different NiO shell thicknesses were obtained. Conventional and high-resolution transmission electron microscopy (TEM and HRTEM) measurements reveal narrow size distributions, polycrystalline cores, and amorphous shells. SQUID magnetometry measurements show the effects of size and the NiO shell thickness on the magnetic properties.

## RESULTS AND DISCUSSION

**Nanoparticle Growth and Oxidation.** Each NP size was prepared in a single batch to minimize batch-to-batch variations. After postsynthesis processing to remove high-boiling solvent and excess ligands (performed in the glovebox to minimize oxidation), each batch was split in half. One portion containing “native” NPs with minimal oxidation was used as-is. The other half, the oxidized sample, was redispersed into dioctyl ether for oxidation by bubbling air through the solution at 200 °C for 4 h.<sup>11,58</sup> Both the native and oxidized samples were dispersed into polymer sticks for SQUID magnetometry measurements<sup>11,59</sup> to minimize the effects of dipolar coupling and thus to measure the magnetic properties of noninteracting NPs. (Photographs of polymer sticks containing Ni NPs are shown in the Supporting Information, Figure S-1.) Several studies have highlighted the importance of a matrix to increase the interparticle distances; without use of a matrix, dipolar coupling contributes to a significant increase in the superparamagnetic blocking temperatures ( $T_B$ ).<sup>60–64</sup>

**Structural Characterization.** TEM, HRTEM, and selected-area electron diffraction (SAED) were performed to measure the NP size, to characterize the crystallinity and crystal structure, and to image the NiO shells. Rep-

**TABLE 1. Average Ni Core Diameter and NiO Shell Thickness**

sample	$d_{\text{total,TEM}}$ (nm)	native		oxidized	
		$d_{\text{core}}$ (nm)	$t_{\text{shell}}$ (nm)	$d_{\text{core}}$ (nm)	$t_{\text{shell}}$ (nm)
Ni 1	23.8 ± 2.6	22.6	0.6	18.6	2.6
Ni 2	10.3 ± 1.6	7.9	1.2	7.3	1.5
Ni 3	8.2 ± 0.8	6.6	0.8	6.1	1.1
Ni 4	8.8 ± 0.9	6.4	1.2	4.4	2.2
Ni 5	7.6 ± 0.5	5.3	1.1	2.8	2.4

representative images of each NP sample before (Ni x) and after oxidation (Ni x-ox) treatment (Figure 1) show clearly identifiable NiO shells for several samples. The nonuniform contrast in the TEM images indicates that the cores are polycrystalline, as we have verified by HR-TEM (Supporting Information, Figure S-2) images of the crystal lattice. SAED (Supporting Information, Figure S-3) confirms the particles are face-centered-cubic (fcc) Ni and do not show the presence of any other crystalline phases, including NiO. We note that a synthetic method from which ours is derived (and which is quite similar to ours) is known to lead to amorphous or highly polycrystalline fcc Ni NPs,<sup>22</sup> and others have reported similarly disordered structures.<sup>65–67</sup> TEM and HRTEM further suggest that the NiO shells are mostly amorphous, because we observe crystal lattice only over small regions within the NiO shells, and in conventional TEM, the NiO shells had predominantly uniform contrast. We note that since we cannot measure a lattice parameter for the amorphous oxide, we have not rigorously verified the stoichiometry of the oxide phase as NiO. NiO is, however, the only well-characterized oxide of nickel, which is known to have slight stoichiometric variations from 1:1,<sup>68</sup> and the oxide phase is generally reported as NiO.

NP sizes (Table 1) were determined by manually measuring<sup>69</sup> the diameter of each particle twice and then taking the average value for more than 200 NPs for each native NP sample. Histograms of the NP size distributions are shown in the Supporting Information, Figure S-4. The NiO shell thickness was calculated from a combined TEM measurement of the total NP diameter and the reduction of the saturation magnetization below the bulk value ( $M_{\text{S,BULKNi}}$ ), of 57.2 emu/g at 2.5 K,<sup>70</sup> as described in the Supporting Information. (Alternately, the shell thicknesses for most samples can be measured by TEM, but with less accuracy, because Ni NPs on TEM substrate films are more susceptible to oxidation than NP samples for magnetometry measurements that were dispersed in polymers and were stored in a glove-box.)

The native NPs had thin NiO surface layers ranging in thickness (0.6–1.2 nm). After performing intentional oxidation, the NiO shell thickness increased to 1.1–2.6 nm. Extended oxidation times at 200 °C do not increase the shell thickness, which suggests that NiO layers of

2–3 nm thickness form a passivating layer<sup>36</sup> that prevents further oxidation at 200 °C. *In comparison with oxidation of Fe and Co NPs, conversion of Ni to NiO in nanoparticle form requires more driving force:* Fe NPs quickly oxidize upon exposure to air at room temperature.<sup>71</sup> Co NPs can form from Co(core)/CoO(shell) NPs upon room temperature exposure to air<sup>4,11</sup> and can be converted to hollow, crystalline CoO NPs at temperatures below 200 °C.<sup>11,58</sup>

**Magnetic Characterization.** SQUID measurements (Quantum Design MPMS-XL7 magnetometer) of the temperature- and field-dependent magnetizations of each NP sample, dispersed in the polymer matrix, were acquired to assess the superparamagnetic blocking temperature ( $T_B$ ), magnetic hysteresis ( $M_S$  and  $H_C$ ), and exchange bias ( $H_C$  and  $H_{\text{EB}}$ ). The magnetization units of emu/g are based on the mass of nickel; the mass of oxygen in NiO and of the ligands is excluded.

For each native/oxidized (Ni x/Ni x-ox) pair of samples, the oxidized sample was prepared from the native sample, which eliminated the possibility of batch-to-batch variations and ensured that each pair had the same size (before oxidation) and the same size distribution. The chief aim of the magnetic measurements was to perform pairwise comparison of each oxidized sample (Ni x-ox) with a minimally oxidized reference (Ni x) to discern the effects of oxidation. Comparisons between the whole sets of native and oxidized samples must be interpreted cautiously because of variations of the NiO thicknesses within each set. There is also partial overlap among the native and oxidized samples: Ni 2, Ni 4, Ni 5, Ni 2-ox, and Ni 3-ox all have NiO shell thicknesses of 1.1–1.5 nm.

Measurements of the temperature-dependent magnetization ( $M$  vs  $T$ ) acquired in a 100 Oe field during heating after zero-field cooling (ZFC) are shown in Figure 2. At  $T_B$ , the ferromagnetic moment within each NP decouples from the crystal lattice and becomes superparamagnetic. For dc SQUID measurements,  $T_B$  is typically chosen as  $T_B = KV/(25k_B)$ , such that the magnetocrystalline anisotropy energy ( $KV$ ) is much greater than thermal energy, where  $V$  is the ferromagnetic core volume.<sup>72</sup> Experimentally,  $T_B$  is measured as the temperature corresponding to the peak in  $M$  versus  $T$ : the magnetization reaches a maximum when thermal energy facilitates reorientation of NP moments into the small applied field but is not so large that it randomizes NP moments' orientations. As expected, in our measurements,  $T_B$  decreases with decreasing core size, which can be achieved by choosing a greater extent of oxidation or by choosing a batch of NPs with a smaller total diameter.

Measurements of  $M$  versus  $H$  for each sample (Figure 3) were performed at 2.5 K while scanning the field from 50 to –50 kOe, and then back to 50 kOe after cooling from room temperature in 50 kOe field (FC) or zero field (ZFC). Values of  $M_S$  and  $H_C$  at 2.5 K are reported in

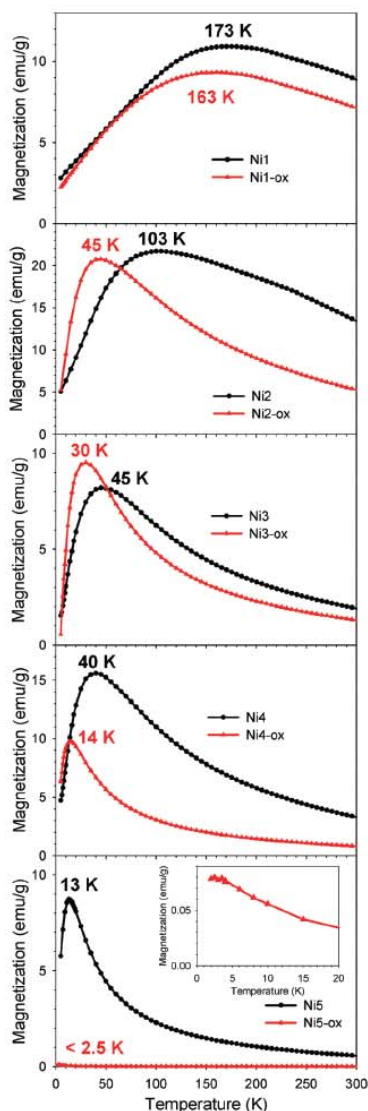


Figure 2.  $M$  vs  $T$  after cooling in zero field for native and oxidized Ni(core)/NiO(shell) NPs. The inset (bottom panel) shows greater detail of the low-temperature region. Labels indicate  $T_B$  for each sample.

Table 2, and the size-dependence of  $H_C$  is plotted in Figure 4. After applying a linear correction for the diamagnetic magnetization of the polymer, the magnetization for most samples did not saturate asymptotically to a fixed value. At high fields, the slope of  $M$  versus  $H$  was greater for the oxidized samples, because antiferromagnetic NiO magnetizes in the field direction but does not saturate in a 50 kOe field.<sup>22,50–57</sup> The oxidized samples show a greater deviation from ferromagnetic saturation behavior, because they have greater NiO

content than the native samples. For calculating the saturation magnetization of the Ni cores ( $M_{S, Ni}$ ), a line of slope  $k_i$  was fit to the ZFC magnetization for each sample at high fields, and then a line intersecting the origin with slope  $-k_i$  was added to the magnetization to remove the magnetization of NiO. This forced asymptotic saturation behavior at high fields, from which  $M_S$  was obtained. For greater extents of oxidation,  $M_S$  systematically decreases due to the lower unoxidized Ni content.

For all samples, there is no exchange shift at 2.5 K, even with 50 kOe field cooling, and for each sample except the largest size,  $H_C$  is slightly larger after oxidation, which originates from an *enhanced anisotropy consistent with weak exchange bias*. Plots of  $H_C$  versus  $d_{core}$  (Figure 4) also show that for a given core size,  $H_C$  is greater with a thicker NiO shell. A comparison of  $H_C$  for 50 kOe and zero-field cooling (Table 2) shows rather small differences in  $H_C$ , which is consistent with no exchange shift, because the NiO shell is unable to remember any specific pinning orientation. Other studies have shown that NiO NPs of 5 nm diameter have significant  $H_{EB}$ ,<sup>50,73,74</sup> and  $H_{EB}$  of 80 Oe at 5 K<sup>38</sup> has been reported for crystalline<sup>36</sup> Ni(core)/NiO(shell) NPs with  $\sim 2$  nm shells, which suggests that *the reduction in the magnetic anisotropy causing  $H_{EB}$  to vanish primarily originates from the amorphous structure of our NiO shells*. A thicker amorphous NiO layer would be needed to provide the same pinning strength as a thinner, crystalline NiO layer, because structural disorder in amorphous NiO reduces its ability to pin the Ni core. However, defects and partial disorder within crystalline antiferromagnets can enhance EB.<sup>13</sup> In a related study of Ni/NiO NPs, EB pinning of the Ni phase originated from coupling with a spin-glasslike, disordered NiO phase.<sup>44</sup>

We have also considered that  $T_N$  is reduced for thin layers of NiO, and the amorphous structure could cause a further reduction in  $T_N$ . Such lowering of  $T_N$  alone is probably insufficient to cause  $H_{EB}$  to vanish at 2.5 K. For crystalline NiO films of 2 nm thickness,  $T_N \approx 400$  K,<sup>48,49</sup> and structural disorder in the amorphous NiO is expected to further reduce  $T_N$ , but  $T_N < 2.5$  K for amorphous NiO remains rather unlikely. The absence of an exchange shift at a particular temperature  $T_0$  does not imply  $T_N < T_0$ . Pinning through EB can fail above  $T_N$  if the NiO moments cant or flip when moderate magnetic fields are applied,<sup>13,18,75</sup> or the amorphous NiO shells may be superparamagnetic even at 2.5 K due to a lowered magnetocrystalline anisotropy. We note that  $K_{NiO}$  is generally substantially less than  $K_{CoO}$ .<sup>76</sup> Therefore, the minimum thickness giving rise to EB at a particular temperature should be thinner for CoO rather than for NiO.<sup>18,77</sup> Indeed, this is the case; prior results show significant EB in Co(core)/CoO(shell) NPs having CoO thicknesses of 3 nm.<sup>11</sup>

The size-dependence of  $T_B$  allows for measurements of magnetocrystalline anisotropy constants and an as-

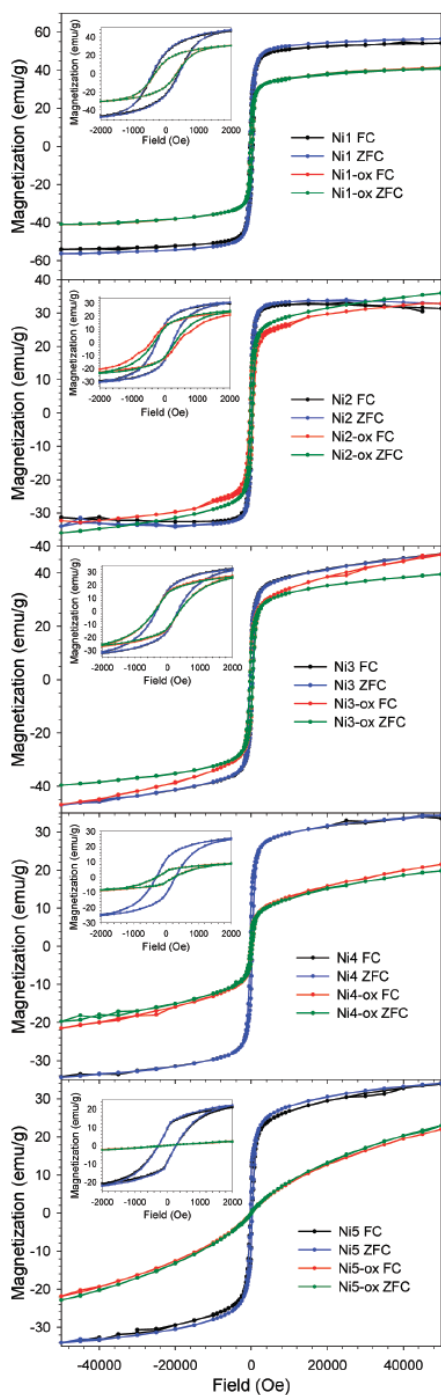


Figure 3.  $M$  vs  $H$  at 2.5 K for native and oxidized Ni(core)/NiO(shell) NPs after cooling from room temperature in 50 kOe field (FC) or zero field (ZFC). Insets show greater detail of the same measurements.

www.acsnano.org

TABLE 2. Saturation Magnetization and Coercivity at 2.5 K with 50 kOe or Zero-Field Cooling

sample	native			oxidized		
	$M_s$ (emu/g)	$H_{CFC}$ (Oe)	$H_{CFC}$ (Oe)	$M_s$ (emu/g)	$H_{CFC}$ (Oe)	$H_{CFC}$ (Oe)
Ni 1	52.0	411	390	34.5	334	328
Ni 2	33.7	248	249	27.5	319	319
Ni 3	36.7	332	331	31.1	379	383
Ni 4	28.9	292	291	10.9	274	263
Ni 5	26.8	271	275	4.6	33	30

assessment of the relative strengths of other sources of anisotropy (surface anisotropy<sup>78</sup> and EB). The blocking temperature was previously introduced as  $T_B = KV/(25k_B)$  for a system exhibiting magnetocrystalline anisotropy only. To account for surface anisotropy and EB, an additional term,  $f(V, T, t_{shell})$ , can be added, giving:  $T_B = KV/(25k_B) + f(V, T, t_{shell})$ . When magnetocrystalline anisotropy is predominant, plots of  $T_B$  versus  $V$  (Figure 5) are expected to be linear and to have slope  $KV/(25k_B)$ . For these plots, the core volume has been calculated for spheres with the diameters reported in Table 1. The intercept term and sources of nonlinearity are attributed to  $f(V, T, t_{shell})$ . An important limitation of this analysis is that it assumes  $K$  does not depend on temperature, because each blocking temperature is measured when  $T = T_B$ . The magnetocrystalline anisotropy constants for bulk Ni ( $K_{Ni,bulk}$ ) are known to have a significant temperature dependence (more than an order of magnitude decrease from 2.5 to 300 K).<sup>79</sup> Two other limitations restrict the accuracy of this approach: Higher-order magnetocrystalline anisotropy constants are neglected, and the factor of 25 is an approximation that could be eliminated by performing ac SQUID measurements.<sup>11</sup>

For the native and oxidized samples,  $T_B$  versus  $V$  is linear for all samples except Ni 5 and Ni 5-ox, which are expected to lie below the linear fit, because their blocking temperatures are significantly higher than those for all the other samples, at which  $K$  is significantly below its low-temperature value. From linear fits to the four smallest sizes for each sample, we have measured  $K_{native} = 1.7 \times 10^6$  erg/cm<sup>3</sup> and  $K_{oxidized} = 7.5 \times 10^5$  erg/cm<sup>3</sup>. Both of these values agree well with the bulk value,  $K_{Ni,bulk} \approx 1 \times$

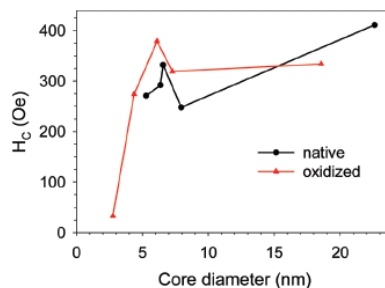


Figure 4. Ni core-size dependence of the coercivity (zero-field cooled).

VOL. 3 ■ NO. 5 ■ 1077–1084 ■ 2009 ACS NANO

1081

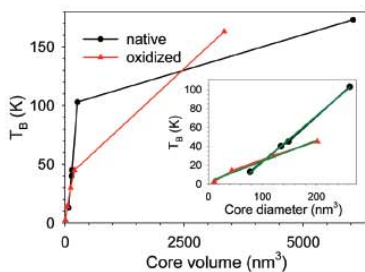


Figure 5. Dependence of  $T_b$  on the Ni core volume. Inset shows the same plot, omitting the two data points for samples with the largest volumes (Ni 5 and Ni 5-ox). Linear fits are shown in green.

$10^6$  erg/cm<sup>3</sup>, below 100 K,<sup>79</sup> but it is remarkable that  $K_{\text{native}} > K_{\text{oxidized}}$ . In particular, we note that  $H_{C,\text{native}} < H_{C,\text{oxidized}}$  for cores of the same size (except for the largest sizes). This trend for  $H_C$  to increase during oxidation while  $K$  decreases violates the Stoner–Wohlfarth<sup>80</sup> model for the hysteresis of single-domain ferromagnetic NPs that predicts  $H_C = 2K/M_s$ . Oxidation appears to reduce the surface anisotropy (lowering  $K$ ) while increasing the ex-

change bias (which increases  $H_C$ ). The linear regressions also have rather different intercept terms on the temperature axis:  $T_{0,\text{native}} = -26$  K, and  $T_{0,\text{oxidized}} = 2$  K. The temperature dependence of  $K$  and contributions from other anisotropy sources prevent further interpretation of the difference in intercepts.

## CONCLUSIONS

In summary, synthetic control over the core size and shell thickness of ligand-stabilized Ni(core)/NiO(shell) NPs has been demonstrated, with maximum shell thicknesses of 2–3 nm. For a given batch of NPs, greater extents of oxidation cause reduction in  $T_b$  due to the smaller core volume, but there is also a small enhancement in  $H_C$  at low temperature from weak exchange bias that does not cause an exchange shift. The amorphous structure of the NiO shells combined with their thin thickness renders the shells unable to support the interfacial pinning strength necessary for an exchange shift. Magnetocrystalline anisotropy constants for the Ni cores calculated from  $T_b$  are consistent with bulk values, but oxidation causes reduced magnetocrystalline anisotropy.

## METHODS

**Preparation of Ni(Core)/NiO(Shell) Nanoparticles.** Our procedure for preparing Ni NPs followed a method reported by the Hyeon group with minor modifications.<sup>21</sup> The NP synthesis was performed using a standard vacuum and inert gas (nitrogen) line and commercially available reagents without further purification. For a typical preparation of 24 nm diameter Ni NPs, 0.2 g nickel acetylacetonate (Ni(acac)<sub>2</sub>, 98%, TCI) and 2.0 mL oleylamine (97%, Pfaltz & Bauer) were mixed with 5.0 g trioctylphosphine oxide (TOPO, 99%, Strem) and heated to 80 °C in a three-necked, round-bottomed flask for 2 h under vacuum to remove oxygen before backfilling with nitrogen. By syringe, 0.3 mL trioctylphosphine (TOP, 97%, Strem) was injected into the mixture before rapidly heating the solution to 240 °C (in approximately 10 min) with vigorous stirring. After aging the mixture for 30 min at 240 °C, the mixture was cooled to room temperature, and a flocculation procedure was performed to remove the high-boiling solvent and excess ligands: The NPs were first flocculated by adding excess methanol to the solution and then isolated by centrifugation. After discarding the supernatant, three cycles were performed in which the NPs were redispersed in hexanes, precipitated with methanol and centrifuged. The purified NPs were redispersed in toluene and stored in the glovebox to prevent oxidation. The NP sizes can be controlled by adjusting the amounts of Ni(acac)<sub>2</sub> and oleylamine. For 10 nm diameter NPs, 0.16 g Ni(acac)<sub>2</sub> and 1.6 mL oleylamine was used, and for 8 nm diameter, 0.14 g Ni(acac)<sub>2</sub> and 1.4 mL oleylamine was used.

The as-prepared Ni NPs had thin ~1 nm NiO shells. For growth of thicker ~2 nm NiO shells, the NPs were redispersed in dioctyl ether and heated to 200 °C for 4 h while bubbling air through the NP solution.<sup>11,58</sup> The NPs were removed from the high-boiling solvent through flocculation and centrifugation.

**Transmission Electron Microscopy.** TEM specimens were prepared by placing single drops of dilute NP solutions in hexanes or toluene onto Cu TEM substrates with ultrathin carbon and Formvar support films and allowing the solvent to evaporate. Conventional bright-field imaging and selected-area diffraction were performed using a JEOL 2000FX microscope whose magnification and camera length were calibrated using stained catalase

crystals and aluminum, respectively. HRTEM imaging was carried out on a JEOL 2010F microscope.

**Polymer Dispersions for Magnetic Measurements.** To minimize dipolar interactions between NPs, the NPs were dispersed in monomers that were then polymerized into a matrix of poly(lauryl methacrylate) cross-linked with ethylene glycol dimethacrylate.<sup>11,59</sup> Approximately 10 mg of NPs were dispersed in 1 mL of a solution of 83% lauryl methacrylate, 17% ethylene glycol dimethacrylate, and 0.40% 2,2'-azobisisobutyronitrile (AIBN) by mass. Upon heating the solution to ~110 °C for 5 min, polymerization had occurred. For SQUID measurements, a blank polymer specimen was measured, and the diamagnetic signal was removed from all field-dependent measurements. For determining the magnetization from the measured magnetic moment, inductively coupled plasma-optical emission spectroscopy (ICP-OES) measurements of the concentration of Ni in the polymer were performed by Galbraith Laboratories, Inc.

**Acknowledgment.** This work was supported by the National Science Foundation (ECCS-0707315) and startup funds from North Carolina State University. We thank Rob Schmidt and David Shultz for access to and assistance with the SQUID magnetometer and Tom Rawdanowicz and Trinity Biggerstaff for TEM training.

**Supporting Information Available:** Photographs of polymer sticks with and without NPs, HRTEM and electron diffraction of all NP samples, histograms of NP diameter measurements, and details of the calculation of NiO shell thicknesses. This material is available free of charge via the Internet at <http://pubs.acs.org>.

## REFERENCES AND NOTES

- Hines, M. A.; Guyot-Sionnest, P. Synthesis and Characterization of Strongly Luminescing ZnS-Capped CdSe Nanocrystals. *J. Phys. Chem.* **1996**, *100*, 468–471.
- Dabbousi, B. O.; Rodriguez-Viejo, J.; Mikulec, F. V.; Heine, J. R.; Mattoussi, H.; Ober, R.; Jensen, K. F.; Bawendi, M. G. (CdSe)ZnS Core–Shell Quantum Dots: Synthesis and Characterization of a Size Series of Highly Luminescent Nanocrystallites. *J. Phys. Chem. B* **1997**, *101*, 9463–9475.

3. Xu, Z. C.; Hou, Y. L.; Sun, S. H. Magnetic Core/Shell Fe<sub>3</sub>O<sub>4</sub>/Au and Fe<sub>3</sub>O<sub>4</sub>/Au/Ag Nanoparticles with Tunable Plasmonic Properties. *J. Am. Chem. Soc.* **2007**, *129*, 8698–8699.
4. Melkleejohn, W. H.; Bean, C. P. New Magnetic Anisotropy. *Phys. Rev.* **1957**, *105*, 904–913.
5. Gangopadhyay, S.; Hadjilpanayis, G. C.; Sorensen, C. M.; Klabunde, K. J. In Exchange-Anisotropy in Oxide-Passivated Co Fine Particles, 37th Annual Conference on Magnetism and Magnetic Materials, Houston, TX, Dec 01–04; Amer Inst Physics: Houston, TX, 1992; pp 6964–6966.
6. Verelst, M.; Ely, T. O.; Amlens, C.; Snoeck, E.; Lecante, P.; Mosset, A.; Respaud, M.; Broto, J. M.; Chaudret, B. Synthesis and Characterization of CoO, Co<sub>3</sub>O<sub>4</sub>, and Mixed Co/CoO Nanoparticles. *Chem. Mater.* **1999**, *11*, 2702–2708.
7. Skumryev, V.; Stoyanov, S.; Zhang, Y.; Hadjilpanayis, G.; Givord, D.; Nogués, J. Beating the Superparamagnetic Limit with Exchange Bias. *Nature (London)* **2003**, *423*, 850–853.
8. Spasova, M.; Wledwald, U.; Farle, M.; Radetic, T.; Dahmen, U.; Hilgendorff, M.; Giersig, M. In Temperature Dependence of Exchange Anisotropy in Monodisperse Cobalt Nanoparticles with a Cobalt Oxide Shell, International Conference on Magnetism (ICM 2003), Rome, Italy, Jul 27–Aug 01; 2003; pp 1508–1509.
9. Morel, R.; Brenac, A.; Portemont, C. Exchange Bias and Coercivity in Oxygen-Exposed Cobalt Clusters. *J. Appl. Phys.* **2004**, *95*, 3757–3760.
10. Nogués, J.; Sort, J.; Langlais, V.; Doppli, S.; Dleny, B.; Muñoz, J. S.; Suriñach, S.; Baró, M. D.; Stoyanov, S.; Zhang, Y. Exchange Bias in Ferromagnetic Nanoparticles Embedded in an Antiferromagnetic Matrix. *Int. J. Nanotechnol.* **2005**, *2*, 23–42.
11. Tracy, J. B.; Weiss, D. N.; Dinega, D. P.; Bawendi, M. G. Exchange Biasing and Magnetic Properties of Partially and Fully Oxidized Colloidal Cobalt Nanoparticles. *Phys. Rev. B* **2005**, *72*, 064404.
12. Tracy, J. B.; Bawendi, M. G. Defects in CoO in Oxidized Cobalt Nanoparticles Dominate Exchange Biasing and Exhibit Anomalous Magnetic Properties. *Phys. Rev. B* **2006**, *74*, 184434.
13. Nogués, J.; Sort, J.; Langlais, V.; Skumryev, V.; Suriñach, S.; Muñoz, J. S.; Baró, M. D. Exchange Bias in Nanostructures. *Phys. Rep.* **2005**, *422*, 65–117.
14. Berkowitz, A. E.; Takano, K. Exchange Anisotropy—A Review. *J. Magn. Magn. Mater.* **1999**, *200*, 552–570.
15. Klwl, M. Exchange Bias Theory. *J. Magn. Magn. Mater.* **2001**, *234*, 584–595.
16. Nogués, J.; Schuller, I. K. Exchange Bias. *J. Magn. Magn. Mater.* **1999**, *192*, 203–232.
17. Stamps, R. L. Mechanisms for Exchange Bias. *J. Phys. D: Appl. Phys.* **2000**, *33*, R247–R268.
18. Iglesias, O.; Labarta, A.; Batlle, X. Exchange Bias Phenomenology and Models of Core/Shell Nanoparticles. *J. Nanosci. Nanotechnol.* **2008**, *8*, 2761–2780.
19. Hütten, A.; Sudfeld, D.; Ennen, I.; Reiss, G.; Hachmann, W.; Heinzmann, U.; Wojcyskowski, K.; Jutzl, P.; Saikaly, W.; Thomas, G. New Magnetic Nanoparticles for Biotechnology. *J. Biotechnol.* **2004**, *112*, 47–63.
20. Prinz, G. A. Device Physics—Magnetoelectronics. *Science* **1998**, *282*, 1660–1663.
21. Lee, I. S.; Lee, N.; Park, J.; Kim, B. H.; Yi, Y. W.; Kim, T.; Kim, T. K.; Lee, I. H.; Palk, S. R.; Hyeon, T. Ni/NiO Core/Shell Nanoparticles for Selective Binding and Magnetic Separation of Histidine-Tagged Proteins. *J. Am. Chem. Soc.* **2006**, *128*, 10658–10659.
22. Park, J.; Kang, E.; Son, S. U.; Park, H. M.; Lee, M. K.; Kim, J.; Kim, K. W.; Noh, H. J.; Park, J. H.; Bae, C. J.; Park, J. G.; Hyeon, T. Monodisperse Nanoparticles of Ni and NiO: Synthesis, Characterization, Self-Assembled Superlattices, and Catalytic Applications in the Suzuki Coupling Reaction. *Adv. Mater.* **2005**, *17*, 429–434.
23. Huang, Z. P.; Wang, D. Z.; Wen, J. G.; Sennett, M.; Gibson, H.; Ren, Z. F. Effect of Nickel, Iron and Cobalt on Growth of Aligned Carbon Nanotubes. *Appl. Phys. A* **2002**, *74*, 387–391.
24. Guan, Y. F.; Pearce, R. C.; Melechko, A. V.; Hensley, D. K.; Simpson, M. L.; Rack, P. D. Pulsed Laser Dewetting of Nickel Catalyst for Carbon Nanofiber Growth. *Nanotechnology* **2008**, *19*, 235604.
25. Caruge, J. M.; Halpert, J. E.; Bulović, V.; Bawendi, M. G. NiO as an Inorganic Hole-Transporting Layer in Quantum-Dot Light-Emitting Devices. *Nano Lett.* **2006**, *6*, 2991–2994.
26. Melkleejohn, W. H.; Bean, C. P. New Magnetic Anisotropy. *Phys. Rev.* **1956**, *102*, 1413–1414.
27. Leighton, C.; Nogués, J.; Jönsson-Åkerman, B. J.; Schuller, I. K. Coercivity Enhancement in Exchange Biased Systems Driven by Interfacial Magnetic Frustration. *Phys. Rev. Lett.* **2000**, *84*, 3466–3469.
28. Zheng, R. K.; Wen, G. H.; Fung, K. K.; Zhang, X. X. Giant Exchange Bias and the Vertical Shifts of Hysteresis Loops in  $\gamma$ -Fe<sub>2</sub>O<sub>3</sub>-Coated Fe Nanoparticles. *J. Appl. Phys.* **2004**, *95*, 5244–5246.
29. Zheng, R. K.; Wen, G. H.; Fung, K. K.; Zhang, X. X. Training Effect of Exchange Bias in  $\gamma$ -Fe<sub>2</sub>O<sub>3</sub> Coated Fe Nanoparticles. *Phys. Rev. B* **2004**, *69*, 214431.
30. Ceylan, A.; Baker, C. C.; Hasanain, S. K.; Shah, S. I. Effect of Particle Size on the Magnetic Properties of Core-Shell Structured Nanoparticles. *J. Appl. Phys.* **2006**, *100*, 034301.
31. Martínez-Boubeta, C.; Martínez, B. Critical Radius for Exchange Bias in Naturally Oxidized Fe Nanoparticles. *Phys. Rev. B* **2006**, *74*, 054430.
32. Kavich, D. W.; Dickerson, J. H.; Mahajan, S. V.; Hasan, S. A.; Park, J. H. Exchange Bias of Singly Inverted FeO/Fe<sub>3</sub>O<sub>4</sub> Core-Shell Nanocrystals. *Phys. Rev. B* **2008**, *78*, 174414.
33. Yao, Y. D.; Chen, Y. Y.; Hsu, C. M.; Lin, H. M.; Tung, C. Y.; Tal, M. F.; Wang, D. H.; Wu, K. T.; Suo, C. T. Thermal and Magnetic Studies of Nanocrystalline Ni. *Nanostruct. Mater.* **1995**, *6*, 933–936.
34. Yao, Y. D.; Chen, Y. Y.; Tal, M. F.; Wang, D. H.; Lin, H. M. Magnetic Anisotropy Effects in Nano-Cluster Nickel Particles. *Mater. Sci. Eng. A* **1996**, *217*, 281–285.
35. Sako, S.; Ohshima, K.; Sakai, M.; Bandow, S. Magnetic Property of NiO Ultrafine Particles with a Small Ni Core. *J. Vac. Sci. Technol. B* **1997**, *15*, 1338–1342.
36. Sakiyama, K.; Koga, K.; Seto, T.; Hirasawa, M.; Oril, T. Formation of Size-Selected Ni/NiO Core-Shell Particles by Pulsed Laser Ablation. *J. Phys. Chem. B* **2004**, *108*, 523–529.
37. Roy, A.; Srinivas, V.; Ram, S.; De Toro, J. A.; Rivelro, J. M. Effect of Interstitial Oxygen on the Crystal Structure and Magnetic Properties of Ni Nanoparticles. *J. Appl. Phys.* **2004**, *96*, 6782–6788.
38. Seto, T.; Akinaga, H.; Takano, F.; Koga, K.; Oril, T.; Hirasawa, M. Magnetic Properties of Monodispersed Ni/NiO Core-Shell Nanoparticles. *J. Phys. Chem. B* **2005**, *109*, 13403–13405.
39. Yi, J. B.; Ding, J.; Zhao, Z. L.; Liu, B. H. High Coercivity and Exchange Coupling of Ni/NiO Nanocomposite Film. *J. Appl. Phys.* **2005**, *97*, 10K306.
40. Roy, A.; Srinivas, V.; Ram, S.; De Toro, J. A.; Mizutani, U. Structure and Magnetic Properties of Oxygen-Stabilized Tetragonal Ni Nanoparticles Prepared by Borohydride Reduction Method. *Phys. Rev. B* **2005**, *71*, 184443.
41. Liu, X. S.; Meridor, U.; Zhao, P.; Song, G. B.; Frydman, A.; Gedanken, A. The Synthesis and Magnetic Properties of Monodispersed Single-Domain Nickel Nanospheres and Highly Globular Nanostructures of Ni<sub>core</sub>NiO<sub>shell</sub>. *J. Magn. Magn. Mater.* **2006**, *301*, 13–21.
42. Parada, C.; Morán, E. Microwave-Assisted Synthesis and Magnetic Study of Nanosized Ni/NiO Materials. *Chem. Mater.* **2006**, *18*, 2719–2725.
43. Li, S. D.; Liu, M. M.; Bi, H.; Lü, L. Y.; Zou, W. Q.; Huang, Z. G.; Du, Y. W. The Enhanced Magnetic Properties of Ni Nanocrystallites Induced by the Coupling between Ni/NiO Interfaces. *J. Alloys Compd.* **2006**, *425*, 1–3.

44. Del Bianco, L.; Boscherini, F.; Fiorini, A. L.; Tamsari, M.; Spizzo, F.; Antisari, M. V.; Piscopello, E. Exchange Bias and Structural Disorder in the Nanogranular Ni/NiO System Produced by Ball Milling and Hydrogen Reduction. *Phys. Rev. B* **2008**, *77*, 094408.
45. Sun, X. C.; Dong, X. L. Magnetic Properties and Microstructure of Carbon Encapsulated Ni Nanoparticles and Pure Ni Nanoparticles Coated with NiO Layer. *Mater. Res. Bull.* **2002**, *37*, 991–1004.
46. Salgueiriño-Macelra, V.; Correa-Duarte, M. A.; Bañobre-López, M.; Grzelczak, M.; Farle, M.; Liz-Marzán, L. M.; Rivas, J. Magnetic Properties of Ni/NiO Nanowires Deposited onto CNT/Pt Nanocomposites. *Adv. Funct. Mater.* **2008**, *18*, 616–621.
47. Redl, F. X.; Black, C. T.; Papaefthymiou, G. C.; Sandstrom, R. L.; Yin, M.; Zeng, H.; Murray, C. B.; O'Brien, S. P. Magnetic, Electronic, and Structural Characterization of Nonstoichiometric Iron Oxides at the Nanoscale. *J. Am. Chem. Soc.* **2004**, *126*, 14583–14599.
48. Abarra, E. N.; Takano, K.; Hellman, F.; Berkowitz, A. E. Thermodynamic Measurements of Magnetic Ordering in Antiferromagnetic Superlattices. *Phys. Rev. Lett.* **1996**, *77*, 3451–3454.
49. Alders, D.; Tjeng, L. H.; Voogt, F. C.; Hibma, T.; Sawatzky, G. A.; Chen, C. T.; Vogel, J.; Sacchi, M.; Iacobucci, S. Temperature and Thickness Dependence of Magnetic Moments in NiO Epitaxial Films. *Phys. Rev. B* **1998**, *57*, 11623–11631.
50. Makhlof, S. A.; Parker, F. T.; Spada, F. E.; Berkowitz, A. E. Magnetic Anomalies in NiO Nanoparticles. *J. Appl. Phys.* **1997**, *81*, 5561–5563.
51. Kodama, R. H.; Makhlof, S. A.; Berkowitz, A. E. Finite Size Effects in Antiferromagnetic NiO Nanoparticles. *Phys. Rev. Lett.* **1997**, *79*, 1393–1396.
52. Berkowitz, A. E.; Kodama, R. H.; Makhlof, S. A.; Parker, F. T.; Spada, F. E.; McNiff, E. J.; Foner, S. In Anomalous Properties of Magnetic Nanoparticles, 7th European Magnetic Materials and Applications Conference (EMMA 98), Zaragoza, Spain, Sep 09–12, 1998; pp 591–594.
53. Kodama, R. H.; Berkowitz, A. E. Atomic-Scale Magnetic Modeling of Oxide Nanoparticles. *Phys. Rev. B* **1999**, *59*, 6321–6336.
54. Li, L.; Chen, L. J.; Qihe, R. M.; Li, G. S. Magnetic Crossover of NiO Nanocrystals at Room Temperature. *Appl. Phys. Lett.* **2006**, *89*, 134102.
55. Bahl, C. R. H.; Mørup, S. Varying the Exchange Interaction between NiO Nanoparticles. *Nanotechnology* **2006**, *17*, 2835–2839.
56. Ghosh, M.; Biswas, K.; Sundaresan, A.; Rao, C. N. R. MnO and NiO Nanoparticles: Synthesis and Magnetic Properties. *J. Mater. Chem.* **2006**, *16*, 106–111.
57. Thota, S.; Kumar, J. Sol-Gel Synthesis and Anomalous Magnetic Behaviour of NiO Nanoparticles. *J. Phys. Chem. Solids* **2007**, *68*, 1951–1964.
58. Yin, Y. D.; Rioux, R. M.; Erdonmez, C. K.; Hughes, S.; Somorjai, G. A.; Alivisatos, A. P. Formation of Hollow Nanocrystals through the Nanoscale Kirkendall Effect. *Science* **2004**, *304*, 711–714.
59. Lee, J.; Sundar, V. C.; Helne, J. R.; Bawendi, M. G.; Jensen, K. F. Full Color Emission from II–VI Semiconductor Quantum Dot–Polymer Composites. *Adv. Mater.* **2000**, *12*, 1102–1105.
60. Frankamp, B. L.; Boal, A. K.; Tuominen, M. T.; Rotello, V. M. Direct Control of the Magnetic Interaction between Iron Oxide Nanoparticles through Dendrimer-Mediated Self-Assembly. *J. Am. Chem. Soc.* **2005**, *127*, 9731–9735.
61. Petit, C.; Taleb, A.; Pileni, M. P. Cobalt Nanosized Particles Organized in a 2D Superlattice: Synthesis, Characterization, and Magnetic Properties. *J. Phys. Chem. B* **1999**, *103*, 1805–1810.
62. Poddar, P.; Telem-Shafir, T.; Fried, T.; Markovich, G. Dipolar Interactions in Two- and Three-Dimensional Magnetic Nanoparticle Arrays. *Phys. Rev. B* **2002**, *66*, 060403.
63. Gross, A. F.; Diehl, M. R.; Beverly, K. C.; Richman, E. K.; Tolbert, S. H. Controlling Magnetic Coupling between Cobalt Nanoparticles through Nanoscale Confinement in Hexagonal Mesoporous Silica. *J. Phys. Chem. B* **2003**, *107*, 5475–5482.
64. Bae, C. J.; Angappane, S.; Park, J. G.; Lee, Y.; Lee, J.; An, K.; Hyeon, T. Experimental Studies of Strong Dipolar Interparticle Interaction in Monodisperse Fe<sub>3</sub>O<sub>4</sub> Nanoparticles. *Appl. Phys. Lett.* **2007**, *91*, 102502.
65. Henkes, A. E.; Vasquez, Y.; Schaak, R. E. Converting Metals Into Phosphides: A General Strategy for the Synthesis of Metal Phosphide Nanocrystals. *J. Am. Chem. Soc.* **2007**, *129*, 1896–1897.
66. Winnischofer, H.; Rocha, T. C. R.; Nunes, W. C.; Socolovsky, L. M.; Knobel, M.; Zanchet, D. Chemical Synthesis and Structural Characterization of Highly Disordered Ni Colloidal Nanoparticles. *ACS Nano* **2008**, *2*, 1313–1319.
67. Nunes, W. C.; De Biasi, E.; Meneses, C. T.; Knobel, M.; Winnischofer, H.; Rocha, T. C. R.; Zanchet, D. Magnetic Behavior of Ni Nanoparticles with High Disordered Atomic Structure. *Appl. Phys. Lett.* **2008**, *92*, 183113.
68. Greenwood, N. N.; Eamshaw, A. *Chemistry of the Elements*, 2nd ed.; Butterworth-Heinemann: Boston, MA, 1997; 1151–1152.
69. Rasband, W. S. ImageJ. <http://rsb.info.nih.gov/ij/> (accessed November 1, 2008).
70. O'Handley, R. C. *Modern Magnetic Materials: Principles and Applications*; Wiley-Interscience: New York, 2000; p 99.
71. Peng, S.; Wang, C.; Xie, J.; Sun, S. H. Synthesis and Stabilization of Monodisperse Fe Nanoparticles. *J. Am. Chem. Soc.* **2006**, *128*, 10676–10677.
72. Bean, C. P.; Livingston, J. D. Superparamagnetism. *J. Appl. Phys.* **1959**, *30*, 1205–1295.
73. Bi, H.; Li, S. D.; Zhang, Y. C.; Du, Y. W. Ferromagnetic-Like Behavior of Ultrafine NiO Nanocrystallites. *J. Magn. Magn. Mater.* **2004**, *277*, 363–367.
74. Makhlof, S. A.; Al-Attar, H.; Kodama, R. H. Particle Size and Temperature Dependence of Exchange Bias in NiO Nanoparticles. *Solid State Commun.* **2008**, *145*, 1–4.
75. Dobrynin, A. N.; Temst, K.; Lievens, P.; Margueritat, J.; Gonzalo, J.; Afonso, C. N.; Piscopello, E.; Tendeloo, G. V. Observation of Co/CoO Nanoparticles Below the Critical Size for Exchange Bias. *J. Appl. Phys.* **2007**, *101*, 113913.
76. Gruyters, M. Structural and Magnetic Properties of Transition Metal Oxide/Metal Bilayers Prepared by In Situ Oxidation. *J. Magn. Magn. Mater.* **2002**, *248*, 248–257.
77. Lund, M. S.; Macedo, W. A. A.; Liu, K.; Nogués, J.; Schuller, I. K.; Leighton, C. Effect of Anisotropy on the Critical Antiferromagnet Thickness in Exchange-Biased Bilayers. *Phys. Rev. B* **2002**, *66*, 054422.
78. Yanes, R.; Chubykalo-Fesenko, O.; Kachkachi, H.; Garanin, D. A.; Evans, R.; Chantrell, R. W. Effective Anisotropies and Energy Barriers of Magnetic Nanoparticles with Néel Surface Anisotropy. *Phys. Rev. B* **2007**, *76*, 064416.
79. Stearns, M. 3d, 4d and 5d Elements, Alloys and Compounds. In *Landolt-Börnstein—Group III Condensed Matter*; Wijn, H. P. J., Ed.; Springer-Verlag: New York, 1986; Vol. 19a, pp 41–47.
80. Stoner, E. C.; Wohlfarth, E. P. A Mechanism of Magnetic Hysteresis in Heterogeneous Alloys. *Philos. Trans. R. Soc. London, A* **1948**, *240*, 599–642.

## Supporting Information:

# Synthesis and Structural and Magnetic Characterization of Ni(core)/NiO(shell) Nanoparticles

Aaron C. Johnston-Peck,<sup>†</sup> Junwei Wang,<sup>†</sup> Joseph B. Tracy<sup>†\*</sup>

Department of Materials Science and Engineering, North Carolina State University, Raleigh, North Carolina 27695

Photographs of polymer sticks with and without Ni(core)/NiO(shell) nanoparticles:

empty polymer

containing Ni(core)/NiO(shell) NPs



**Figure S-1.** Photographs of the poly(lauryl methacrylate) cross-linked with ethylene glycol dimethacrylate matrix for SQUID magnetometry measurements: (left) with no nanoparticles added and (right) containing Ni(core)/NiO(shell) nanoparticles.

**High-resolution TEM of Ni(core)/NiO(shell) nanoparticles:**

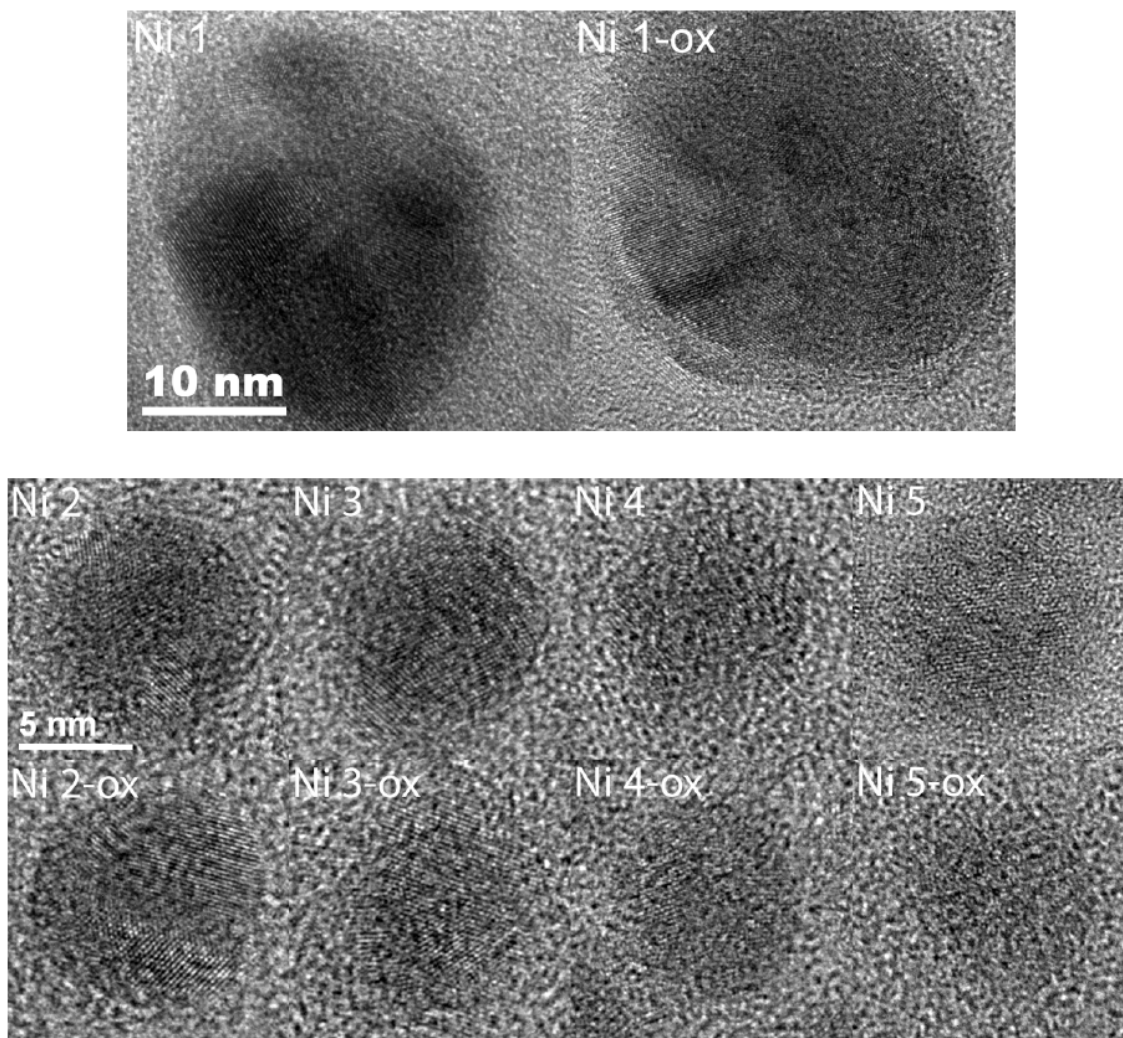


**Figure S-2.** HRTEM images of the native and oxidized Ni nanoparticles.

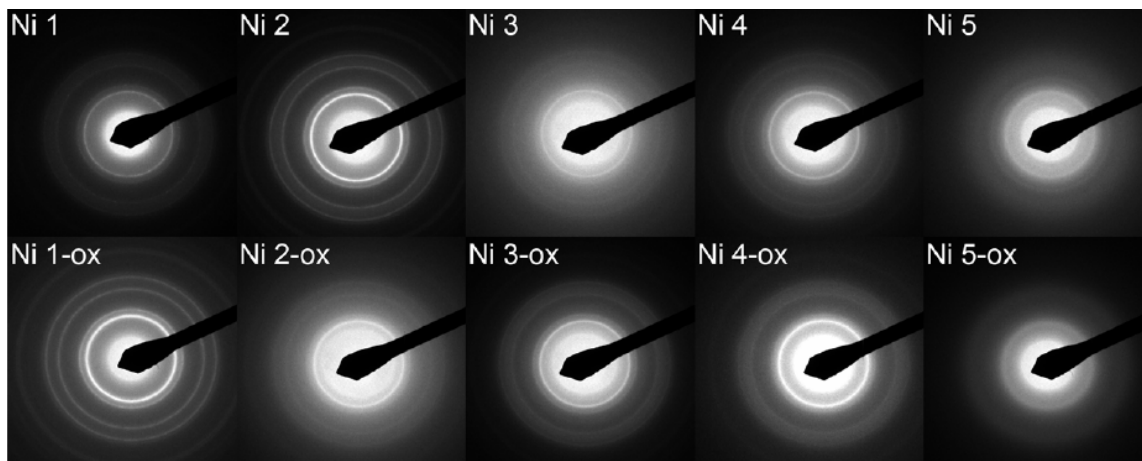


**Figure S-3.** Selected-area electron diffraction of the native and oxidized Ni nanoparticles.

**Histograms of total nanoparticle diameters for the native sample:**

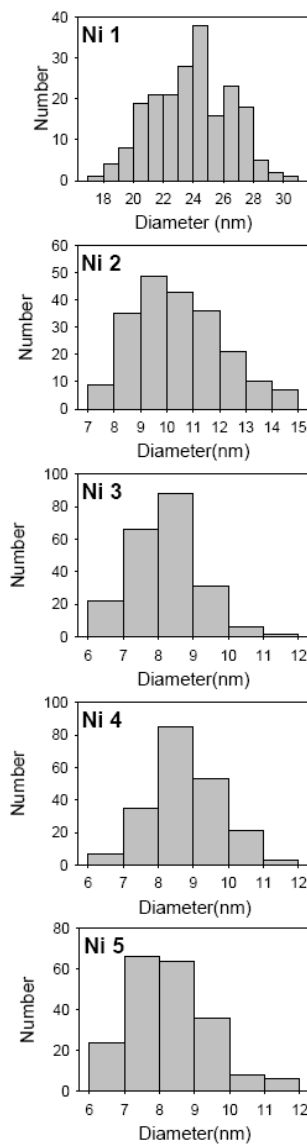


**Figure S-4:** Histograms showing the distribution of total  $2(r_{Ni} + t_{NiO})$  nanoparticle diameters measured by TEM for each sample with native oxidation.

**Calculation of NiO shell thickness:**

We corrected for the linear magnetization of the antiferromagnetic NiO shells by adding a line to the magnetization curve of the Ni(core)/Ni(shell) NPs, thereby eliminating any of the NiO layer from contributing to the saturation magnetization ( $M_{S,measured}$ ), which was computed from the saturation moment in SQUID measurements divided by the mass of Ni content from elemental analysis. Therefore, only unoxidized atoms in the Ni contribute to  $M_{S,measured}$ :

$$\frac{N_{Ni}}{N_{Ni} + N_{NiO}} = \frac{M_{S,measured}}{M_{S,bulkNi}}, \quad (\text{Eq. 1})$$

where  $N_{Ni}$  is the average number of Ni atoms in an unoxidized core,  $N_{NiO}$  is the average number of Ni atoms in the NiO shell, and  $M_{S,BulkNi} = 57.2 \text{ emu/g}$  at  $2.5 \text{ K}$ .<sup>1</sup> Values for  $N_{Ni}$  and  $N_{NiO}$  can be calculated from the bulk densities of Ni and NiO ( $\delta_{Ni} = 8.908 \text{ g/cm}^3$  and  $\delta_{NiO} = 6.67 \text{ g/cm}^3$ ), the molecular weights of Ni ( $MW_{Ni}$ ) and NiO ( $MW_{NiO}$ ), and Avogadro's number ( $N_A$ ):

$$N_{Ni} = \frac{\delta_{Ni} V_{Ni} N_A}{MW_{Ni}} \quad (\text{Eq. 2})$$

$$N_{NiO} = \frac{\delta_{NiO} V_{NiO} N_A}{MW_{NiO}} = \left( \frac{\delta_{NiO}}{\delta_{Ni}} \right) \left( \frac{MW_{Ni}}{MW_{NiO}} \right) \frac{\delta_{Ni} V_{NiO} N_A}{MW_{Ni}} = c \frac{\delta_{Ni} V_{NiO} N_A}{MW_{Ni}}$$

using  $c \equiv \left( \frac{\delta_{NiO}}{\delta_{Ni}} \right) \left( \frac{MW_{Ni}}{MW_{NiO}} \right)$ . (Eq. 3)

Combining Eq. 1, 2, and 3 gives:

$$\frac{V_{Ni}}{V_{Ni} + cV_{NiO}} = \frac{M_{S,measured}}{M_{S,bulkNi}}. \quad (\text{Eq. 4})$$

For spherical NPs with concentric cores and shells, for NPs of *total* radius  $r_{total} = r_{Ni} + t_{NiO}$ .

$$\begin{aligned}
\frac{r_{Ni}^3}{r_{Ni}^3 + c \left[ (r_{Ni} + t_{NiO})^3 - r_{Ni}^3 \right]} &= \frac{1}{1 + c \left[ \left( 1 + \frac{t_{NiO}}{r_{Ni}} \right)^3 - 1 \right]} = \frac{M_{S,measured}}{M_{S,bulkNi}} \\
\Rightarrow 1 + c \left[ \left( 1 + \frac{t_{NiO}}{r_{Ni}} \right)^3 - 1 \right] &= \frac{M_{S,bulkNi}}{M_{S,measured}} \\
\Rightarrow \left( 1 + \frac{t_{NiO}}{r_{total} - t_{NiO}} \right)^3 &= \frac{M_{S,bulkNi}}{cM_{S,measured}} + 1 - \frac{1}{c} \\
\Rightarrow \frac{t_{NiO}}{r_{total} - t_{NiO}} &= \left( \frac{M_{S,bulkNi}}{cM_{S,measured}} + 1 - \frac{1}{c} \right)^{\frac{1}{3}} - 1 \\
\Rightarrow t_{NiO} = r_{total} \left[ \left( \frac{M_{S,bulkNi}}{cM_{S,measured}} + 1 - \frac{1}{c} \right)^{\frac{1}{3}} - 1 \right] &+ t_{NiO} \left[ 1 - \left( \frac{M_{S,bulkNi}}{cM_{S,measured}} + 1 - \frac{1}{c} \right)^{\frac{1}{3}} \right] \\
\Rightarrow t_{NiO} = \frac{r_{total} \left[ \left( \frac{M_{S,bulkNi}}{cM_{S,measured}} + 1 - \frac{1}{c} \right)^{\frac{1}{3}} - 1 \right]}{\left( \frac{M_{S,bulkNi}}{cM_{S,measured}} + 1 - \frac{1}{c} \right)^{\frac{1}{3}}} &= r_{total} \left[ 1 - \left( \frac{M_{S,bulkNi}}{cM_{S,measured}} + 1 - \frac{1}{c} \right)^{\frac{1}{3}} \right]. \quad (\text{Eq. 5})
\end{aligned}$$

Eq. 5 provides the dependence of  $t_{NiO}$  on  $M_{S,measured}$  and  $r_{total}$ , where  $r_{total}$  is half the average total diameter measured by TEM. This relationship has been used to calculate the NiO shell thicknesses reported in Table 1.

#### Reference:

1. O'Handley, R. C., *Modern Magnetic Materials: Principles and Applications*. Wiley-Interscience: New York, 2000; p 99.

## CHAPTER 8

# Formation and Grain Analysis of Spin-Cast Magnetic Nanoparticle Monolayers

The following material was published in *Langmuir* (Vol. 27, No. 8, pp. 5040-5046, 2011) as “Formation and Grain Analysis of Spin-Cast Magnetic Nanoparticle Monolayers” by Aaron C. Johnston-Peck, Junwei Wang, and Joseph B. Tracy. Johnston-Peck’s contribution to the manuscript included synthesizing the FePt NPs, assembling the monolayers, collecting and analyzing the TEM data, writing the MATLAB code used for image analysis, and writing the manuscript.

### 8.1 Motivation

In BPM it is critical that the bits be ordered in a periodic fashion. For commercial applications, the required length scale of assembly would be on the magnitude of  $\text{cm}^2$ . The presence of defects such as grain boundaries, vacancies, and interstitials must be minimized or eliminated as they will cause read and write errors. Self-assembly of NPs is a facile method that allows NPs to spontaneously form ordered assemblies. Significant effort has been invested in long-range self-assembly of NPs, but there has been no report demonstrating greater than  $\text{cm}^2$  areas of assembled NPs with minimal defects. Spin-casting, in comparison with other techniques, has been explored less for the purpose of generating self-assembled

monolayers of NPs. Regardless, it is an attractive technique due to its high-throughput and low cost, which are both key considerations for commercialization.

Irrespective of the self-assembly technique employed, for optimizing the NP assembly, it is important to understand the relationship between the self-assembly experimental parameters and structural properties of the formed NP array. Researchers frequently do not quantitatively characterize the arrays produced but rather use qualitative measures to draw conclusions. Using analytical tools to evaluate the self-assembled structures is critical but it is not without challenges due to the relatively large length scales but small repeat unit associated with NP self-assembly.

This study shows that NP monolayers can be generated by spin-casting. Techniques were also developed to aid in the quantitative characterization of NP monolayers.

## **8.2 Manuscript Reprint**

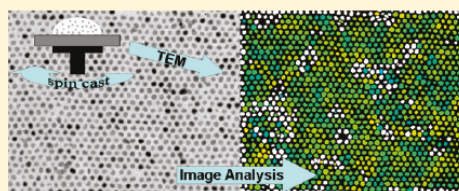
## Formation and Grain Analysis of Spin-Cast Magnetic Nanoparticle Monolayers

Aaron C. Johnston-Peck, Junwei Wang,<sup>†</sup> and Joseph B. Tracy\*

Department of Materials Science and Engineering, North Carolina State University, Raleigh, North Carolina 27695, United States

Supporting Information

**ABSTRACT:** Ligand-stabilized magnetic nanoparticles (NPs) with diameters of 4–7 nm were spin-cast into monolayers on electron-transparent silicon nitride (SiN) substrates. SiN membranes facilitate detailed high-resolution characterization of the spin-cast monolayers by transmission electron microscopy (TEM) and approximate spin-casting onto wafers. Suspending the NPs in hexanes and pretreating the substrate with ultraviolet light and ozone (UVO) gives the best results. Computer-aided analysis of the arrays elucidates their grain structures, including identification of the grain boundaries and defects and measurements of the grain orientations and translational correlation lengths. Narrow NP size distributions result in close-packed arrays with minimal defects and large grains containing thousands of NPs. Edge dislocations, interstitials, vacancies, and overlapping NPs were observed. Deviations from close packing occur as the normalized standard deviation of the sample's size distribution increases above approximately 11%. Polydisperse size distributions and deviations from spherical NP shapes frustrate assembly and prevent ordered packing.



### INTRODUCTION

Large-scale, ordered monolayers of nanoparticles (NPs) are a special kind of thin film with potential for diverse applications. Monolayer NP arrays combine large lateral areas with the novel, size-dependent properties of NPs. Ordering in monolayer arrays is required for applications that would rely on periodicity in the film and also minimizes exposure to the underlying layer, which is particularly important for avoiding shorts in device applications.<sup>1</sup> Several current and potential applications for NP arrays include light-emitting diodes,<sup>2,3</sup> solar cells,<sup>4</sup> ultrahigh-density magnetic recording media,<sup>5</sup> biosensors,<sup>6</sup> catalysis of carbon nanotube growth,<sup>7,8</sup> model catalysts,<sup>9</sup> superhydrophobic surfaces,<sup>10</sup> phononic crystals,<sup>11</sup> and photonic crystals.<sup>12</sup> Fundamental studies of interparticle coupling<sup>13</sup> and conductivity<sup>14</sup> in NP arrays are of considerable interest. Ordered NP arrays have also been reported to have some unusual collective chemical properties, such as enhanced oxidation resistance.<sup>15,16</sup>

Here, we report the self-assembly of NPs with diameters below 10 nm into monolayers by spin-casting onto electron-transparent silicon nitride (SiN) membranes. Ligand-functionalized NPs suspended in organic solvents were spin-cast onto 50 nm-thick SiN membranes (Prochips DuraSiN), followed by imaging by transmission electron microscopy (TEM). Several parameters, including solvent selection, surface treatment, and NP concentration, were varied to optimize self-assembly into monolayers. Detailed structural analysis of the arrays elucidates some general relationships between the experimental parameters and the final product.

Several techniques are available for forming monolayer and multilayer structures. Spin-casting has several attributes that make

it advantageous over other techniques: Spin-casting has higher throughput than dip coating,<sup>17</sup> adsorption onto self-assembled monolayers (SAMs),<sup>18</sup> the Langmuir–Blodgett (LB) method,<sup>19–21</sup> and assembly at the air–liquid interface with no applied lateral pressure.<sup>22–26</sup> Spin-casting can potentially be adapted to accommodate all types of NPs, whereas the LB method uses water and an immiscible phase, thus requiring water-insoluble NPs. Layer-by-layer assembly<sup>27</sup> and spin-assisted assembly<sup>28</sup> are based on electrostatic interactions that require appropriately functionalized NPs. Spin-casting is a highly general, facile technique with good potential for commercialization. Many of the phases obtained through spin-casting are equilibrium or nearly equilibrium phases, but spin-casting also provides opportunities to explore kinetically controlled self-assembly.

There have been several reports of spin-casting of NPs<sup>2,29–35</sup> and of larger, submicrometer-sized particles<sup>36–39</sup> into two-dimensional or three-dimensional structures. Relationships between spin speed,<sup>29,31,36,37</sup> solvent,<sup>2,38</sup> acceleration,<sup>29</sup> time,<sup>31,36</sup> surface treatment,<sup>37</sup> and particle concentration<sup>2,30,32,34,38</sup> and array formation have been reported. Most of the studies reporting the relationship between spin-casting parameters and the coverage and ordering in the assembled product have used larger particles, possibly because of challenges imaging smaller particles. Scanning electron microscopy (SEM), atomic force microscopy (AFM), and small-angle X-ray scattering (SAXS)<sup>33,35</sup> have been used to study these spin-cast structures, while to the best of our

Received: January 2, 2011

Revised: February 24, 2011

Published: March 24, 2011

knowledge, use of TEM has not been reported. Among these techniques, TEM offers the facile advantage of direct, high-resolution imaging (here, “high-resolution” includes phase-contrast imaging as well as amplitude-contrast imaging at resolutions that would be difficult to attain with AFM or SEM) over a large area. Characterization by TEM requires an electron-transparent substrate that is sufficiently robust and flat for spin-casting; the advent of electron-transparent membranes has enabled this study.

Several analytical tools are available for methodically and precisely analyzing the structure of arrays of objects. After converting the TEM image to a binary, black-and-white image, the Delaunay triangulation and its related Voroni tessellation can be calculated and used to identify the presence of point and line defects by determining each NP's number of nearest neighbors.<sup>40</sup> The radial distribution function, which describes the NP density as a function of the distance from a particular NP, can be analyzed to quantify the (short-range) translational and (long-range) orientational order. The grain structure can be determined by assessing the orientation of each NP with respect to its nearest neighbors. These techniques have been applied to many systems, including block copolymers,<sup>40,41</sup> pores,<sup>42,43</sup> microspheres ( $d \geq 100$  nm),<sup>44,45</sup> and, in very few cases, NPs.<sup>46,47</sup>

Here, large spin-cast monolayer arrays of FePt and Ni NPs were prepared, characterized, and analyzed. Analysis of TEM images provides insight into how monolayer formation depends on experimental parameters of the NP stock solution and the spin-casting process. The NP size distribution determines the local ordering, while concentration, surface treatment, and the choice of solvent determine the coverage density. Established analysis techniques were adapted for this first-time application to NP arrays. Grains and grain boundaries were identified by measuring the orientation of each NP with respect to its nearest neighbors. The radial distribution function quantified the length scale of array ordering, while a Delaunay Triangulation mesh identified defects, such as dislocations.

## EXPERIMENTAL SECTION

**Materials.** Oleylamine- and oleic acid-stabilized FePt NPs were synthesized by modifying a method published by Sun et al.<sup>48</sup> Trioctylphosphine-stabilized Ni NPs were synthesized using techniques published by Tracy et al.<sup>49</sup> After purification, the NPs were dispersed in hexanes (98.5%, ACS grade, EMD Chemicals) at concentrations of ~1–2 wt % for spin-casting. SiN membranes (DuraSiN DTF-05523) supplied by Protochips, Inc. were used as substrates for spin-casting and TEM. The 50 nm-thick membrane window has a viewing area of 0.25 mm<sup>2</sup>.

**Substrate Treatment.** As-received substrates were treated in an ultraviolet light with ozone (UVO) cleaner, Jelight model 144-A, operating under ambient conditions for 5 min.

**Spin Cycle.** A Laurel Technologies model WS-650S-6NPP/LITE spin coater was used for spin-casting. The substrate was held in place using a custom-fabricated Teflon chuck. All experiments were conducted under ambient conditions. After depositing approximately 5–10  $\mu$ L of solution on the substrate, spinning was started with an acceleration rate of 500 rpm/s to a maximum speed of 3000 rpm, at which spinning was maintained for 60 s.

**Analysis.** Bright-field imaging was performed on a JEOL 2000FX transmission electron microscope operating at 200 kV. The diameters of 300 NPs were measured for each sample. Image processing was performed using ImageJ and Adobe Photoshop. To obtain the centroids of the NPs for grain and defect analysis, the micrographs were converted into binary images through a series of processing steps using ImageJ and Photoshop. A mask was applied to the fast Fourier transform (FFT) to reduce noise. Application of the FFT mask did not distort the images

(see Supporting Information, Figure S-1 for a comparison) but simplified the conversion process to binary images. In Photoshop, digital filters sharpened the edges of the NPs. The levels of the histogram were then adjusted to convert the image into a black-and-white image. Any NPs that remained conjoined were manually separated using the original image as a guide in an effort to maintain the image integrity. Analysis routines were written (see Supporting Information) for and executed in Matlab R2008a to analyze the image data. The coordinates of the geometric center of each NP were measured and used in the analysis.

The positional data were analyzed using techniques described by Steinhart et al. to determine the radial distribution function (RDF) and the NP orientation.<sup>43</sup> The interparticle distance was calculated using the formula,  $r = ((x_i - x_j)^2 + (y_i - y_j)^2)^{1/2}$ , where  $r$  is the separation length and  $x_i$  and  $y_i$  are the positional coordinates of the  $i$ th NP. The distances were then binned, and the number of counts at each distance was tabulated. The orientation of each NP was calculated using the edge of the image as the reference axis while calculating the slope between nearest-neighbor NPs using the formula,  $\theta = \arctan[(y_i - y_j)/(x_i - x_j)]$ . Calculations of  $\theta$  for every NP were then sorted, and all calculated values were converted into an interval of 0–60° by adding or subtracting multiples of 60°. In the orientation map, the NPs were color coded according to their orientation angle.

The translational correlation length of each array was determined by fitting an exponential decay to the envelope of the RDF (see Supporting Information, Figure S-2).<sup>44,50</sup> Defects were identified by applying a Delaunay Triangulation mesh using the positional data. In the defect map, each NP was color coded according to its coordination number.

## RESULTS AND DISCUSSION

**Nanoparticle Monolayer Synthesis.** The spin-casting process and related parameters were adjusted to maximize the extent of coverage and to optimize the self-assembly of FePt and Ni NPs into monolayers. The SiN substrates were used as-received or after ultraviolet light and ozone (UVO) treatment. Spin-casting of NP solutions in hexanes onto unfunctionalized, UVO-treated substrates gave the best results. UVO treatment increases the surface density of silanol groups while removing residual organics.<sup>51–55</sup> The silanol groups cause stronger van der Waals attractions to the NPs than the untreated substrates, which increases the coverage of NPs but does not appear to hinder monolayer formation. Alkanes with different chain lengths (hexanes, heptane, octane, nonane, and decane) were compared, which showed that (for the same NP concentration in the spin-casting solution) the surface coverage increased as the solvent boiling point decreased, because shorter chain lengths give faster evaporation, thus depositing more NPs on the substrate. The surface coverage was controlled by adjusting the NP concentration in the solution for spin-casting; as the concentration increased, the resulting structures progressed from islands (<1 wt %) to monolayers (1–2 wt %) to multilayers (>2 wt %).

**Grain and Defect Analysis.** Detailed analysis of the NP monolayers provides insight into the self-assembly process. Techniques that quantify and visually accentuate experimental data have been frequently applied to assemblies of diblock copolymers, pores, and micrometer- and submicrometer-sized particles, but there has been limited application to NP arrays.<sup>46,47</sup> Analysis of each NP's geometrical orientation and coordination number (the number of nearest neighbors) allows for identification of defects (interstitials, vacancies, and dislocations) and grain boundaries. The translational correlation length is derived

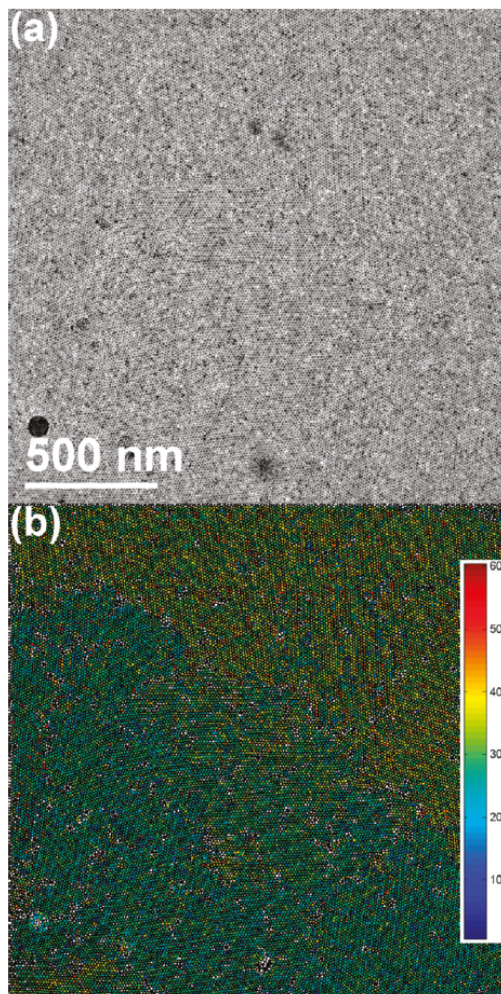


Figure 1. (a) TEM image of Monolayer 1 of Ni nanoparticles (7.0 nm diameter) and its (b) color-coded orientation map.

from the radial distribution function, which gives information about the length scale of ordering.

For analyzing the grain structure of the monolayers, grayscale TEM images were converted to black-and-white images. The location of the centroid of each NP was measured, which was used for further analysis. A Delaunay Triangulation mesh was generated, in which lines were drawn to connect neighboring NPs; vertices correspond to the locations of NPs. Grain and defect analyses were performed to highlight both orientational ordering in the grains and disorder associated with defects. For the grain analysis, the orientation of each NP with respect to its nearest neighbors and reference axes (edges of the image) was calculated, and the NPs were color coded using an interval from  $0^\circ$  to  $60^\circ$ . Grains were defined as contiguous regions over which the NPs

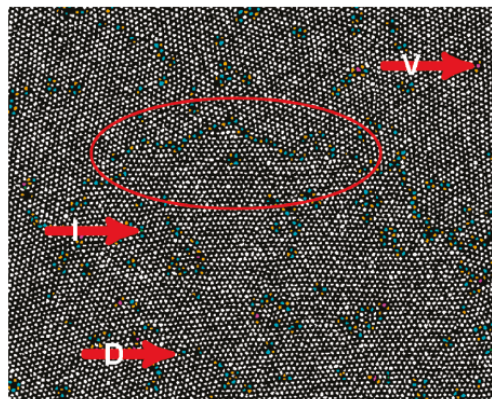


Figure 2. Defect map of part of Monolayer 1, where defects are colored according to their coordination numbers: 4 (green), 5 (orange), 7 (cyan), 8 (magenta). Colored adjacent nanoparticles signify the presence of a defect. Examples of each type of defect have been highlighted, "V" (vacancy), "I" (interstitial), and "D" (dislocation). The oval surrounds a string of dislocations, demarcating a grain boundary.

have the same orientation. NPs that did not have exactly six neighbors within a defined radius were not close packed and were identified as defects, which were colored white to highlight their presence.

For the defect analysis, each NP's coordination number was measured from the Delaunay Triangulation mesh (corresponding to the number of lines intersecting on each vertex). NPs with six nearest neighbors were colored white to indicate that they were close packed and were not defects. NPs deviating from close packing were colored according to their coordination numbers: 4 (green), 5 (orange), 7 (cyan), and 8 (magenta). Two or more adjacent NPs deviating from close packing (6 nearest neighbors) signify the presence of defects. A 5–7 pair indicates a dislocation, while lines (not necessary contiguous) of 5–7 pairs are present at grain boundaries. Groupings of NPs with coordinations of 7–4–7 and 8–5–8 indicate interstitials and vacancies, respectively.<sup>40</sup> Regions of many colored NPs typically do not indicate a specific kind of defect but rather exhibit general disorder and significant deviation from close packing.

A TEM image of a spin-cast monolayer of Ni NPs ( $7.0 \pm 0.8$  nm diameter), Monolayer 1, covering approximately  $3.5 \mu\text{m}^2$  and the corresponding orientation map of the individual NPs is shown in Figure 1. Distinct colored regions in the orientation map highlight different grains of varying size. Most of the grains are truncated by the edges of the image, making it impossible to determine their full sizes. One complete grain near the center of the image is approximately  $0.4 \mu\text{m}^2$  large and contains  $\sim 4000$  NPs. The orientation map shows other truncated grains, both smaller and larger in size. The misorientation angles across grain boundaries range from below  $5^\circ$  to greater than  $15^\circ$ . Grains with similar orientations can be difficult to distinguish from one another in the orientation map; the defect map is particularly useful for distinguishing small angle grain boundaries. Edge dislocations occur periodically at grain boundaries, where the periodicity depends on the misorientation between the two grains, as defined by the relationship,  $D \approx b/\theta$ , where  $b$  is the

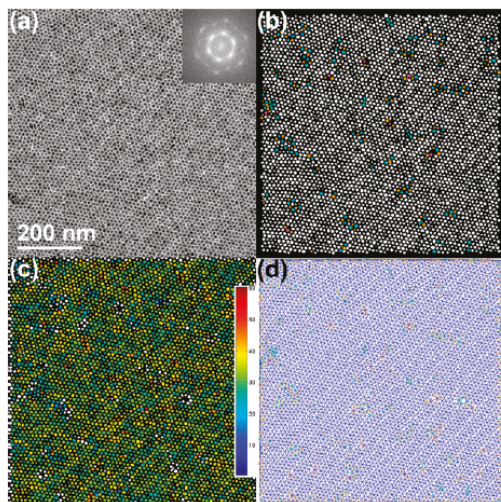


Figure 3. (a) TEM image of Monolayer 2 of FePt nanoparticles (7.2 nm diameter) and its color-coded (b) defect and (c) orientation maps and (d) Delaunay triangulation mesh. Inset (panel a): Fast Fourier transform (FFT) of the image.

burgers vector,  $\theta$  is the tilt angle, and  $D$  is the distance between dislocations.<sup>56</sup>

The defect map shows that dislocations occur at the grain boundaries and within the grains (Figure 2 and Supporting Information, Figure S-3). The defect map also identifies the presence of interstitials and vacancies. The translational correlation length ( $\xi_T$ ) gives a quantitative measure of the translational order. If every grain had a perfect internal structure, then  $\xi_T$  would be approximately equal to the average grain size. The translational correlation length is calculated by fitting an exponential decay proportional to  $\exp(-r/\xi_T)$  to the envelope of the radial distribution function (RDF),  $g(r)$ .<sup>50</sup> The RDF was calculated using positional data from the entire TEM image; thus,  $\xi_T$  is an average value for the entire monolayer. For Monolayer 1,  $\xi_T$  is 250 nm, but this value is smaller than the average grain size, because defects disrupt the translational order,<sup>50,57</sup> as supported by the defect map.

Defects are likely caused by nonuniform NP shapes and sizes,<sup>58</sup> and if the NP self-assembly follows a convective assembly mechanism, their adhesion to the substrate ahead of the growth front can also cause defects.<sup>59</sup> Once the NPs are in contact with the substrate, they likely lack sufficient lateral mobility to recrystallize. As the solution becomes more concentrated, the NPs might form clusters prior to deposition, resulting in polycrystallinity. Alternatively, the polydispersity of the NPs coupled with slow crystallization kinetics might also cause the polycrystalline structure. The spin-casting process occurs rapidly, and it is known that polydisperse samples require longer assembly times to form ordered structures.<sup>60</sup> The rapid kinetics of the spin-casting process may not allow for nonuniform NPs to reorient to continue crystalline grain growth, thus effectively nucleating a new grain. If this is the case, then high-boiling solvents might allow for larger grain sizes by providing longer crystallization times, but higher NP concentrations in the spin-casting solution

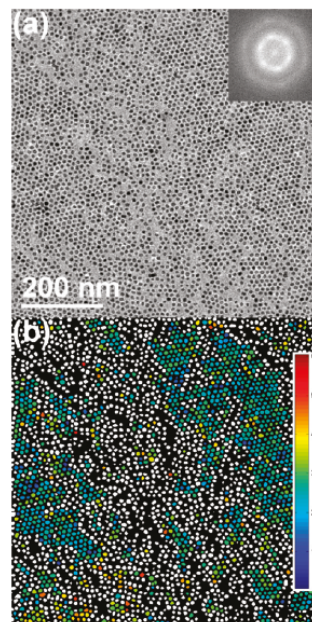
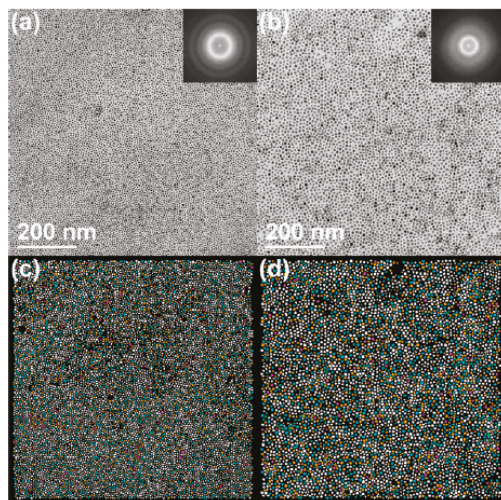


Figure 4. (a) TEM image of Monolayer 3 of FePt nanoparticles (7.2 nm diameter) and its (b) color-coded orientation map. Inset (panel a): Fast Fourier transform (FFT) of the image.

would also be required to compensate for the loss of more material through spinning. We further note that the presence of a small amount of excess ligand would affect self-assembly by altering the solvent wetting behavior and the evaporation process. During assembly of ligand-stabilized NPs at the air–liquid interface, excess ligands have been shown to facilitate self-assembly into monolayers.<sup>23</sup>

A TEM image of an array of FePt NPs ( $7.2 \pm 0.8$  nm diameter), Monolayer 2, covering approximately  $0.5 \mu\text{m}^2$ , comprised of a single grain is shown in Figure 3a, from which the corresponding orientation map (Figure 3c) and defect map (Figure 3b) were obtained. Point defects and edge dislocations are present within the grain. Monolayer 3 (Figure 4a) is a more dilute region of the same spin-cast sample as Monolayer 2. The translational correlation lengths of Monolayers 2 and 3 are 122 and 32 nm, respectively. The TEM image of Monolayer 3 (Figure 4a) shows two bands of close-packed NPs separated by a disordered rift highlighted in the defect map (Supporting Information, Figure S-4). The orientation map for Monolayer 3 (Figure 4b) indicates that the two bands of NPs have the same orientation, which suggests that the bands were once assembled together in a continuous grain and then separated. Prior experimental results<sup>23</sup> and theoretical modeling<sup>61</sup> suggest that suspended NPs assemble into grains in solution and then adhere to the surface as the solvent evaporates. If this mechanism of assembly also applies to spin-casting, then the grain may have separated while still suspended, or part of the grain could have adhered to the surface while the remaining part, still suspended and mobile, was deposited nearby.



**Figure 5.** TEM images of (a) Monolayer 4, a disordered monolayer of spherical FePt nanoparticles (4.2 nm diameter), and (b) Monolayer 5, a disordered monolayer of irregularly-shaped FePt nanoparticles (6.4 nm diameter). Color-coded defect maps for (a) and (b) are shown in (c) and (d), respectively. Insets (panels a,b): Fast Fourier transform (FFT) of the image.

Monolayer 4 (Figure 5a) of smaller FePt NPs ( $4.2 \pm 0.6$  nm diameter) and Monolayer 5 (Figure 5b) of aspherical FePt NPs ( $6.4 \pm 0.7$  nm diameter) both show poor ordering. The translational correlation lengths of 34 and 44 nm, respectively, are markedly lower than those for Monolayers 1–2, even though the experimental parameters were nearly identical. The parameters for the NP solution (ligand composition, solvent, and concentration), substrate treatment, and spin cycle were identical to those for Monolayer 2. Therefore, the differences in the monolayers originate from intrinsic properties of the NPs rather than the deposition parameters. The disorder likely arises from the NP size distribution, because the diameters of the NPs in Monolayer 4 have a relative standard deviation of 13%, but the diameters of NPs in Monolayers 1 and 2 have lower relative standard deviations of 11% and 10%, respectively. Previous studies have reported large-scale assemblies of small NPs through both spin-casting<sup>2</sup> and other techniques, such as drying-mediated self-assembly.<sup>62</sup> Moreover, other experimental studies have shown that assembly is hindered or completely prevented for polydisperse NPs.<sup>2,62</sup> Changing the NP size influences the strength and length scale of the interparticle interactions,<sup>63</sup> but the poor ordering in Monolayer 4 likely arises from the increased size dispersion of the smaller NPs, because similar sizes of monodisperse (standard deviation less than 10%) FePt<sup>64</sup> and PbSe<sup>2</sup> NPs have previously been assembled into ordered structures.

NP shape is another important parameter that determines the extent of (dis)order in the array. The size distribution of the FePt NPs in Monolayer 5 is approximately the same as for Monolayers 1 and 2, but their aspherical shapes prevented crystalline packing. The circularity ( $C$ ) of the two samples of FePt NPs was evaluated using the formula,  $C = 4\pi A/P^2$ , where  $A$  is the cross-sectional

**Table 1.** Summary of Nanoparticle Sizes and Circularities

sample	diameter (nm) <sup>a</sup>	circularity <sup>a</sup>	$\xi_T$ (nm)
Monolayer 1	$7.0 \pm 0.8$		250
Monolayer 2	$7.2 \pm 0.8$	$0.87 \pm 0.03$	122
Monolayer 3	$7.2 \pm 0.8$		32
Monolayer 4	$4.2 \pm 0.6$		34
Monolayer 5	$6.4 \pm 0.7$	$0.80 \pm 0.04$	44

<sup>a</sup>The standard deviation is given as the uncertainty.

area of the NP and  $P$  is the perimeter, giving  $C = 1$  for spherical NPs (Table 1). Values of  $C$  were calculated from measurements of  $A$  and  $P$  for at least 250 NPs. The FePt NPs in the ordered monolayer (Monolayer 2) have an average circularity of 0.87, while the disordered sample (Monolayer 5) has a circularity of 0.80. Therefore, the NPs in Monolayer 5 are less circular, and there is a greater dispersion of shapes than in Monolayer 2, but perfectly spherical NPs are not required for assembly into close-packed arrays. Measurements of  $C$  do not, however, fully capture the shapes of the NPs, because measurements are made of two-dimensional projections, and a different projection of the same NP could give a different circularity. Furthermore, different shapes can have the same circularity. It is also known that nanorods can pack into highly ordered, nonclose-packed arrays through drying-mediated assembly if the distribution of shapes is sufficiently narrow.<sup>65,66</sup> Drying-mediated assembly is, however, a slower process than spin-casting; the additional time allows for the assembly of nonspherical shapes into ordered structures, whereas the short assembly time of the spin-casting process might lead to disordered assemblies. Coe-Sullivan et al. showed that spin-cast arrays of rod-shaped quantum dots assembled into disordered rather than close-packed structures, but this disorder likely arose from polydisperse shapes.<sup>2</sup> In addition to the reduced circularity, the NPs in Monolayer 5 have irregular shapes (Supporting Information, Figure S-5), whereas the NPs in Monolayer 2 were approximately circular or slightly oblong (Supporting Information, Figure S-6). Assembly of the ligands on the NP surfaces, which depends on the surface curvature and faceting, among other variables, is also expected to affect the interparticle interactions and is not simple to predict. Nevertheless, a greater dispersion of NP shapes has more disordered and hence weaker interparticle interactions that would provide less enthalpic driving force for assembly. Therefore, the disordered packing likely arises from the variety of morphologies present in the addition to the lack of sphericity; incommensurate structures have been documented to cause hexatic assembly.<sup>44,67</sup>

## CONCLUSIONS

Spin-casting is a facile technique for synthesizing NP monolayers, and SiN membranes facilitate their characterization by TEM. Image analysis techniques enable analysis of the grain structures and defects in the monolayers. Short-range ordering in the monolayers is determined by the NP size and shape distributions and by the spin-casting conditions.

Deposition of functional NP monolayers over large lateral dimensions is highly desirable, because NP monolayers could serve as a new kind of thin film in electronic, magnetic, and photonic materials and devices. Comparable or larger close-packed monolayers of ligand-stabilized NPs have been achieved through the LB method<sup>19–21</sup> and the assembly of NPs at the

air–liquid interface under zero lateral pressure,<sup>22–26</sup> but spin-casting remains highly desirable due to its simplicity and greater potential for commercialization. Recently, wafer-scale assembly of ~300 nm particles was demonstrated through spin-casting,<sup>39</sup> but assembly of smaller, <10 nm NPs remains challenging, because the interparticle interactions are much weaker for smaller sizes. By comparison, the largest areal coverage that we have obtained through spin-casting is on the order of tens of  $\mu\text{m}^2$  (Supporting Information, Figure S-7). Achieving spin-cast monolayers over larger areas will likely require specially functionalized NPs that will optimize the interparticle and NP–substrate interactions to drive crystalline monolayer formation while avoiding multilayer formation until the first monolayer is complete.

## ■ ASSOCIATED CONTENT

**S Supporting Information.** Synthetic procedures for Ni and FePt nanoparticles, additional TEM images, grain analysis, and Matlab code for performing grain analysis. This material is available free of charge via the Internet at <http://pubs.acs.org>.

## ■ AUTHOR INFORMATION

### Corresponding Author

\*E-mail: [jbtracy@ncsu.edu](mailto:jbtracy@ncsu.edu).

### Present Addresses

<sup>†</sup>Department of Materials Science and Engineering, Rensselaer Polytechnic Institute, Troy, New York 12180, United States.

## ■ ACKNOWLEDGMENT

This research was supported by the National Science Foundation (ECCS-0707315) and startup funds from North Carolina State University. A.C.J.-P. acknowledges support from a GAANN fellowship. We thank Protochips, Inc. for providing the SiN substrates and Dr. Jonathan Steckel, Prof. Sang-Kee Eah, Prof. Jan Genzer, and Philip Marquis for helpful discussions.

## ■ REFERENCES

- (1) Anikeeva, P. O.; Halpert, J. E.; Bawendi, M. G.; Bulović, V. *Nano Lett.* **2007**, *7*, 2196–2200.
- (2) Coe-Sullivan, S.; Steckel, J. S.; Woo, W. K.; Bawendi, M. G.; Bulović, V. *Adv. Funct. Mater.* **2005**, *15*, 1117–1124.
- (3) Caruge, J. M.; Halpert, J. E.; Wood, V.; Bulović, V.; Bawendi, M. G. *Nat. Photon.* **2008**, *2*, 247–250.
- (4) Lin, S. C.; Lee, Y. L.; Chang, C. H.; Shen, Y. J.; Yang, Y. M. *Appl. Phys. Lett.* **2007**, *90*, 143517.
- (5) Sun, S. H.; Murray, C. B.; Weller, D.; Folks, L.; Moser, A. *Science* **2000**, *287*, 1989–1992.
- (6) Li, C. Z.; Liu, Y. L.; Luong, J. H. T. *Anal. Chem.* **2005**, *77*, 478–485.
- (7) Choi, G. S.; Cho, Y. S.; Son, K. H.; Kim, D. J. *Microelectron. Eng.* **2003**, *66*, 77–82.
- (8) Paillet, M.; Jourdain, V.; Poncharal, P.; Sauvajol, J. L.; Zahab, A.; Meyer, J. C.; Roth, S.; Cordente, N.; Amiens, C.; Chaudret, B. *J. Phys. Chem. B* **2004**, *108*, 17112–17118.
- (9) Grunwaldt, J. D.; Kiener, C.; Wögerbauer, C.; Baiker, A. *J. Catal.* **1999**, *181*, 223–232.
- (10) Ling, X. Y.; Phang, I. Y.; Vancso, G. J.; Huskens, J.; Reinhoudt, D. N. *Langmuir* **2009**, *25*, 3260–3263.
- (11) Robertson, W. M.; Rudy, J. F. *J. Acoust. Soc. Am.* **1998**, *104*, 694–699.

- (12) Miyazaki, H. T.; Miyazaki, H.; Ohtaka, K.; Sato, T. *J. Appl. Phys.* **2000**, *87*, 7152–7158.
- (13) Polavarapu, L.; Xu, Q. H. *Nanotechnology* **2009**, *20*, 185606.
- (14) Greshnykh, D.; Frömsdorf, A.; Weller, H.; Klinke, C. *Nano Lett.* **2009**, *9*, 473–478.
- (15) Klecha, E.; Ingert, D.; Walls, M.; Pileni, M. P. *Langmuir* **2009**, *25*, 2824.
- (16) Lisiecki, I.; Turner, S.; Bals, S.; Pileni, M. P.; Van Tendeloo, G. *Chem. Mater.* **2009**, *21*, 2335–2338.
- (17) Yoon, T. S.; Oh, J. H.; Park, S. H.; Kim, V.; Jung, B. G.; Min, S. H.; Park, J.; Hyeon, T.; Kim, K. B. *Adv. Funct. Mater.* **2004**, *14*, 1062–1068.
- (18) Raj, C. R.; Okajima, T.; Ohsaka, T. *J. Electroanal. Chem.* **2003**, *543*, 127–133.
- (19) Dabbousi, B. O.; Murray, C. B.; Rubner, M. F.; Bawendi, M. G. *Chem. Mater.* **1994**, *6*, 216–219.
- (20) Chen, S. W. *Langmuir* **2001**, *17*, 2878–2884.
- (21) Lee, D. K.; Kim, Y. H.; Kim, C. W.; Cha, H. G.; Kang, Y. S. *J. Phys. Chem. B* **2007**, *111*, 9288–9293.
- (22) Santhanam, V.; Liu, J.; Agarwal, R.; Andres, R. P. *Langmuir* **2003**, *19*, 7881–7887.
- (23) Bigioni, T. P.; Lin, X. M.; Nguyen, T. T.; Corwin, E. I.; Witten, T. A.; Jaeger, H. M. *Nat. Mater.* **2006**, *5*, 265–270.
- (24) Mueggenburg, K. E.; Lin, X. M.; Goldsmith, R. H.; Jaeger, H. M. *Nat. Mater.* **2007**, *6*, 656–660.
- (25) Jiang, Z.; Lin, X. M.; Sprung, M.; Narayanan, S.; Wang, J. *Nano Lett.* **2010**, *10*, 799–803.
- (26) Martin, M. N.; Basham, J. L.; Chando, P.; Eah, S. K. *Langmuir* **2010**, *26*, 7410–7417.
- (27) Decher, G.; Hong, J. D.; Schmitt, J. *Thin Solid Films* **1992**, *831*–835.
- (28) Jiang, C. Y.; Markutsya, S.; Tsukruk, V. V. *Langmuir* **2004**, *20*, 882–890.
- (29) Rehg, T. J.; Higgins, B. G. *AIChE J.* **1992**, *38*, 489–501.
- (30) Hong, Y. K.; Kim, H.; Lee, G.; Kim, W.; Park, J. I.; Cheon, J.; Koo, J. Y. *Appl. Phys. Lett.* **2002**, *80*, 844–846.
- (31) Liu, F. K.; Chang, Y. C.; Ko, F. H.; Chu, T. C.; Dai, B. T. *Microelectron. Eng.* **2003**, *67*–68, 702–709.
- (32) Kim, S. G.; Hagura, N.; Iskandar, F.; Yabuki, A.; Okuyama, K. *Thin Solid Films* **2008**, *516*, 8721–8725.
- (33) Hanrath, T.; Choi, J. J.; Smilgies, D. M. *ACS Nano* **2009**, *3*, 2975–2988.
- (34) Wang, H. B.; Wang, H.; Yang, F. J.; Zhang, J.; Li, Q.; Zhou, M. J.; Jiang, Y. *Surf. Coat. Technol.* **2010**, *204*, 1509–1513.
- (35) Heitsch, A. T.; Patel, R. N.; Goodfellow, B. W.; Smilgies, D. M.; Korgel, B. A. *J. Phys. Chem. C* **2010**, *114*, 14427–14432.
- (36) Jiang, P.; McFarland, M. J. *J. Am. Chem. Soc.* **2004**, *126*, 13778–13786.
- (37) Ogi, T.; Modesto-Lopez, L. B.; Iskandar, F.; Okuyama, K. *Colloids Surf., A* **2007**, *297*, 71–78.
- (38) Wee, L. H.; Tosheva, L.; Vasilev, C.; Doyle, A. M. *Microporous Mesoporous Mater.* **2007**, *103*, 296–301.
- (39) Liu, X. F.; Sun, C. H.; Linn, N. C.; Jiang, B.; Jiang, P. *J. Phys. Chem. C* **2009**, *113*, 14804–14811.
- (40) Segalman, R. A.; Hexemer, A.; Hayward, R. C.; Kramer, E. J. *Macromolecules* **2003**, *36*, 3272–3288.
- (41) Harrison, C.; Angelescu, D. E.; Trawick, M.; Cheng, Z. D.; Huse, D. A.; Chaikin, P. M.; Vega, D. A.; Sebastian, J. M.; Register, R. A.; Adamson, D. H. *Europhys. Lett.* **2004**, *67*, 800–806.
- (42) Mátéfi-Tempfli, S.; Mátéfi-Tempfli, M.; Piraux, L. *Thin Solid Films* **2008**, *516*, 3735–3740.
- (43) Hillebrand, R.; Müller, F.; Schwirn, K.; Lee, W.; Steinhart, M. *ACS Nano* **2008**, *2*, 913–920.
- (44) Dullens, R. P. A.; Mourad, M. C. D.; Aarts, D.; Hoogenboom, J. P.; Kegels, W. K. *Phys. Rev. Lett.* **2006**, *96*, 028304.
- (45) Knapek, C. A.; Samsonov, D.; Zhdanov, S.; Konopka, U.; Morfill, G. E. *Phys. Rev. Lett.* **2007**, *98*, 015004.
- (46) Kim, B.; Carignano, M. A.; Tripp, S. L.; Wei, A. *Langmuir* **2004**, *20*, 9360–9365.

- (47) Yun, S.-H.; Yoo, S. L.; Jung, J. C.; Zin, W.-C.; Sohn, B.-H. *Chem. Mater.* **2006**, *18*, 5646–5648.
- (48) Chen, M.; Liu, J. P.; Sun, S. H. *J. Am. Chem. Soc.* **2004**, *126*, 8394–8395.
- (49) Johnston-Peck, A. C.; Wang, J.; Tracy, J. B. *ACS Nano* **2009**, *3*, 1077–1084.
- (50) Nelson, D. R. *Defects and Geometry in Condensed Matter Physics*; Cambridge University Press: Cambridge, 2002.
- (51) Vig, J. R. *J. Vac. Sci. Technol., A* **1985**, *3*, 1027–1034.
- (52) Kasi, S. R.; Liehr, M. *Appl. Phys. Lett.* **1990**, *57*, 2095–2097.
- (53) Ogbuji, L. U. T.; Jayne, D. T. *J. Electrochem. Soc.* **1993**, *140*, 759–766.
- (54) Zazzera, L.; Evans, J. F. *J. Vac. Sci. Technol., A* **1993**, *11*, 934–939.
- (55) Ito, T.; Namba, M.; Bühlmann, P.; Umezawa, Y. *Langmuir* **1997**, *13*, 4323–4332.
- (56) Hirth, J. P.; Lothe, J. *Theory of Dislocations*, 2nd ed.; John Wiley & Sons: New York, 1982.
- (57) Strandburg, K. J. *Bond-Orientational Order in Condensed Matter Systems*; Springer-Verlag: New York, 1992.
- (58) Dimitrov, A. S.; Nagayama, K. *Langmuir* **1996**, *12*, 1303–1311.
- (59) Denkov, N.; Velez, O.; Kralchevski, P.; Ivanov, I.; Yoshimura, H.; Nagayama, K. *Langmuir* **1992**, *8*, 3183–3190.
- (60) Rakers, S.; Chi, L. F.; Fuchs, H. *Langmuir* **1997**, *13*, 7121–7124.
- (61) Zhao, Y.; Marshall, J. S. *Phys. Fluids* **2008**, *20*, 043302.
- (62) Murray, C. B.; Kagan, C. R.; Bawendi, M. G. *Annu. Rev. Mater. Res.* **2000**, *30*, 545–610.
- (63) Bishop, K. J. M.; Wilmer, C. E.; Soh, S.; Grzybowski, B. A. *Small* **2009**, *5*, 1600–1630.
- (64) Shevchenko, E.; Talapin, D.; Kornowski, A.; Wieckhorst, F.; Kotzler, J.; Haase, M.; Rogach, A.; Weller, H. *Adv. Mater.* **2002**, *14*, 287–290.
- (65) Jana, N. R. *Angew. Chem., Int. Ed.* **2004**, *43*, 1536–1540.
- (66) Sau, T. K.; Murphy, C. J. *Langmuir* **2005**, *21*, 2923–2929.
- (67) Dullens, R. P. A.; de Villeneuve, V. W. A.; Mourad, M. C. D.; Petukhov, A. V.; Kegel, W. K. *Eur. Phys. J.: Appl. Phys.* **2008**, *44*, 21–28.

## Supporting Information

### **Formation and Grain Analysis of Spin-Cast Magnetic Nanoparticle Monolayers**

Aaron C. Johnston-Peck, Junwei Wang,<sup>†</sup> and Joseph B. Tracy\*

*Department of Materials Science and Engineering, North Carolina State University, Raleigh, North Carolina 27695*

*<sup>†</sup>Present Address: Department of Materials Science and Engineering, Rensselaer Polytechnic Institute, Troy, New York 12180*

#### **Synthetic Procedure for Ni Nanoparticles**

Ni NPs with diameters of 7 nm were synthesized as follows: 130 mg (0.44 mmol) nickel(II) acetylacetonate (98 %, TCI), 1.30 mL (3.83 mmol) oleylamine (97%, Pfaltz & Bauer), and 5.0 g trioctylphosphine oxide (TOPO, 90%, Sigma-Aldrich) were combined in a three-necked, round-bottomed 100 mL flask with a magnetic stir bar. After degassing the solution under vacuum for 90 min at 80 °C and backfilling with nitrogen, the mixture was heated to 240 °C for 30 min. During the heating ramp, 0.30 mL (0.65 mmol) trioctylphosphine (TOP, 97%, Strem) was added by syringe at 100 °C. After completing the reaction and cooling the flask to room temperature, ~5 mL toluene was added to prevent crystallization of the TOPO. Methanol was then added to flocculate the NPs, followed by centrifugation at 4000 rpm to separate the NPs from the TOPO and reaction side products. After decanting the supernatant, the NPs were redispersed in hexanes. For further purification, two additional cycles of flocculation were performed by adding methanol, centrifuging to isolate the NPs, and redispersing in hexanes. The purified NPs were stored in hexanes in a glass vial.

#### **Synthetic Procedure for FePt Nanoparticles**

FePt NPs with diameters of 4 nm were synthesized as follows: 101 mg (0.25 mmol) platinum(II) acetylacetonate (97 %, Sigma Aldrich) and 10.0 mL benzyl ether (99%, Acros) were combined in a three-necked, round-bottomed 100 mL flask with a magnetic stir bar. After degassing the solution under vacuum for 75 min at room temperature and backfilling with nitrogen, the mixture was heated to 100 °C. Immediately upon reaching 100 °C, 0.34 mL (1.00 mmol) oleylamine (97%, Pfaltz & Bauer), 0.32 mL (1.00 mmol) oleic acid (99%, Alfa Aesar), and 81 µL (0.60 mmol) iron pentacarbonyl (99.5%, Alfa Aesar) were added by syringe. The temperature was held constant at 100 °C for 10 min and was then increased to 290 °C for 60 min. After completing the reaction and cooling the flask to room temperature, methanol was added to flocculate the NPs, followed by centrifugation at 4000 rpm to separate the NPs from the benzyl ether and reaction side products. After decanting the supernatant, the NPs were redispersed in hexanes. For further purification, two additional cycles of flocculation were performed by adding ethanol, centrifuging to isolate the NPs, and redispersing in hexanes. A drop (~0.05 mL) of oleic acid was added to the purified NPs in hexanes, and this mixture was stored in a glass vial. For synthesizing other sizes of FePt NPs, the concentration of oleic acid and oleylamine was varied.

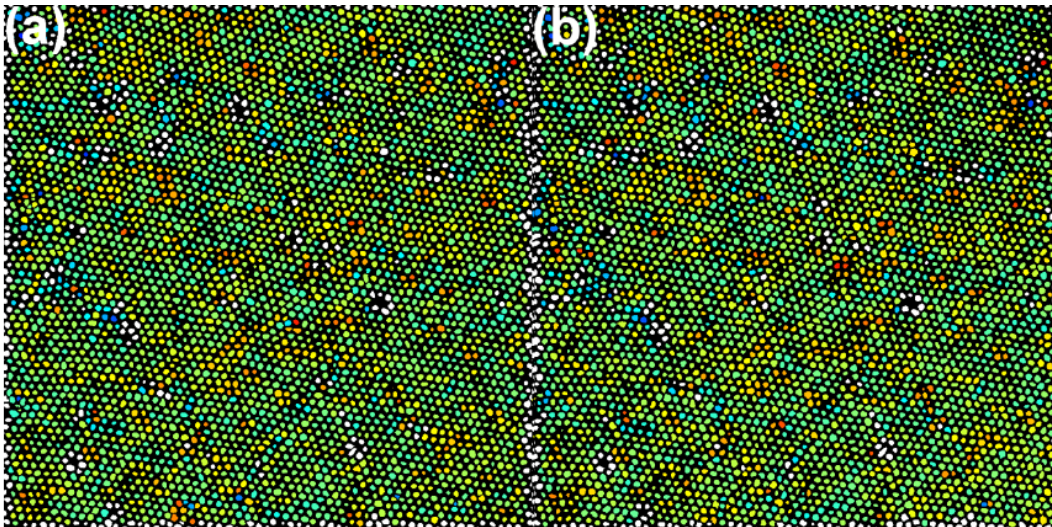


**Figure S-1.** Comparison of orientation maps for Monolayer 2 generated from Figure 3a (a) using a fast Fourier transform (FFT) mask in the process of converting the raw image to a binary image, and (b) without using the FFT mask in the conversion process.

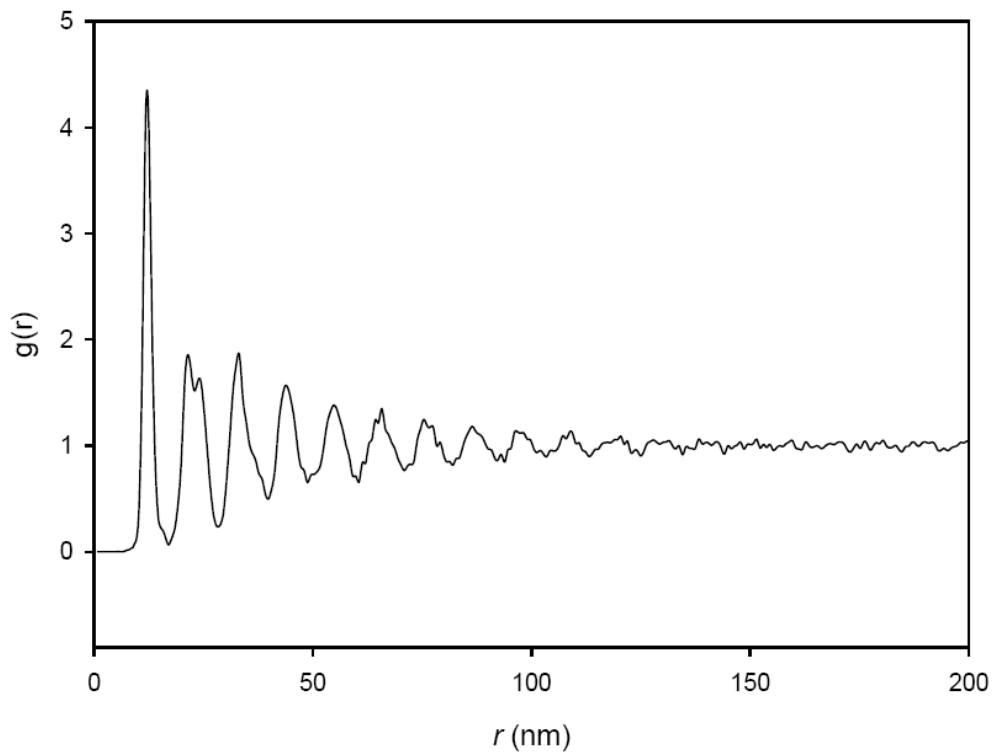


**Figure S-2.** Radial distribution function of Monolayer 2 (calculated from Figure 3a).

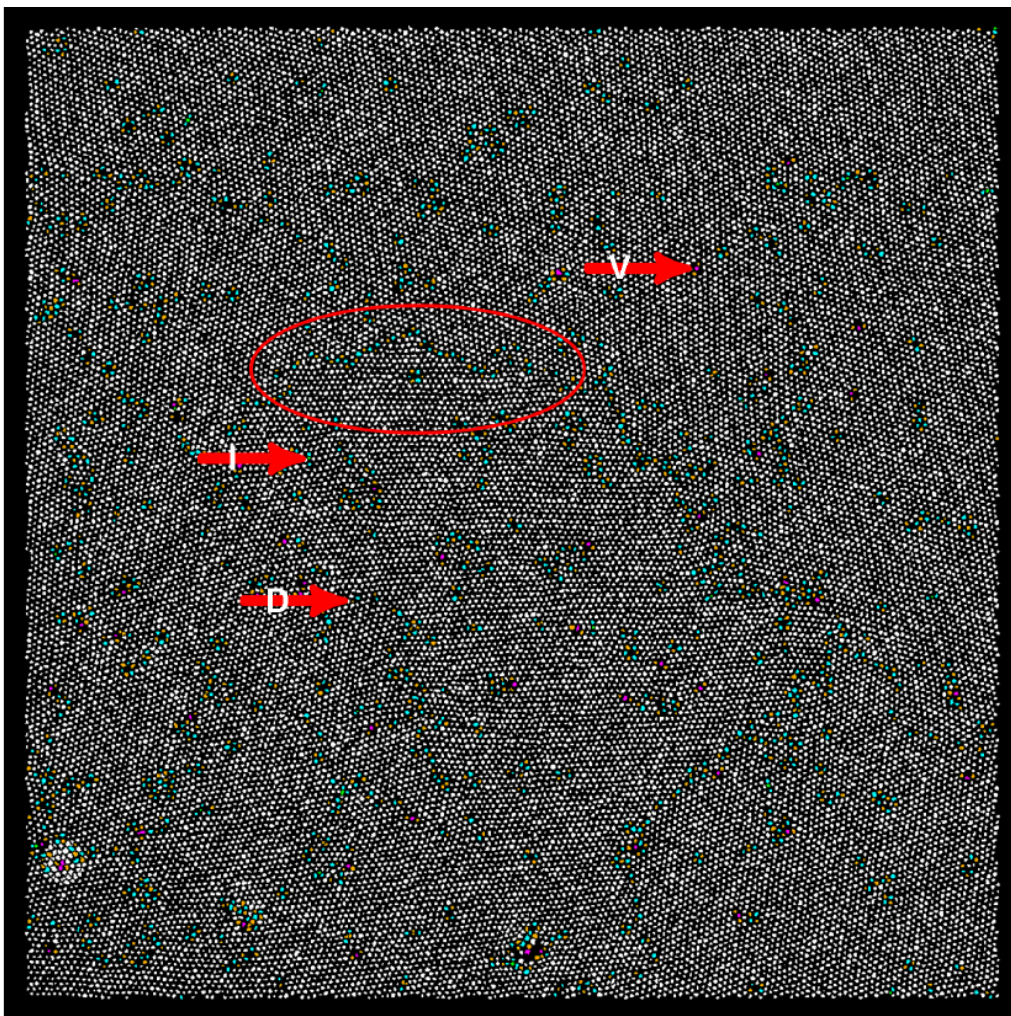


**Figure S-3.** Whole defect map of Monolayer 1, where defects are colored according to their coordination numbers: 4 (green), 5 (orange), 7 (cyan), 8 (magenta). Colored adjacent nanoparticles signify the presence of a defect. Examples of each type of defect have been highlighted, “V” (vacancy), “I” (interstitial), and “D” (dislocation). The oval surrounds a string of dislocations, demarcating a grain boundary.

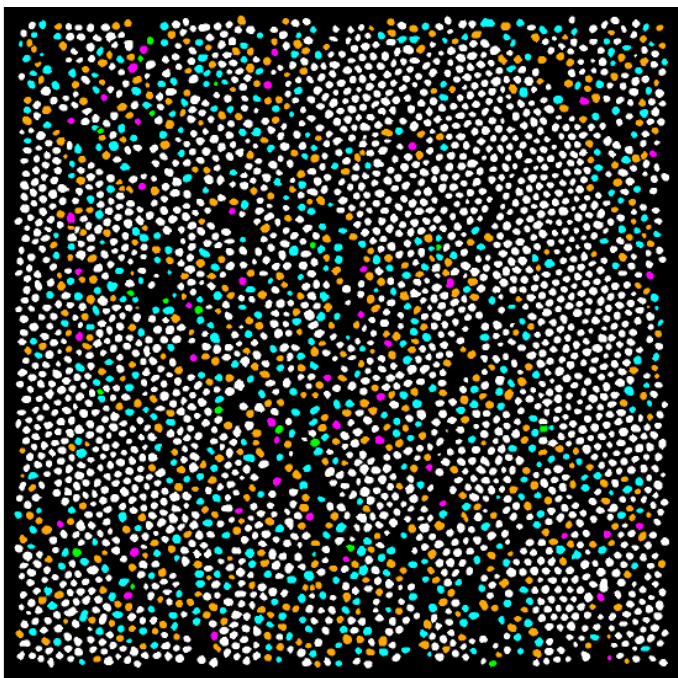


**Figure S-4.** Defect map of Monolayer 3 of FePt nanoparticles (7.2 nm diameter) corresponding to the TEM image shown in Figure 4a of the main text.

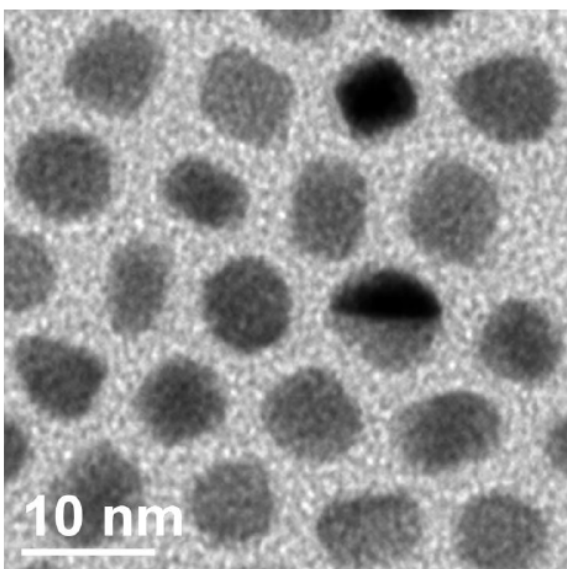


**Figure S-5.** TEM image of FePt nanoparticles (6.4 nm diameter) used to synthesize Monolayer 5 (Figure 5b).

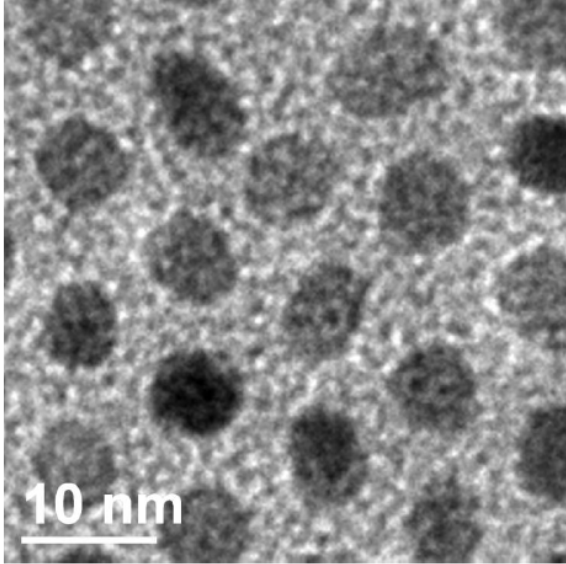


**Figure S-6.** TEM image of FePt nanoparticles (7.2 nm diameter) used to synthesize the close-packed Monolayers 2-3 (Figures 3-4).

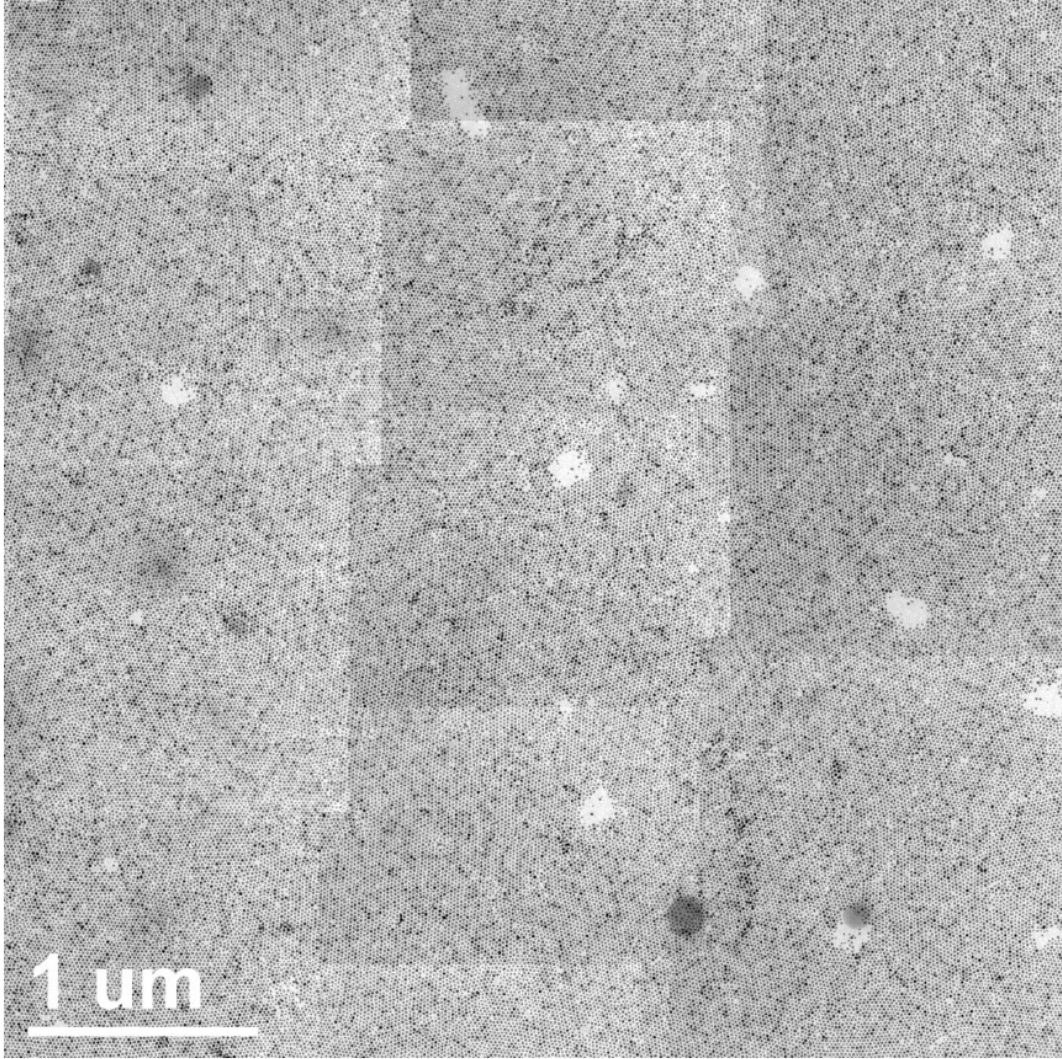


**Figure S-7.** TEM image of a monolayer of Ni nanoparticles (7.0 nm diameter) covering approximately  $21 \mu\text{m}^2$ .

**Code 1.** The following Matlab code computes the pair distribution function for a selected image and writes the output to Microsoft Excel file.

```

clear;
%Computes the PDF
%Part 1: Determining coordinates of particle centroids
%Binary (bitmap) image file (use white background, black particles)
original = imread('Filename.tif');
comporiginal = imcomplement(original);
L = bwlabel(comporiginal);
stats = regionprops(L , 'Centroid');
centroids = cat(1 , stats.Centroid);
xcoords(: , 1) = centroids (: , 1);
ycoords(: , 1) = centroids (: , 2);

%defines t as the size of the inputted list of coordinates
t = size(xcoords,1);

%Part 2: Calculating PDF
%Maximum radius calculated
%calculates the distance between every point
distances = zeros(t*t,1);
counter = 1;
for j=1:t
    for i=j+1:t
        distances(counter,1) = (((xcoords(i,1)-xcoords(j,1))^2+...
            (ycoords(i,1)-ycoords(j,1))^2)^.5);
        counter = counter + 1;
    end
end

%rounds distance calculations to nearest integer for plotting purposes
rdist = round(distances);

%creates a data set with a set of distances that occur in the rounded
%dataset
cordist=unique(rdist(:));

%creates a histogram of the how many times a specific value in the rounded
%dataset occurs
count=hist(rdist(:),cordist)';

%outputting data sets to excel files where they can then be plotted
save 'cordist.xls' cordist -ascii
save 'count.xls' count -ascii

```

**Code 2.** The following Matlab code computes the radial distribution function from a selected image and writes the output to a Microsoft Excel file.

```

%Computes Radial Distribution Function from an image

clear;
%Part 1: Determining coordinates of particle centroids

```

```

%Binary (bitmap) image file (use white background, black particles)
original = imread('Filename.tif');
comporiginal = imcomplement(original);
L = bwlabel(comporiginal);
stats = regionprops(L, 'Centroid');
centroids = cat(1, stats.Centroid);
totalpoints = size(centroids, 1);
xcoords(:, 1) = centroids(:, 1);
ycoords(:, 1) = centroids(:, 2);

%Part 2: Calculating PDF
%Maximum radius calculated
maxr = 300;
%Length of image side (pixels)
imagesize = 1024;
%Radius interval size
width = 1;
g=zeros(maxr,1);
r=0;
count=0;

for i=1:totalpoints
    for j=i + 1:totalpoints
        if xcoords(i) > maxr && xcoords(i) < imagesize - maxr && ...
            ycoords(i) > maxr && ycoords(i) < imagesize - maxr
            r = sqrt((xcoords(i)-xcoords(j))^2+(ycoords(i)-ycoords(j))^2);
            count = round(r / width);
            if count < maxr
                g(count) = g(count) + 1;
            end
        end
    end
end

%Part 3:Normalization
radius1=zeros(maxr,1);
radius2=zeros(maxr,1);
area=zeros(maxr,1);

for i = 1:maxr
    radius1(i,1) = (i-1) * width;
    radius2(i,1) = radius1(i,1) + width;
    area(i,1) = pi * ((radius2(i,1)^2)-(radius1(i,1)^2));
end

totalarea = sum(area);
totalg = sum(g);
normg = g / totalg;
normarea = area / totalarea;

for i = 1:maxr
    finalg(i,1) = normg(i,1) / normarea(i,1);
end

%outputs g(r) to an excel file

```

```
save 'finalg.xls' finalg -ascii
```

**Code 3.** The following Matlab code computes the coordination number of each nanoparticle in a selected image and generates a color-coded defect map.

```
%Computes coordination at each particle and generates a corresponding color
%coded plot
clear;
```

```
%Part 1: Determining coordinates of particle centroids
%Binary (bitmap) image file (use white background, black particles)
original = imread('Filename.tif');
comporiginal = imcomplement(original);
L = bwlabel(comporiginal);
stats = regionprops(L , 'Centroid');
centroids = cat(1 , stats.Centroid);
xcoords(: , 1) = centroids (: , 1);
ycoords(: , 1) = centroids (: , 2);

%Part 2: Calculating coordination of each particle
%defines t as the size of the inputted list of coordinates
t = size(xcoords,1);
tri = delaunay(xcoords,ycoords);
%identifying edges of all triangles
edges = [tri(:, [1 2]);tri(:, [1 3]);tri(:, [2 3])];
%eliminating any repeated edges
edges = unique(sort(edges,2), 'rows');
%number of edges at a point
count = accumarray(edges(:,1),1);
% number of elements in count
m = size(count,1);

%Part 2: Generating color coded image
RGB = label2rgb(L == 1, jet(1), [0 0 0], 'shuffle');
%Length of image side (pixels)
imagesize = 1024;
%Border size (pixels)
border = 24;
for i = 1:m
    if count(i) == 4
        if xcoords(i) < imagesize - border && xcoords(i) > border && ...
            ycoords(i) < imagesize - border && ycoords(i) > border
            RGB =RGB + label2rgb(L == i, [0 1 0], [0 0 0], 'shuffle');
        end
    elseif count(i) == 5
        if xcoords(i) < imagesize - border && xcoords(i) > border && ...
            ycoords(i) < imagesize - border && ycoords(i) > border
            RGB =RGB + label2rgb(L == i, [1 1 0], [0 0 0], 'shuffle');
        end
    elseif count(i) == 6
        if xcoords(i) < imagesize - border && xcoords(i) > border && ...
            ycoords(i) < imagesize - border && ycoords(i) > border
            RGB =RGB + label2rgb(L == i, [1 1 1], [0 0 0], 'shuffle');
        end
    end
end
```

```

elseif count(i) == 7
    if xcoords(i) < imagesize - border && xcoords(i) > border && ...
        ycoords(i) < imagesize - border && ycoords(i) > border
        RGB =RGB + label2rgb(L == i, [0 1 1], [0 0 0], 'shuffle');
    end
elseif count(i) == 8
    if xcoords(i) < imagesize - border && xcoords(i) > border && ...
        ycoords(i) < imagesize - border && ycoords(i) > border
        RGB =RGB + label2rgb(L == i, [1 0 1], [0 0 0], 'shuffle');
    end
end
end
end

imshow (RGB)

```

**Code 4.** The following Matlab code computes the orientation of individual nanoparticles in a selected image and generates a color-coded orientation map.

```

clear;
%Computes and plots relative particle Orientation
%Part 1: Determining coordinates of particle centroids
%Binary (bitmap) image file (use white background, black particles)
original = imread('Filename.tif');
comporiginal = imcomplement(original);
L = bwlabel(comporiginal);
stats = regionprops(L , 'Centroid');
centroids = cat(1 , stats.Centroid);
xcoords(: , 1) = centroids (: , 1);
ycoords(: , 1) = centroids (: , 2);

%defines t as the size of the inputted list of coordinates
t = size(xcoords,1);

%calculating the angle between two points that are separated by a distance
%less than a cutoff distance determined from the PDF (minimum between the
%first and second peaks)and then must be manually inputted into the code
cutoffdist = 23;
alpha = zeros(t,6);

%Part 2: Normalize relative angles into a 60 degree interval
for c=1:t
    jamz = 1;
    for i=1:t
        if (((xcoords(i,1)-xcoords(c,1))^2+(ycoords(i,1)-ycoords(c,1)...
            )^2)^.5) >0) && (((xcoords(i,1)-xcoords(c,1))^2+...
            (ycoords(i,1)-ycoords(c,1))^2)^.5) <= cutoffdist)
            alpha (c,jamz) = (180/pi) * (atan ((ycoords(i,1)-...
            ycoords(c,1)) / (xcoords(i,1)- xcoords(c,1))));
            jamz = jamz + 1;
        end
    end
end
end

jj = size (alpha, 2);

```

```

alphap = zeros (t,jj);

for c=1:t
  for i=1:jj
    if alpha (c,i) > -30 && alpha (c,i) <= 30;
      alphap (c,i) = alpha (c,i);
    elseif alpha (c,i) > 30 && alpha (c,i) <= 90;
      alphap (c,i) = alpha (c,i) - 60;
    elseif alpha (c,i) > 90 && alpha (c,i) <= 150;
      alphap (c,i) = alpha (c,i) - 120;
    elseif alpha (c,i) > 150 && alpha (c,i) <= 210;
      alphap (c,i) = alpha (c,i) - 180;
    elseif alpha (c,i) > 210 && alpha (c,i) <= 270;
      alphap (c,i) = alpha (c,i) - 240;
    elseif alpha (c,i) > 270 && alpha (c,i) <= 330;
      alphap (c,i) = alpha (c,i) - 300;
    elseif alpha (c,i) > 330 && alpha (c,i) <= 360;
      alphap (c,i) = alpha (c,i) - 360;
    elseif alpha (c,i) < -30 && alpha (c,i) >= -90;
      alphap (c,i) = alpha (c,i) + 60;
    elseif alpha (c,i) < -90 && alpha (c,i) >= -150;
      alphap (c,i) = alpha (c,i) + 120;
    elseif alpha (c,i) < -150 && alpha (c,i) >= -210;
      alphap (c,i) = alpha (c,i) + 180;
    elseif alpha (c,i) < -210 && alpha (c,i) >= -270;
      alphap (c,i) = alpha (c,i) + 240;
    elseif alpha (c,i) < -270 && alpha (c,i) >= -330;
      alphap (c,i) = alpha (c,i) + 300;
    elseif alpha (c,i) < -330 && alpha (c,i) >= -360;
      alphap (c,i) = alpha (c,i) + 360;
    end
  end
end

%finding the zero values in alphap
[row0,col0,val0] = find(alphap == 0);
row00 = unique (row0);
counted=hist(row0(:),row00)';
teto = size (row00,1);

%finding the nonzero values in alphas
[rows,cols,vals] = find(alphap ~= 0);

%creating a variable the size of the number of nonzero alphap values
dfd = size(rows,1);

%creating variables same length as the number of original inputted
%coordinates
totalangle=zeros(t,1);
countz=zeros(t,1);

%Part 3: Calculate the average orientation of each particle
%for each specific point all angles are added together and a count of how
%is kept track of 'countz'

```

```

for j = 1:t
    for i=1:dfd
        if rows(i,1) == j;
            totalangle(j,1) = alphap(rows(i,1), cols(i,1)) + ...
                totalangle(j,1);
            countz(j,1) = countz(j,1) +1;
        end
    end
end

%creating a variable to hold the average angle calculations
averageangle = zeros(t,1);

%at each point the average angle is calculated
for j = 1:t
    averageangle(j,1) = totalangle(j,1) / countz(j,1);
end

%rounding averageangle values to nearest integer
raverageangle = round(averageangle);
ind = find(isnan(raverageangle));
raverageangle(ind)=0;
tiny = abs(min (raverageangle)) + 1;
transaa = size(raverageangle,1);

for i=1:t
    transaa(i,1) = raverageangle(i,1) + tiny + (min(raverageangle)+ 30) ;
end

c=colormap(jet(61));
RGB = label2rgb(L == 1, jet(1), [0 0 0], 'shuffle');

for i = 1:t
    RGB =RGB + label2rgb(L == i, c(transaa(i,:),:), [0 0 0], 'shuffle');
end

for i = 1:teto
    if jj - counted(i) ~= 6
        RGB =RGB + label2rgb(L == row00(i), [1 1 1], [0 0 0], 'shuffle');
    end
end

imshow (RGB)

```

### **8.3 Addendum**

In the research presented, BF-TEM images were acquired and analyzed. The use of HAADF-STEM images in the place of BF-TEM images could also be beneficial. Specifically, the HAADF-STEM images are incoherent, and the contrast mechanism is only mass-thickness and does not contain diffraction contrast as BF-TEM images do. This means all the NPs will always appear bright on a dark background regardless of microscope conditions such as defocus (assuming the thickness and or mass of the substrate are lower than that of the NPs). Moreover without any diffraction contrast mechanism contributing, the NPs will be approximately uniform in appearance. All of these properties of HAADF-STEM images would make conversion from the raw image into the required binary image for analysis simpler than for a BF-TEM image.

## CHAPTER 9

### **Sinter-Free Phase Conversion and Scanning Transmission**

### **Electron Microscopy of FePt Nanoparticle Monolayers**

The following material was published in *Nanoscale* (Vol. 3, No. 10, pp. 4142-4149, 2011) as “Sinter-free phase conversion and scanning transmission electron microscopy of FePt nanoparticle monolayers” by Aaron C. Johnston-Peck, Giovanna Scarel, Junwei Wang, Gregory N. Parsons, and Joseph B. Tracy. Johnston-Peck’s contribution to the research included synthesizing the FePt NPs, assembling the NP monolayers, heat treating the samples, collecting and analyzing the TEM data, and writing the manuscript.

#### **9.1 Motivation**

NPs are very susceptible to thermally induced aggregation and sintering due to their high surface area to volume ratio. This proves to be a significant challenge in several fields, including catalysis<sup>1-3</sup> and phase conversions. The  $L1_0$  intermetallic phase of FePt is very attractive as a material for use in BPM because of its extremely large magnetocrystalline anisotropy. Wet-chemistry synthesis methods produce an alloy phase, however, whose magnetic properties are not useful for of BPM. The ligands coating the surface of FePt NPs after wet-chemical synthesis are amiable to self-assembly, yet if the NPs were to be in the  $L1_0$  phase, they would be ferromagnetic at room temperature, which would complicate self-assembly due to the strong magnetic dipolar interactions among the NPs. Therefore, an

approach that would facilitate self-assembly into ordered monolayers followed by conversion into the  $L1_0$  intermetallic phase, while maintaining NP size and translational order of an array is highly desirable.

In this research we developed a procedure where, alloy phase FePt NPs were synthesized and self-assembled into a ordered monolayer. Coating by a refractory material and subsequent thermal annealing converted the NPs into  $L1_0$  and  $L1_2$  intermetallic phases while maintaining NP size and order of the monolayer array. These demonstrate significant progress toward the preparation of arrays of  $L1_0$  FePt NPs, and they also highlight important challenges that remain.

## **9.2 Manuscript Reprint**

Cite this: *Nanoscale*, 2011, **3**, 4142

www.rsc.org/nanoscale

PAPER

## Sinter-free phase conversion and scanning transmission electron microscopy of FePt nanoparticle monolayers†

Aaron C. Johnston-Peck,<sup>a</sup> Giovanna Scarel,<sup>‡b</sup> Junwei Wang,<sup>§a</sup> Gregory N. Parsons<sup>b</sup> and Joseph B. Tracy<sup>\*a</sup>

Received 3rd June 2011, Accepted 27th June 2011

DOI: 10.1039/c1nr10567a

Thermally robust monolayers of 4–6 nm diameter FePt nanoparticles (NPs) were fabricated by combining chemical synthesis and atomic layer deposition. Spin-cast monolayers of FePt NPs were coated with thin, 11 nm-thick layers of amorphous Al<sub>2</sub>O<sub>3</sub>, followed by annealing to convert the FePt NPs from an alloy (A1) into intermetallic FePt (L<sub>10</sub>) and FePt<sub>3</sub> (L<sub>12</sub>) phases. The Al<sub>2</sub>O<sub>3</sub> layer serves as a barrier that prevents sintering between NPs during annealing at temperatures up to 730 °C. Electron and X-ray diffraction in conjunction with high-angle annular dark-field scanning transmission electron microscopy (HAADF-STEM) show that as-synthesized A1 FePt NPs convert into L<sub>10</sub> and L<sub>12</sub> phase NPs through annealing. HAADF-STEM measurements of individual NPs reveal imperfect ordering and show that the NP composition determines which intermetallic phase is obtained. Mixed-phase NPs with L<sub>10</sub> cores and FePt<sub>3</sub> L<sub>12</sub> shells were also observed, as well as a smaller number of unconverted A1 NPs. These results highlight the need for improved control over the compositional uniformity of FePt NPs for their use in bit-patterned magnetic recording.

### Introduction

Increasing the areal density of magnetic recording media requires new, nanostructured materials.<sup>1</sup> Monolayers of monodisperse ferromagnetic nanoparticles (NPs) are envisioned as future bit-patterned media, which can potentially extend the storage limit beyond 15 Tbit/in<sup>2</sup>.<sup>2</sup> Smaller NP sizes increase the areal density but also make the NPs' magnetic moments more susceptible to ambient thermal energy-induced fluctuations (superparamagnetism), which randomizes each NP's magnetization direction, thus preventing information storage. The magnetocrystalline anisotropy energy of a single-crystalline magnetic NP is  $KV$ , the product of the magnetocrystalline anisotropy constant ( $K$ ) and the NP core volume ( $V$ ). Obtaining ferromagnetic behavior in the absence of other sources of magnetic anisotropy requires  $KV$  values that significantly exceed thermal energy,  $k_B T$ .

Therefore, extremely hard magnets with large  $K$  are needed for bit-patterned media, such as intermetallic (L<sub>10</sub>) FePt<sup>3</sup> with  $K$  of  $7 \times 10^7$  erg/cm<sup>3</sup>.<sup>4</sup> For stable bits,  $KV$  in excess of  $60k_B T$  at room temperature is required, which corresponds to a minimum L<sub>10</sub> FePt NP diameter of 4 nm.<sup>1</sup> Monodisperse, ligand-stabilized FePt NPs synthesized by wet-chemical methods can be patterned into monolayers through self-assembly.<sup>5</sup> Unfortunately, with few exceptions, wet-chemical methods result in chemically-disordered, alloy (A1) FePt NPs whose magnetic properties are not useful for magnetic storage without conversion into the thermodynamically-favored L<sub>10</sub> phase. Even if L<sub>10</sub> FePt NPs could be directly synthesized in solution, the stronger interparticle interactions for ferromagnetic NPs might complicate self-assembly into monolayers for bit-patterned media.

In the A1 phase, both Fe and Pt are randomly distributed throughout the unit cell (Fig. 1a). Thermal annealing will convert FePt alloys with compositions of approximately 41–57 at % Fe<sup>6</sup> into the intermetallic face-centered tetragonal (fct) L<sub>10</sub> phase (Fig. 1b), in which layers of Fe and Pt atoms alternate along the  $c$ -axis. The difference between the Fe and Pt atomic radii causes the unit cell to compress along the  $c$ -axis. Alloys without precisely equimolar compositions, however, are unable to achieve ideal long-range chemical ordering ( $S = 1$ ), and the maximum order attainable is given by the relation,  $S_{max} = 1 - 2\Delta x$ , where  $\Delta x$  is the deviation of the mole fraction of either component from an equimolar composition. As the alloy becomes increasingly Fe-deficient, the intermetallic face-centred cubic (fcc) L<sub>12</sub> FePt<sub>3</sub> phase will form (Fig. 1c). An Fe-rich L<sub>12</sub> Fe<sub>3</sub>Pt phase also exists but was not observed in this study, where the compositions were Pt-rich. The L<sub>10</sub> and L<sub>12</sub> phases can both

<sup>a</sup>Department of Materials Science and Engineering, North Carolina State University, Raleigh, NC, 27695, USA. E-mail: jtracy@ncsu.edu

<sup>b</sup>Department of Chemical and Biomolecular Engineering, North Carolina State University, Raleigh, NC, 27695, USA

† Electronic supplementary information (ESI) available: Representative transmission electron microscopy images of the as-synthesized nanoparticles and of a nanoparticle multilayer, selected-area electron diffraction, energy dispersive X-ray spectra, additional filtered and unfiltered high-angle annular dark-field scanning transmission electron microscopy images, and details of the image simulations. See DOI: 10.1039/c1nr10567a

‡ Current Address: Department of Physics and Astronomy, James Madison University, Harrisonburg, VA 22807, USA

§ Current Address: Department of Materials Science and Engineering, Rensselaer Polytechnic Institute, Troy, NY 12180, USA

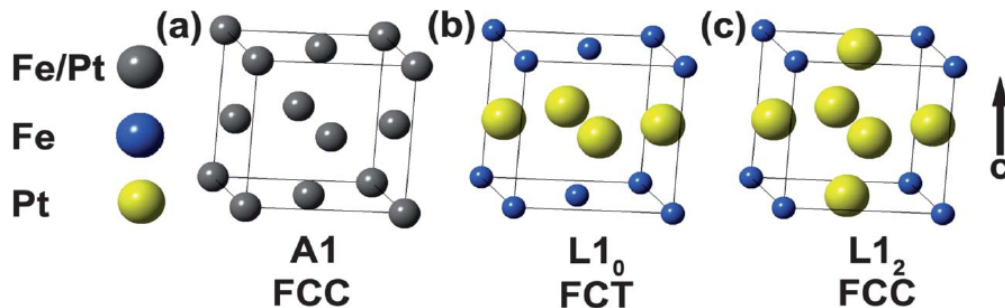


Fig. 1 Models of the unit cells for the different phases of FePt: (a) A1 alloy, face-centered cubic, (b)  $L1_0$  FePt intermetallic, face-centered tetragonal, and (c)  $L1_2$  FePt<sub>3</sub> intermetallic, face-centered cubic.

be identified by diffraction peaks for mixed even and odd indices (e.g., the  $\{001\}$  or  $\{110\}$  families of planes) arising from superlattice planes that are not present for the disordered A1 phase.

Annealing without special precautions causes sintering between NPs.<sup>7</sup> Several approaches have been developed for the phase conversion of FePt NPs with minimal sintering: salt (NaCl) matrix annealing,<sup>8</sup> pulsed laser annealing,<sup>9</sup> rapid thermal annealing,<sup>10</sup> ion-beam irradiation,<sup>11</sup> metal additives that lower the onset temperature of ordering,<sup>12–14</sup> overcoating particles with materials such as MgO,<sup>15,16</sup> SiO<sub>2</sub>,<sup>17–20</sup> iron oxide,<sup>21</sup> or carbon,<sup>22</sup> incorporating the NPs in thin films and matrices,<sup>23–25</sup> and affixing NPs to substrates functionalized with self-assembled monolayers (SAMs) of aliphatic compounds<sup>26–28</sup> have been demonstrated. Very recently, Kong *et al.* reported atomic layer deposition (ALD) of thin, amorphous Al<sub>2</sub>O<sub>3</sub> films on layers of FePt NPs supported on Si wafers.<sup>29</sup> Here, we have employed a similar approach of depositing thin, amorphous Al<sub>2</sub>O<sub>3</sub> films on spin-cast FePt NP monolayers supported on SiN membranes that facilitate characterization by electron microscopy.<sup>30</sup> The Al<sub>2</sub>O<sub>3</sub> coating serves as a diffusion barrier that prevents the NPs from agglomerating and coalescing, while allowing conversion into the  $L1_0$  or  $L1_2$  phases.

ALD is a variant of chemical vapor deposition, where a pair of precursor gases is successively exposed to a reactive surface in self-terminating steps that allow for fine control over the deposition. ALD is known to give highly conformal, uniform coatings with minimal defects.<sup>31</sup> The film thickness per cycle of successive exposures depends on the material deposited. For Al<sub>2</sub>O<sub>3</sub> ALD at moderate temperatures, the film grows at a rate of  $\sim 1.1$ – $1.2$  Å/cycle, and the total film thickness can be precisely controlled by varying the number of deposition cycles. In related reports, ligand-stabilized semiconductor quantum dots have been embedded in Al<sub>2</sub>O<sub>3</sub><sup>32</sup> or ZnO<sup>33</sup> by ALD. Al<sub>2</sub>O<sub>3</sub> coatings deposited by ALD have also been used to stabilize Ag nanostructures for surface-enhanced Raman scattering at temperatures of 400–500 °C.<sup>34,35</sup> Here, we demonstrate the use of thin Al<sub>2</sub>O<sub>3</sub> films as diffusion barriers at temperatures up to 730 °C that prevent sintering among NPs in close-packed layers, where the separation distance between NP surfaces is  $\sim 2$ – $3$  nm. These results substantially agree with those recently reported by Kong *et al.*,<sup>29</sup> but there are also significant differences, and we describe and discuss significant results that they did not report.

FePt NPs with diameters of 4–6 nm and different Fe:Pt compositions were synthesized by thermally decomposing iron pentacarbonyl and platinum(II) acetylacetonate in the presence of oleylamine and oleic acid in benzyl ether. FePt NP monolayers were formed by spin casting NP solutions onto SiN membranes. After removing the ligands, the monolayers were coated with amorphous Al<sub>2</sub>O<sub>3</sub> *via* ALD. The coated NPs were then annealed at various temperatures, which converts the alloy FePt NPs into intermetallic phases. The Al<sub>2</sub>O<sub>3</sub> barrier successfully prevents sintering between NPs and maintains translational order in the monolayers. Measurements by high-angle annular dark-field scanning transmission electron microscopy (HAADF-STEM, also known as Z-contrast STEM) have enabled a detailed study of phase transformations within single NPs and show that compositional variations and surface effects reduce ordering ( $S < 1$ ) of the NPs and also generate unanticipated structures, such as NPs consisting of multiple intermetallic phases.

## Experimental

### Nanoparticle synthesis and purification

FePt NPs were synthesized by modifying a method by Liu *et al.*<sup>36</sup> Syntheses were performed using standard airless procedures and as-purchased reagents without any further purification. FePt NPs with diameters of 6 nm and an approximately equimolar Fe:Pt ratio were synthesized as follows: 101 mg (0.25 mmol) platinum(II) acetylacetonate (97%, Sigma Aldrich) and 10.0 mL benzyl ether (99%, Acros) were added to a 100 mL three-neck, round-bottomed flask with a magnetic stir bar. The contents of the flask were degassed for 75 min at room temperature before backfilling with nitrogen and heating to 100 °C. Immediately upon reaching 100 °C, 0.60 mL (1.75 mmol) oleylamine (97%, Pfaltz & Bauer), 0.56 mL (1.75 mmol) oleic acid (99%, Alfa Aesar), and 81  $\mu$ L (0.60 mmol) iron pentacarbonyl (99.5%, Alfa Aesar) were added by syringe. The temperature was maintained at 100 °C for 10 min and was then raised to 250 °C for 60 min. The NPs with 4 nm and 5 nm diameters were synthesized in the same manner but by increasing the final temperature and varying the amounts of Fe(CO)<sub>5</sub>, oleylamine, and oleic acid. After cooling the flask to room temperature, methanol was added to flocculate the NPs, followed by centrifugation to separate the

NPs from the benzyl ether and reaction side products. The supernatant was decanted and discarded, and the NPs were dispersed in hexanes. A second purification cycle was performed by adding ethanol to flocculate the NPs, followed by centrifugation to isolate the NPs, which were then redispersed in hexanes.

#### Monolayer preparation

NPs suspended in hexanes were spin cast<sup>30</sup> on SiN membranes (DuraSiN DTF-05523) supplied by Protochips, Inc. A Laurel Technologies Model WS-650S-6NPP/LITE spin coater was used in conjunction with a custom-fabricated teflon chuck designed to support the SiN membrane. The as-received membranes were treated in a Jelight Model 144-A ultraviolet light with ozone (UVO) cleaner, operating at ambient atmosphere for 5 min. After depositing 10  $\mu\text{L}$  of a  $\sim 1$  wt % solution of NPs, spinning was started with an acceleration rate of 500 rpm/s to 3000 rpm, at which spinning continued for 60 s.

#### Atomic layer deposition

The SiN substrates received a second UVO treatment for 5 min after NP monolayer deposition to remove organics and to increase the surface coverage of silanol groups on the SiN substrate.<sup>30,37</sup> The FePt NPs were coated with amorphous  $\text{Al}_2\text{O}_3$  films deposited in a hot wall, viscous flow ALD reactor<sup>38</sup> at 100 °C by alternating exposures (1 s) to trimethylaluminum (TMA) and deionized water, which served as aluminum and oxygen sources, respectively. A total of 100 TMA and 100 water exposures were performed. The TMA and water exposures were separated by long purges under Ar: 30 s after TMA exposure and 60 s after water exposure. Long purge times are required for eliminating residual precursor and reaction by-products at low growth temperatures.<sup>38</sup> In a control experiment, the  $\text{Al}_2\text{O}_3$  layer was deposited on a Si(100) substrate with a native oxide layer. A thickness of 11 nm was measured by ellipsometry (AutoEL, Rudolph Technologies).

#### Heat treatment

Samples were annealed in a tube furnace under forming gas (5%  $\text{H}_2$  in 95%  $\text{N}_2$ ) flowing at a rate of approximately 3 cubic feet per minute.

#### Characterization

A JEOL 2000FX microscope operating at 200 kV was used to acquire bright-field transmission electron microscopy (TEM) images, selected-area electron diffraction (SAED), and energy dispersive X-ray spectroscopy (EDS). The camera length was calibrated using an evaporated Al standard, and the NP average sizes were determined by manually measuring the diameter of a minimum of 150 NPs using Image J.<sup>39</sup> Each recorded NP diameter was the average of two measurements taken orthogonal to each other. The Cliff-Lorimer method was used for quantification of the EDS data. For determining the  $k$  ratio, an EDS standard was prepared using an FePt NP sample whose composition was measured by inductively coupled plasma optical emission spectroscopy (ICP-OES), conducted by

Galbraith Laboratories. Z-contrast STEM images were acquired on a JEOL 2010F microscope using a high-angle annular dark-field (HAADF) detector operating at 200 kV. STEM images were digitally processed post-acquisition using filtering to reduce noise while maintaining intensity information. Fast Fourier transforms (FFTs) of the images were generated, and masks were placed on the (000) reflection and Bragg reflections, which contain the background and structural intensity information, respectively. Information not covered by the masks was discarded; an inverse FFT of the remaining information gave the final image. X-ray diffraction (XRD) was performed using a Bruker D-5000 diffractometer (Cu  $K_\alpha$  X-ray source) equipped with a Hi-Star area detector. HAADF-STEM simulations were performed using QSTEM software.<sup>40</sup> Details of the simulations are given in the Supporting Information.†

## Results and discussion

#### Monolayer arrays

Three batches of FePt NPs were synthesized with average diameters of 4.2, 4.9, and 5.9 nm and average compositions of  $\text{Fe}_{19}\text{Pt}_{81}$ ,  $\text{Fe}_{37}\text{Pt}_{63}$ , and  $\text{Fe}_{47}\text{Pt}_{53}$ , respectively. Representative results from TEM, SAED, and EDS for each sample are presented in the Supporting Information, Figures S-1–S-6.†

The NPs were spin cast onto SiN membranes, and the NP concentration in the spin casting solution was adjusted to favor formation of monolayers and submonolayers. Alternatively, other techniques could be employed for preparing NP monolayers, such as assembly at a liquid-air interface.<sup>41</sup> For some samples, partial multilayers formed, where NPs were stacked on top of each other, giving the appearance in TEM images of overlapping NPs (*e.g.*, Supporting Information, Figure S-7).† The NP monolayers include both close-packed and disordered regions, which may result from the NP size distribution or from non-spherical and irregular NP shapes that could frustrate assembly.<sup>30</sup> The average interparticle spacing (between the inorganic surfaces of the NPs) is approximately 2–3 nm in ordered regions and varies in the disordered regions from 2 nm to more than 4 nm.  $\text{Al}_2\text{O}_3$  thin films were deposited on the NP monolayers by 100 cycles of ALD, which gave a  $\sim 11$  nm-thick film in a control sample on a bare Si wafer with its native oxide layer.

#### Monolayer stability

TEM images of 4 nm FePt NP monolayers after different extents of processing are shown in Fig. 2. The variation in contrast between NPs primarily reflects differences in diffraction contrast, because the NPs have random crystal orientations. NPs with orientations that satisfy Bragg's law scatter the electron beam more strongly and appear darker. After coating with  $\text{Al}_2\text{O}_3$  (panel a) the array remained structurally intact with fully isolated NPs, the same as before coating. After annealing at 730 °C for 5 h, followed by an additional 3 h at 600 °C (panel b), the NP sizes and the film morphology were preserved. This two-stage heat treatment was chosen, because the critical ordering temperature in FePt NPs is suppressed as a function of size, and a stepped annealing process ensures more complete transformation of all sizes of NPs.<sup>42</sup> The NP diameters remain at  $\sim 4$  nm even after

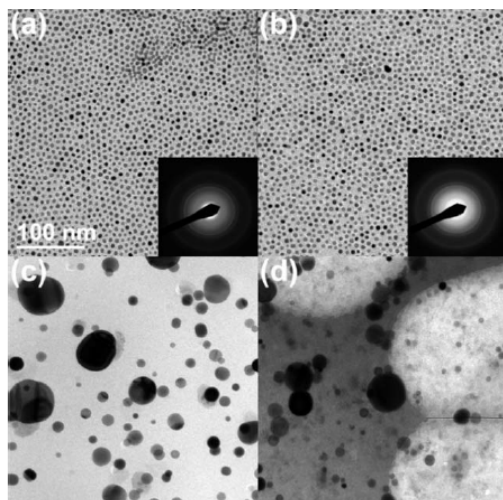


**Fig. 2** TEM images (common scale bar) of monolayers of 4 nm FePt NPs: (a) with an Al<sub>2</sub>O<sub>3</sub> layer, before annealing, (b) with an Al<sub>2</sub>O<sub>3</sub> layer, after annealing (5 h at 730 °C + 3 h at 600 °C), (c) without an Al<sub>2</sub>O<sub>3</sub> layer, after annealing (700 °C for 15 min), and (d) Al<sub>2</sub>O<sub>3</sub>-coated monolayer of 6 nm FePt NPs that sintered after heating at 900 °C for 1 h. Insets (panels a,b): SAED.

prolonged annealing, demonstrating that the Al<sub>2</sub>O<sub>3</sub> thin film serves as an effective diffusion barrier that maintains translational order and minimizes sintering. In comparison, heating an uncoated array for only 15 min at 700 °C causes widespread agglomeration and coalescence into larger NPs (panel c). However, heating the coated array to a higher temperature of 900 °C also causes agglomeration (panel d). Additional related experiments, including those for FePt NPs with 5 nm and 6 nm diameters (Fig. 3) and different heat treatments, gave similar results.

Coating the arrays did not completely eliminate sintering between NPs (*e.g.*, Fig. 3a). Imperfections in the NP monolayer can give rise to sintering. In particular, if some of the NPs stack on top of each other (*i.e.*, begin forming a multilayer) during spin casting, the ligand removal step (by ultraviolet light with ozone

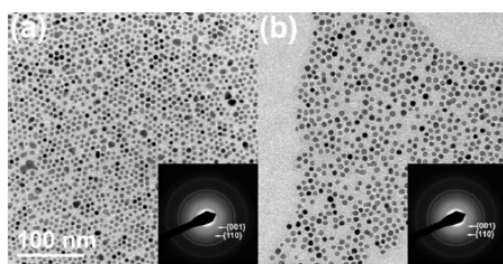


**Fig. 3** TEM images of Al<sub>2</sub>O<sub>3</sub>-coated monolayers of (a) 5 nm and (b) 6 nm FePt NPs after annealing (5 h at 730 °C + 3 h at 600 °C). Insets (panels a,b): SAED.

cleaning) prior to encapsulation would bring the stacked NPs into direct contact with each other. Consequently, the Al<sub>2</sub>O<sub>3</sub> barrier would not prevent such stacked NPs from agglomerating during annealing. Overlapping NPs were observed prior to heat treatments but rarely after annealing, which further supports this explanation of agglomeration resulting from defects formed prior to the ALD coating step. We therefore anticipate agglomeration would be completely eliminated, if the assembly process could be improved to give perfect monolayers with uniform spacing between NPs without multilayer stacking.

Another potential concern might be the presence of any ligands that were not removed by UVO cleaning, even though the UVO treatment should be effective.<sup>43</sup> In a related study, sintering of FePt NPs coated by a sputter deposited layer of SiO<sub>2</sub> was reported, when the ligands were not completely removed prior to depositing the SiO<sub>2</sub> layer.<sup>20</sup> Methyl-terminated alkyl chains are known to be capable of impeding or preventing film growth by ALD.<sup>44–46</sup> However, for highly reactive metal oxide ALD processes, such as Al<sub>2</sub>O<sub>3</sub>, dense and well-ordered organic layers are needed to significantly impede oxide growth.<sup>47</sup> Therefore, some remaining ligands on the NPs would not be expected to significantly impact the stabilizing ability of the ALD thin film coating. Remarkably, Kong *et al.* did not remove the ligands from their FePt NPs prior to Al<sub>2</sub>O<sub>3</sub> growth by ALD, yet the Al<sub>2</sub>O<sub>3</sub> coating prevented sintering during heating.<sup>29</sup> In comparison with our results, their uncoated control samples showed less apparent agglomeration, and partial multilayer regions of their coated samples also experienced less agglomeration than ours. The origins of these differences are unclear, but they might arise from the presence/removal of the ligands prior to Al<sub>2</sub>O<sub>3</sub> deposition, different Al<sub>2</sub>O<sub>3</sub> deposition temperatures, or different substrates (Si *versus* SiN).

The integrity of the Al<sub>2</sub>O<sub>3</sub> film as a diffusion barrier is maintained up to at least 730 °C. Amorphous Al<sub>2</sub>O<sub>3</sub> has been reported to crystallize at ~800–900 °C and increases in density at slightly lower temperatures.<sup>48–50</sup> After heating the Al<sub>2</sub>O<sub>3</sub>-coated NPs to 900 °C (Fig. 2d), the contrast of the Al<sub>2</sub>O<sub>3</sub> film becomes non-uniform, and the NPs undergo substantial sintering, which could be caused by Al<sub>2</sub>O<sub>3</sub> grain nucleation and growth, delamination of the Al<sub>2</sub>O<sub>3</sub> from the NPs and substrate, or densification of the Al<sub>2</sub>O<sub>3</sub>.

Heat treatment induces morphological changes in the FePt NPs. Prior to heating, the 5 nm and 6 nm NPs have an irregular morphology, but after annealing at 730 °C for 5 h + 600 °C for 3 h, the Al<sub>2</sub>O<sub>3</sub>-coated NPs appear rounder in shape (Fig. 4). The high temperature likely causes rounding of the NPs' edges and corners by relaxing the NP and Al<sub>2</sub>O<sub>3</sub> interface. Al<sub>2</sub>O<sub>3</sub> deposited onto Ag NPs by ALD has been reported to prevent morphological changes at temperatures up to 500 °C, but higher temperatures were not investigated.<sup>34</sup> Kong *et al.* likewise did not investigate rounding of irregularly shaped FePt NPs covered by Al<sub>2</sub>O<sub>3</sub> during heating to 700 °C.<sup>29</sup>

#### Intermetallic phase conversions

Both SAED (Fig. 3, inset) and X-ray diffraction (XRD, Fig. 5) measurements show that annealing drives the conversion of the coated NPs with diameters of 5 nm and 6 nm into ordered intermetallic phases, which have additional superlattice

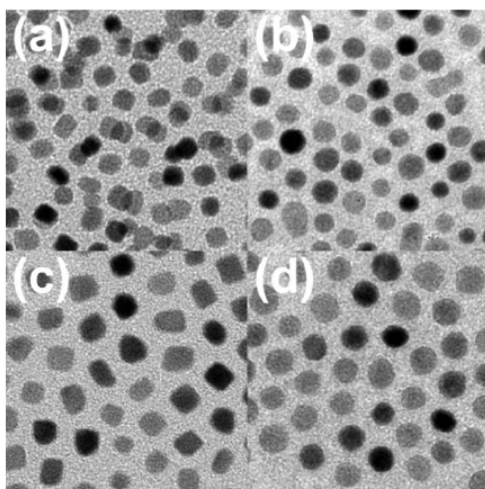


Fig. 4 TEM images of FePt NPs with diameters of (a) 5 nm, before annealing, (b) 5 nm, after annealing with  $\text{Al}_2\text{O}_3$  coating, (c) 6 nm, before annealing, and (d) 6 nm, after annealing with  $\text{Al}_2\text{O}_3$  coating.

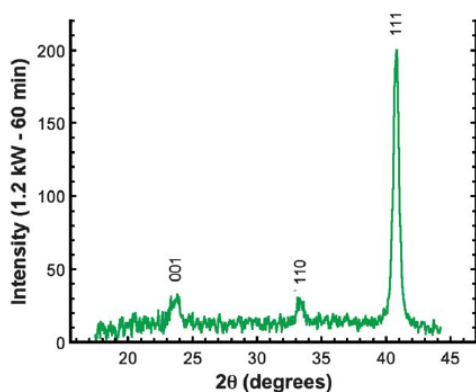


Fig. 5 XRD of an  $\text{Al}_2\text{O}_3$ -coated monolayer of 6 nm FePt NPs after annealing for 5 h at  $730^\circ\text{C}$  + 3 h at  $600^\circ\text{C}$  that converted into the  $\text{L1}_0$  phase.

reflections, the  $\{001\}$  and  $\{110\}$  planes. HAADF-STEM enables detailed characterization of the  $\text{L1}_0$  and  $\text{L1}_2$  phases in individual NPs. For the 4 nm NPs, HAADF-STEM measurements reveal that the conversion occurs, even though the SAED and XRD data do not show evidence of the transformation. Diffraction techniques are less sensitive for small NPs, particularly when arranged in a monolayer consisting of a very small amount of material.

In HAADF-STEM, the signal intensity for each atomic column is proportional to the average atomic weight of the atoms in the column. The large difference in atomic number between Fe ( $Z = 26$ ) and Pt ( $Z = 78$ ) enables facile identification of atomic columns that are rich in either Fe or Pt atoms, which are present

in the intermetallic phases. In certain orientations with respect to the electron beam (the zone axis), superlattice planes in a NP with intermetallic ordering give rise to alternating columns of Pt or Fe atoms.<sup>51,52</sup> For other crystal orientations with respect to the electron beam, the superlattice will have atomic columns that alternate between Fe and Pt atoms, which gives no difference in Z-contrast for different atomic columns. There is no simple method using Z-contrast STEM or high-resolution TEM to evaluate the proportion of NPs that have transformed from the  $\text{A1}$  to  $\text{L1}_0$  or  $\text{L1}_2$  phase, because the NPs have many different orientations on the substrate. For certain zone axes, Z-contrast images allow determination of the phase using line intensity profiles and FFTs in conjunction with simulations using JEMS software.<sup>53</sup> The Z-contrast images shown in Fig. 6–8 were acquired from each sample after coating and heat-treatment ( $730^\circ\text{C}$  for 5 h +  $600^\circ\text{C}$  for 3 h).

Based on the Fe-Pt phase diagram, the 4 nm ( $\text{Fe}_{19}\text{Pt}_{81}$ ) and 5 nm ( $\text{Fe}_{37}\text{Pt}_{63}$ ) NPs would be expected to convert into the  $\text{L1}_2$  ( $\text{FePt}_3$ ) phase, and the 6 nm NPs ( $\text{Fe}_{47}\text{Pt}_{53}$ ) into the  $\text{L1}_0$  phase.<sup>6</sup> The results generally follow this trend (Fig. 6), but there are some deviations (Fig. 7–8 and Supporting Information, Figures

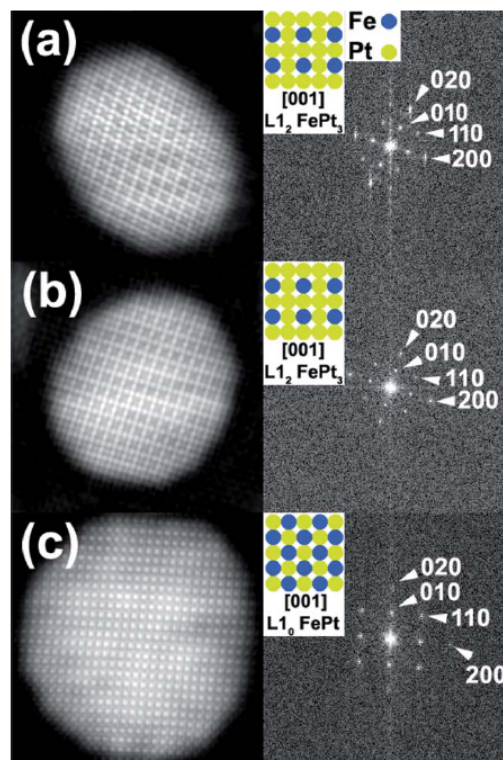


Fig. 6 Filtered HAADF-STEM images with corresponding Fourier transforms (before noise filtering) and cartoons illustrating the ordering: (a)  $\text{L1}_2$ - $\text{FePt}_3$  NP from the 4 nm sample, (b)  $\text{L1}_2$ - $\text{FePt}_3$  NP from the 5 nm sample, and (c)  $\text{L1}_0$ -FePt NP from the 6 nm sample. Each NP was imaged along the  $[001]$  zone axis.

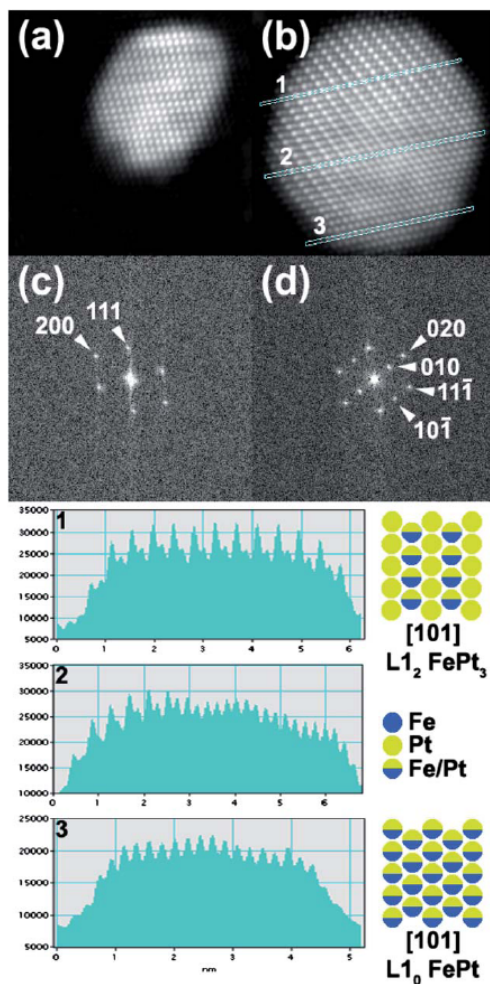


Fig. 7 Filtered HAADF-STEM images with corresponding Fourier transforms (before noise filtering) of (a,c) an Al NP from the 4 nm sample, imaged along the [011] zone axis, and (b,d) a mixed-phase L<sub>10</sub>-FePt/L<sub>12</sub>-FePt<sub>3</sub> NP from the 6 nm sample, imaged along the [101] zone axis. Intensity profiles acquired across the NP in panel (b) at three different points show the transition from the L<sub>12</sub> to L<sub>10</sub> phase.

S-9-S-11).<sup>†</sup> While most of the 4 nm NPs acquired L<sub>12</sub> structures, some remained in the Al phase (Fig. 7a,c). The lack of ordering could arise from the small NP size, which often hinders the transformation into an ordered structure. However, several L<sub>12</sub> NPs of approximately the same size were also identified in the sample. Therefore, the main impediment to ordering is probably the compositional distribution, which is a well-known challenge for chemically-synthesized FePt NPs.<sup>54–56</sup> Because of this compositional disorder, certain NPs may be unable to convert from the alloy into an intermetallic phase, or they may convert into an intermetallic phase that differs from the phase predicted by the ensemble composition.

In the 6 nm sample, NPs simultaneously containing L<sub>12</sub> and L<sub>10</sub> phases were frequently identified, and the proportion varies from predominately L<sub>10</sub> to predominately L<sub>12</sub>. There have been a limited number of reports on FePt<sup>51,52</sup> and FePd<sup>57</sup> NPs consisting of mixed intermetallic phases. The transition between the L<sub>12</sub> and L<sub>10</sub> phases is continuous and defect-free, which is consistent with the crystal structures (Fig. 1) and with a gradual transition that would release interfacial stress and facilitate epitaxy, as indicated by the intensity profiles in Fig. 7. For example, the 6 nm NP in Fig. 7b has L<sub>12</sub> ordering with contrasting atomic columns in one part of the NP and L<sub>10</sub> ordering without contrast between atomic columns in another part of the NP. In many other instances, the L<sub>12</sub> phase appears on edges of the NP (Fig. 8 and Supporting Information, Figures S-10-S-11).<sup>†</sup> Separate regions of the L<sub>12</sub> phase can also form independently within the same NP (e.g., Fig. 8a). These results suggest that the surfaces of the NPs are enriched in Pt, which implies that Pt atoms diffuse toward the surface. It is known that FePt NPs synthesized by wet-chemical methods usually grow through nucleation of a Pt seed, followed by growth of Fe on the seed,<sup>36,58</sup> resulting in Pt-rich cores and Fe-rich shells.<sup>59,60</sup> This outward diffusive flux and preferential formation of the L<sub>12</sub> phase at the surfaces of the NPs upon annealing is likely driven by surface effects that favor having Pt atoms at or near the surface of the NP, such as reduced surface energy or strain relaxation.<sup>61–66</sup> Inhomogeneous phases within NPs, especially Pt-rich shells that leave Pt-deficient cores, will reduce the chemical order parameter (*S*) of the NPs. Such FePt(core)/FePt<sub>3</sub>(shell) NPs might also be an interesting system for investigating exchange bias, because L<sub>12</sub> FePt<sub>3</sub> is antiferromagnetic<sup>67</sup> and could exchange couple with the ferromagnetic FePt. Exchange bias has been observed in nanocrystalline FePt/FePt<sub>3</sub> systems.<sup>68</sup>

The chemical ordering within single NPs varies, but quantitative measurements of *S* are beyond the scope of this study. For NPs oriented with a [001] zone axis, perfectly ordered L<sub>10</sub> and L<sub>12</sub> structures are expected to have alternating columns of Fe and Pt. Comparisons of the atomic column intensities within single NPs with [001] zone axis measured by HAADF-STEM reveal variations in the atomic weight differences (exceeding noise) between neighboring Fe and Pt columns. These fluctuations indicate that antisite defects are present, which implies that *S* < 1 and can vary locally within each NP. However, without the proper experimental setup and image simulations, accurate quantitative interpretation of the intensity is impossible,<sup>69</sup> and values of *S* cannot be assigned in this study. Changes in parameters such as the specimen thickness or microscope defocus<sup>70,71</sup> can also cause intensity variations. These sources of variation were eliminated from our analysis by removing the background signal from the unprocessed images, and the atomic column intensities were compared for nearest neighbors, between which there is minimal change in specimen thickness.<sup>72</sup> Compositional variations within individual NPs reduce order (*S* < 1), and NPs lacking the ideal ratio of Fe to Pt atoms (nearly all of the NPs in this study) for stoichiometric conversion into an intermetallic phase will have less than perfect ordering.<sup>61</sup> Moreover, the distribution of NP compositions is also expected to cause a dispersion of differently ordered transformation products.

Surface effects also reduce ordering. The tendency of Pt to migrate to the surface upon annealing, which has been predicted

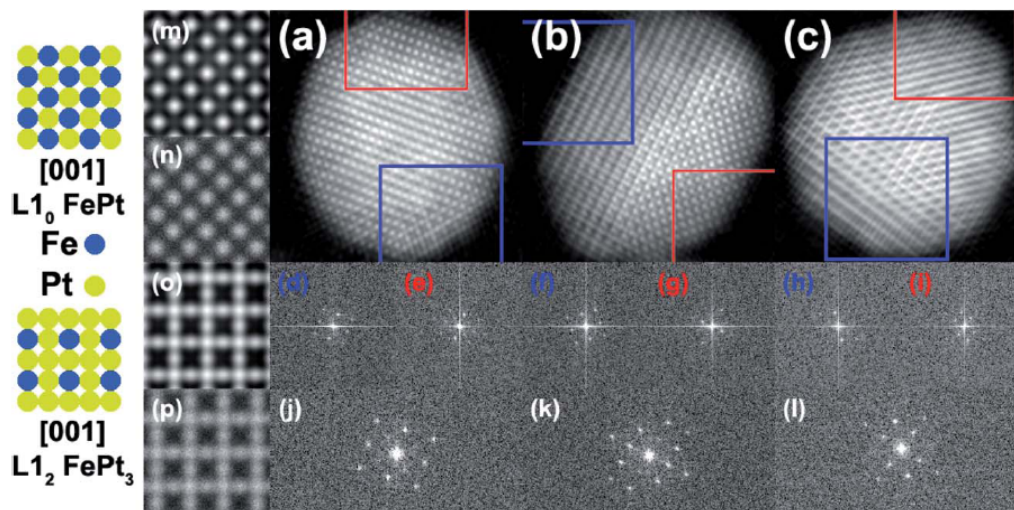


Fig. 8 (a–c) Filtered HAADF-STEM images of 6 nm FePt NPs containing different proportions of the L1<sub>0</sub> and L1<sub>2</sub> phases, imaged along the [001] zone axis. Fourier transforms before noise filtering are shown below each NP: (d–i) selected regions corresponding to the (d,f,h) blue squares that indicate the L1<sub>2</sub> phase and to the (e,g,i) red squares that indicate the L1<sub>0</sub> phase; (j–l) for each entire NP (cropped on the top and bottom). Structure models, (m,o) simulated projected potentials, and (n,p) simulated HAADF-STEM images along the [001] zone axis for the L1<sub>0</sub>-FePt and the L1<sub>2</sub>-FePt<sub>3</sub> phases are provided for comparison.

theoretically<sup>64</sup> and observed experimentally,<sup>65,66</sup> can decrease  $S$  and inhibits the formation of perfectly-ordered L1<sub>0</sub> NPs. This effect is exacerbated in NPs that are Pt-deficient (< 50 at % Pt) and are already unable to form a structure with ideal ordering ( $S = 1$ ). In summary, conversion of the 6 nm NPs into the L1<sub>0</sub> phase was inhibited, because the compositions of individual NPs deviate from the ensemble average. A remaining question is, how significantly can surface effects perturb ordering even in NPs with a perfect Fe<sub>50</sub>Pt<sub>50</sub> composition? The 4 nm and 5 nm NPs are Pt-rich, and stoichiometric deviations from 25 at % Fe usually resulted in an imperfectly ordered ( $S < 1$ ) L1<sub>2</sub> phase without any L1<sub>0</sub> phase present. Finally, we note that atmospheric conditions of annealing or the substrate (in these experiments, simultaneous contact with Al<sub>2</sub>O<sub>3</sub> and SiN) might also significantly affect the phase transformations.<sup>61</sup>

## Conclusions

Monolayers of FePt NPs were coated with a thin film of amorphous Al<sub>2</sub>O<sub>3</sub>, which prevents sintering and preserves assembly of the NPs at temperatures up to 730 °C. Annealing drives the conversion of the encapsulated NPs from the A1 alloy into L1<sub>0</sub> and L1<sub>2</sub> intermetallic phases. Monolayers of L1<sub>0</sub> FePt NPs are of significant interest for bit-patterned magnetic media. At higher temperatures, the Al<sub>2</sub>O<sub>3</sub> crystallizes and the NPs readily agglomerate. An important aspect of this approach is that the NPs are assembled into their final configuration prior to phase transformation. Some other approaches perform self-assembly after transformation into the intermetallic phase, and stronger interparticle interactions or the presence of diffusion barriers

encapsulating the NPs may render self-assembly into ordered structures more challenging.

The Al<sub>2</sub>O<sub>3</sub> coating also facilitates analysis of the NPs by HAADF-STEM. Imaging reveals NPs with mixed phases and a range of chemical ordering, which could negatively impact their use in magnetic recording. The formation of the Pt-rich L1<sub>2</sub> phase on the NP surface is found to be a particular challenge. These results also highlight the need for improved synthetic control over the compositional uniformity of FePt NPs.

The method described here to encase NPs in an ultrathin coating by ALD before annealing is expected to be useful for preventing NPs from sintering at high temperatures for other end uses. In addition to phase transformations, ALD coatings might, for example, maintain uniform, small NP sizes for catalyzing chemical reactions or the growth of carbon nanostructures.

## Acknowledgements

This work was supported by the National Science Foundation (CHE-0943975 and CBET-1034374) and startup funds from North Carolina State University. A.C.J.-P. acknowledges support from a GAANN fellowship. We thank Protochips, Inc. for donating the SiN membranes and Jon-Paul Maria (NCSU) for assistance with XRD and some of the first annealing treatments.

## References

- 1 D. Weller, A. Moser, L. Folks, M. E. Best, W. Lee, M. F. Toney, M. Schwickert, J. U. Thiele and M. F. Doerner, *IEEE Trans. Magn.*, 2000, **36**, 10–15.

- 2 Z. Z. Bandic, D. Litvinov and M. Rooks, *MRS Bull.*, 2008, **33**, 831–834.
- 3 J. P. Wang, *Proc. IEEE*, 2008, **96**, 1847–1863.
- 4 O. A. Ivanov, L. V. Solina, V. A. Demshina and L. M. Magat, *Fiz. Metallov Metalloved.*, 1973, **35**, 92–97.
- 5 S. H. Sun, *Adv. Mater.*, 2006, **18**, 393–403.
- 6 H. Okamoto, *J. Phase Equilib. Diffus.*, 2004, **25**, 395–395.
- 7 Z. R. Dai, S. H. Sun and Z. L. Wang, *Nano Lett.*, 2001, **1**, 443–447.
- 8 K. Elkins, D. Li, N. Poudyal, V. Nandwana, Z. Q. Jin, K. H. Chen and J. P. Liu, *J. Phys. D: Appl. Phys.*, 2005, **38**, 2306–2309.
- 9 S. Saita and S. Maenosono, *J. Phys.: Condens. Matter*, 2004, **16**, 6385–6394.
- 10 H. Zeng, S. H. Sun, R. L. Sandstrom and C. B. Murray, *J. Magn. Magn. Mater.*, 2003, **266**, 227–232.
- 11 J. E. E. Baglin, S. Sun, A. J. Kellock, T. Thomson, M. F. Toney, B. D. Terris and C. B. Murray, *Mat. Res. Soc. Symp. Proc.*, 2003, **777**, T6.5.1–T6.5.6.
- 12 Q. Y. Yan, T. Kim, A. Purkayastha, P. G. Ganesan, M. Shima and G. Ramanath, *Adv. Mater.*, 2005, **17**, 2233–2237.
- 13 S. Kinge, T. Gang, W. J. M. Naber, H. Boschker, G. Rijnders, D. N. Reinhoudt and W. G. van der Wiel, *Nano Lett.*, 2009, **9**, 3220–3224.
- 14 S. S. Kang, Z. Y. Jia, D. E. Nikles and J. W. Harrell, *IEEE Trans. Magn.*, 2003, **39**, 2753–2757.
- 15 J. M. Kim, C. B. Rong, J. P. Liu and S. H. Sun, *Adv. Mater.*, 2009, **21**, 906–909.
- 16 J. Kim, C. B. Rong, Y. Lee, J. P. Liu and S. H. Sun, *Chem. Mater.*, 2008, **20**, 7242–7245.
- 17 Y. Tamada, S. Yamamoto, M. Takano, S. Nasu and T. Ono, *Appl. Phys. Lett.*, 2007, **90**, 162509.
- 18 S. Yamamoto, Y. Morimoto, T. Ono and M. Takano, *Appl. Phys. Lett.*, 2005, **87**, 3.
- 19 D. C. Lee, F. V. Mikulec, J. M. Pelaez, B. Koo and B. A. Korgel, *J. Phys. Chem. B*, 2006, **110**, 11160–11166.
- 20 Y. Ding, S. A. Majetich, J. Kim, K. Barmak, H. Rollins and P. Sides, *J. Magn. Magn. Mater.*, 2004, **284**, 336–341.
- 21 C. Liu, X. W. Wu, T. Klemmer, N. Shukla and D. Weller, *Chem. Mater.*, 2005, **17**, 620–625.
- 22 N. Caiulo, C. H. Yu, K. M. K. Yu, C. C. H. Lo, W. Oduro, B. Thiebaud, P. Bishop and S. C. Tsang, *Adv. Funct. Mater.*, 2007, **17**, 1392–1396.
- 23 Q. Yan, A. Purkayastha, A. P. Singh, H. Li, A. Li, R. V. Ramanujan and G. Ramanath, *Nanotechnology*, 2009, **20**, 025609.
- 24 H. B. Wang, M. J. Zhou, F. J. Yang, J. Wang, Y. Jiang, Y. Wang, H. Wang and Q. Li, *Chem. Mater.*, 2009, **21**, 404–409.
- 25 M. P. Chen, K. Kuroishi and Y. Kitamoto, *IEEE Trans. Magn.*, 2005, **41**, 3376–3378.
- 26 M. Mizuno, Y. Sasaki, A. C. C. Yu and M. Inoue, *Langmuir*, 2004, **20**, 11305–11307.
- 27 Y. Sasaki, M. Mizuno, A. C. C. Yu, M. Inoue, K. Yazawa, I. Ohta, M. Takahashi, B. Jeyadevan and K. Tohji, *J. Magn. Magn. Mater.*, 2004, **282**, 122–126.
- 28 S. M. Momose, H. Kodama, N. Ihara, T. Uzunaki and A. Tanaka, *Jpn. J. Appl. Phys.*, 2003, **42**, L1252–L1254.
- 29 J. Z. Kong, Y. P. Gong, X. F. Li, A. D. Li, J. L. Zhang, Q. Y. Yan and D. Wu, *J. Mater. Chem.*, 2011, **21**, 5046–5050.
- 30 A. C. Johnston-Peck, J. Wang and J. B. Tracy, *Langmuir*, 2011, **27**, 5040–5046.
- 31 S. M. George, *Chem. Rev.*, 2010, **110**, 111–131.
- 32 K. Lambert, J. Dendooven, C. Detavernier and Z. Hens, *Chem. Mater.*, 2011, **23**, 126–128.
- 33 S. H. Kim, P. H. Sher, Y. B. Hahn and J. M. Smith, *Nanotechnology*, 2008, **19**, 365202.
- 34 A. V. Whitney, J. W. Elam, P. C. Stair and R. P. Van Duyne, *J. Phys. Chem. C*, 2007, **111**, 16827–16832.
- 35 E. V. Forno, S. M. Mahurin and S. Dai, *ACS Appl. Mater. Interfaces*, 2010, **2**, 1987–1991.
- 36 V. Nandwana, K. E. Elkins, N. Poudyal, G. S. Chaubey, K. Yano and J. P. Liu, *J. Phys. Chem. C*, 2007, **111**, 4185–4189.
- 37 J. R. Vig, *J. Vac. Sci. Technol., A*, 1985, **3**, 1027–1034.
- 38 G. K. Hyde, K. J. Park, S. M. Stewart, J. P. Hinestroza and G. N. Parsons, *Langmuir*, 2007, **23**, 9844–9849.
- 39 W. S. Rasband, *ImageJ* <http://rsb.info.nih.gov/ij/> (accessed November 1, 2010).
- 40 C. Koch, PhD, Arizona State University, 2002.
- 41 A. Dong, X. Ye, J. Chen and C. B. Murray, *Nano Lett.*, 2011, **11**, 1804–1809.
- 42 K. Sato, *Nat. Mater.*, 2009, **8**, 924–925.
- 43 S. F. Pang, Y. Kurosawa, T. Kondo and T. Kawai, *Chem. Lett.*, 2005, **34**, 544–545.
- 44 W. Lee and F. B. Prinz, *J. Electrochem. Soc.*, 2009, **156**, G125–G128.
- 45 A. Dube, M. Sharma, P. F. Ma, P. A. Ercius, D. A. Muller and J. R. Engstrom, *J. Phys. Chem. C*, 2007, **111**, 11045–11058.
- 46 M. J. Preiner and N. A. Melosh, *Langmuir*, 2009, **25**, 2585–2587.
- 47 R. Chen, H. Kim, P. C. McIntyre and S. F. Bent, *Chem. Mater.*, 2005, **17**, 536–544.
- 48 K. Y. Gao, F. Speck, K. Emtsev, T. Seyller and L. Ley, *J. Appl. Phys.*, 2007, **102**, 094503.
- 49 S. Jakschik, U. Schroeder, T. Hecht, M. Gutsche, H. Seidl and J. W. Bartha, *Thin Solid Films*, 2003, **425**, 216–220.
- 50 G. Krauthaim, T. Hecht, S. Jakschik, U. Schroeder and W. Zahn, *Appl. Surf. Sci.*, 2005, **252**, 200–204.
- 51 J. E. Wittig, J. Bentley, L. F. Allard, M. S. Wellons and C. M. Lukehart, *Microsc. Microanal.*, 2008, **14**, 216–217.
- 52 J. E. Wittig, J. Bentley, L. F. Allard and C. M. Lukehart, *Microsc. Microanal.*, 2010, **16**, 1754–1755.
- 53 P. Stadelmann, *JEMS - Electron Microscopy Software Java Version*, pp. 1999–2011.
- 54 C. Srivastava, J. Balasubramanian, C. H. Turner, J. M. Wiest, H. G. Bagaria and G. B. Thompson, *J. Appl. Phys.*, 2007, **102**, 104310–104318.
- 55 A. C. C. Yu, M. Mizuno, Y. Sasaki and H. Kondo, *Appl. Phys. Lett.*, 2004, **85**, 6242–6244.
- 56 C. Srivastava, D. E. Nikles and G. B. Thompson, *J. Appl. Phys.*, 2008, **104**, 104314.
- 57 K. Sato, J. G. Wen and J. M. Zuo, *J. Appl. Phys.*, 2009, **105**, 093509–093507.
- 58 H. G. Bagaria, D. T. Johnson, C. Srivastava, G. B. Thompson, M. Shamsuzzoha and D. E. Nikles, *J. Appl. Phys.*, 2007, **101**, 104313.
- 59 V. Monnier, M. Delalande, P. Bayle-Guillemaud, Y. Samson and P. Reiss, *Small*, 2008, **4**, 1139–1142.
- 60 M. Delalande, P. R. Marcoux, P. Reiss and Y. Samson, *J. Mater. Chem.*, 2007, **17**, 1579–1588.
- 61 M. Müller and K. Albe, *Phys. Rev. B: Condens. Matter Mater. Phys.*, 2005, **72**, 094203.
- 62 R. V. Chepulsikii, W. H. Butler, A. van de Walle and S. Curtarolo, *Scr. Mater.*, 2010, **62**, 179–182.
- 63 B. Yang, M. Asta, O. N. Mryasov, T. J. Klemmer and R. W. Chantrell, *Acta Mater.*, 2006, **54**, 4201–4211.
- 64 G. Bozzolo, R. A. Lukaszew and J. E. Garces, *Appl. Phys. Lett.*, 2006, **88**, 011915.
- 65 R. M. Wang, O. Dmitrieva, M. Farle, G. Dumpich, H. Q. Ye, H. Poppa, R. Kilaas and C. Kisielowski, *Phys. Rev. Lett.*, 2008, **100**, 017205.
- 66 L. Y. Han, U. Wiedwald, B. Kuerbanjiang and P. Ziemann, *Nanotechnology*, 2009, **20**, 285706.
- 67 S. Maat, O. Hellwig, G. Zeltzer, E. E. Fullerton, G. J. Mankey, M. L. Crow and J. L. Robertson, *Phys. Rev. B: Condens. Matter*, 2001, **63**, 8.
- 68 K. W. Lin, J. Y. Guo, C. Y. Liu, H. Ouyang, J. van Lierop, N. N. Phuoc and T. Suzuki, *Phys. Status Solidi A*, 2007, **204**, 3991–3994.
- 69 J. M. LeBeau, S. D. Findlay, L. J. Allen and S. Stemmer, *Phys. Rev. Lett.*, 2008, **100**, 4.
- 70 Y. Kotaka, *Ultramicroscopy*, 2010, **110**, 555–562.
- 71 D. O. Klenov and S. Stemmer, *Ultramicroscopy*, 2006, **106**, 889–901.
- 72 J. Biskupek, J. R. Jinschek, U. Wiedwald, M. Bendele, L. Han, P. Ziemann and U. Kaiser, *Ultramicroscopy*, 2010, **110**, 820–825.

## Electronic Supplementary Information:

### **Sinter-free phase conversion and scanning transmission electron microscopy of FePt nanoparticle monolayers**

Aaron C. Johnston-Peck,<sup>a</sup> Giovanna Scarel,<sup>‡,b</sup> Junwei Wang,<sup>§a</sup> Gregory N. Parsons,<sup>b</sup> and Joseph B. Tracy<sup>\*a</sup>

<sup>a</sup> Department of Materials Science and Engineering, North Carolina State University, Raleigh, NC, 27695, USA. E-mail: jbracy@ncsu.edu

<sup>b</sup> Department of Chemical and Biomolecular Engineering, North Carolina State University, Raleigh, NC, 27695, USA

<sup>‡</sup> Current Address: Department of Physics and Astronomy, James Madison University, Harrisonburg, VA 22807, USA

<sup>§</sup> Current Address: Department of Materials Science and Engineering, Rensselaer Polytechnic Institute, Troy, NY 12180, USA

**Representative transmission electron microscopy images of the as-synthesized nanoparticles with selected-area electron diffraction:**

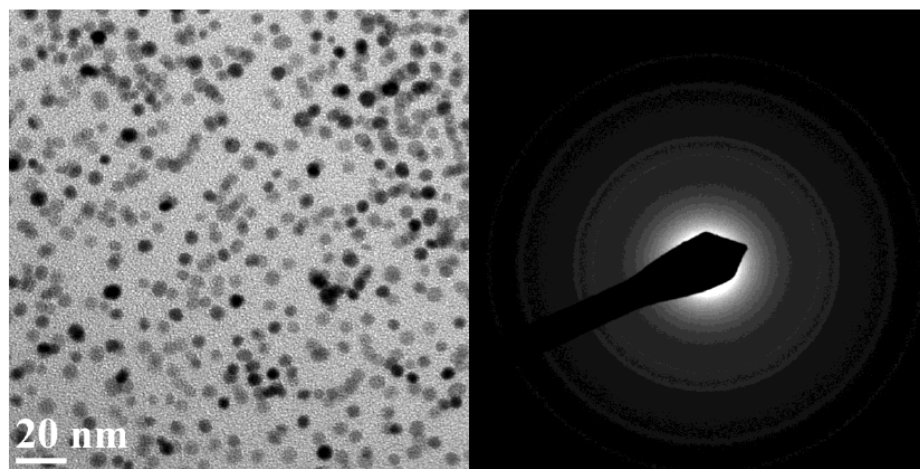


**Figure S-1.** Representative TEM image of 4.2 nm FePt nanoparticles.

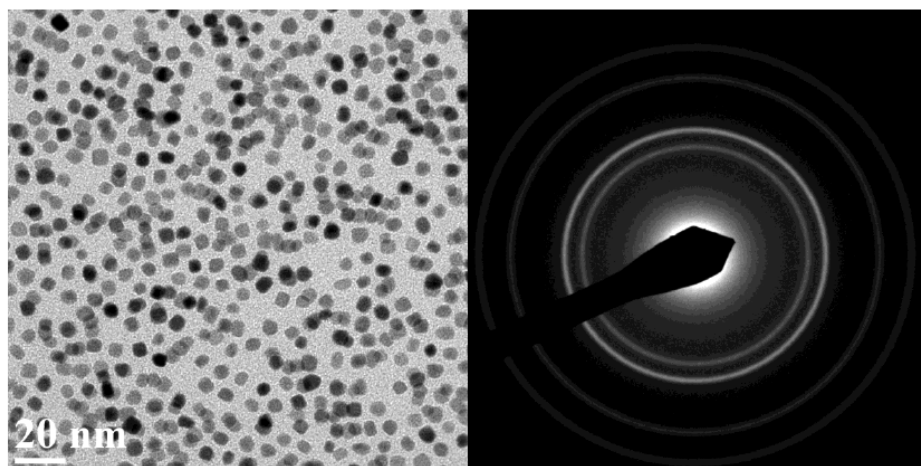


**Figure S-2.** Representative TEM image of 4.9 nm FePt nanoparticles.

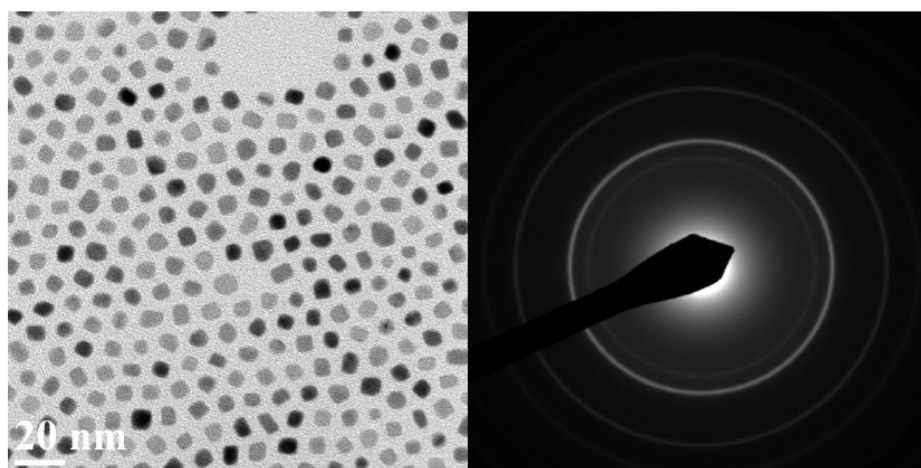


**Figure S-3.** Representative TEM image of 5.9 nm FePt nanoparticles.

**Energy dispersive X-ray spectra:**

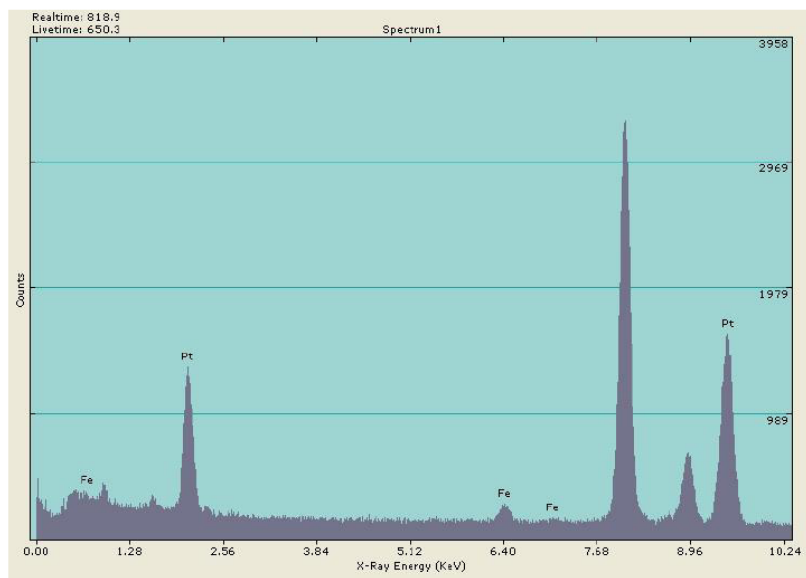


**Figure S-4.** EDS spectrum for 4.2 nm FePt nanoparticles.

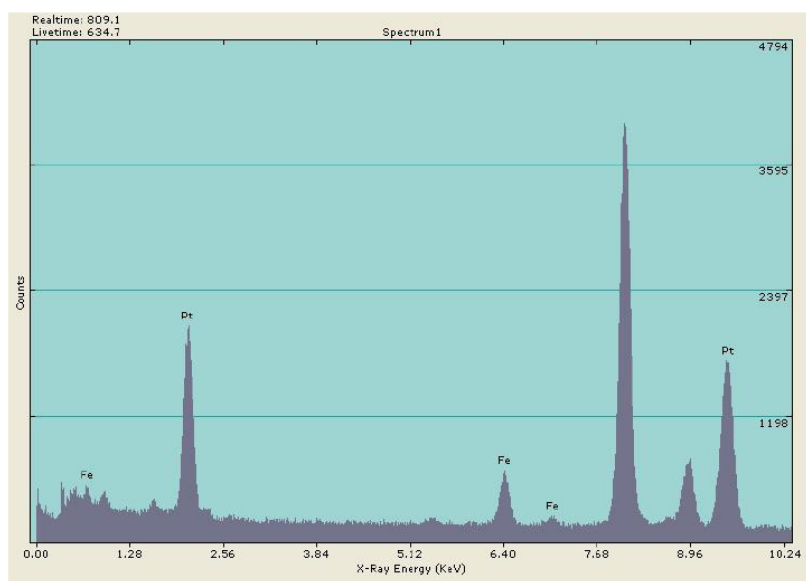


**Figure S-5.** EDS spectrum for 4.9 nm FePt nanoparticles.

ESI-3

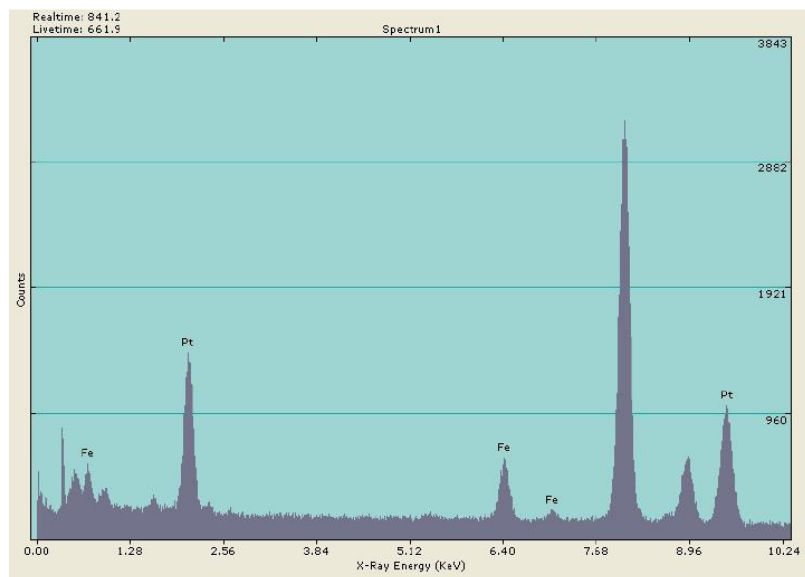


**Figure S-6.** EDS spectrum for 5.9 nm FePt nanoparticles.

**Additional TEM image:**

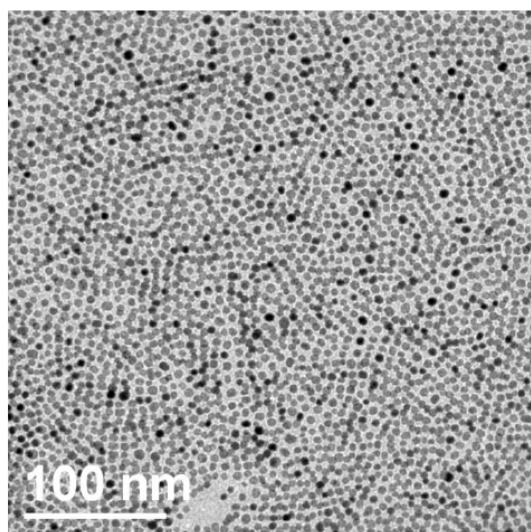


**Figure S-7.** TEM image of a spin cast array of a partial multilayer of 4.2 nm diameter FePt nanoparticles.

ESI-4

**Additional Z-contrast STEM images:**

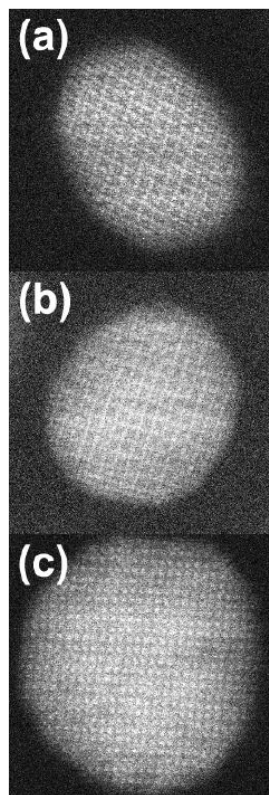


**Figure S-8.** HAADF-STEM images used in Figure 6, before noise filtering.

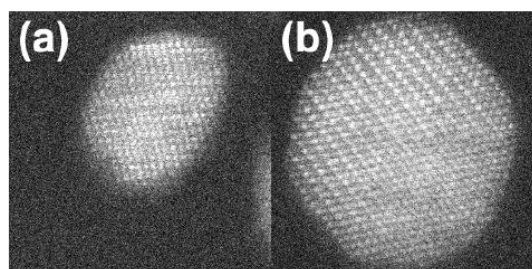


**Figure S-9.** HAADF-STEM images used in Figure 7, before noise filtering.

ESI-5

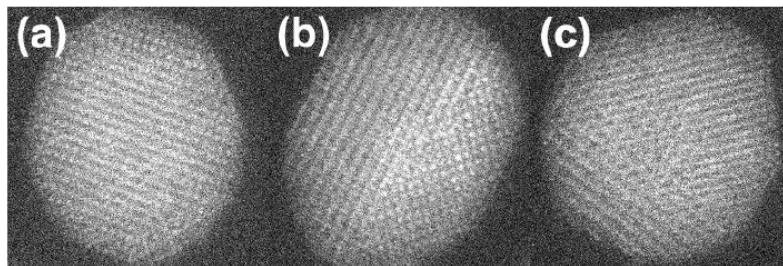


**Figure S-10.** HAADF-STEM images used in Figure 8, before noise filtering.

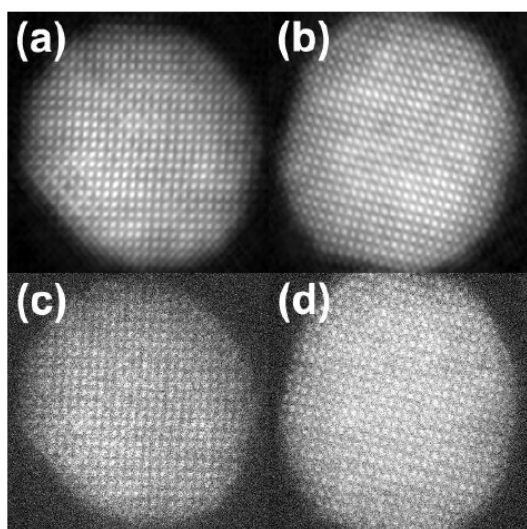


**Figure S-11.** (a-b) Filtered and (c-d) the original, unfiltered HAADF-STEM images showing the presence of the  $\text{FePt}_3$  phase forming on the edges of the nanoparticles.

**Details of Z-contrast STEM image simulation:**

Images were simulated using QSTEM, a program written by Christoph Koch that is based in Matlab and uses a multislice algorithm to compute the wave function at the exit surface of the crystal. The .cfg files used to generate the models employed in the simulation are as follows:

**FePt L1<sub>0</sub>:**

```
Number of particles = 4
A = 1.0 Angstrom (basic length-scale)
H0(1,1) = 3.852 A #
```

```

H0(1,2) = 0 A
H0(1,3) = 0 A
H0(2,1) = 0 A #
H0(2,2) = 3.822 A #
H0(2,3) = 0 A
H0(3,1) = 0 A
H0(3,2) = 0 A
H0(3,3) = 3.713 A #
.NO_VELOCITY.
entry_count = 5
56
Fe
  0.50    0.00    0.50 0.35 1
  0.00    0.50    0.50 0.35 1
195
Pt
  0.00    0.00    0.00 0.37 1
  0.50    0.50    0.00 0.37 1

```

### FePt L1<sub>2</sub>:

```

Number of particles = 4
A = 1.0 Angstrom (basic length-scale)
H0(1,1) = 3.877 A #
H0(1,2) = 0 A
H0(1,3) = 0 A
H0(2,1) = 0 A #
H0(2,2) = 3.877 A #
H0(2,3) = 0 A
H0(3,1) = 0 A
H0(3,2) = 0 A
H0(3,3) = 3.877 A #
.NO_VELOCITY.
entry_count = 5
56
Fe
  0.50    0.00    0.50 0.35 1
195
Pt
  0.00    0.00    0.00 0.37 1
  0.50    0.50    0.00 0.37 1
  0.00    0.50    0.50 0.37 1

```

The lattice parameters are from JCPDS files (43-1359 and 29-716), and the Debye-Waller factors from the literature.<sup>1</sup> A  $10 \times 10 \times 15$  unit cell box was simulated with zero tilt in all directions. A scan window of  $15 \text{ \AA} \times 15 \text{ \AA}$  and a scan length of 25 pixels in each direction were chosen. The model was sliced into two horizontal slabs with 30 slices per slab. Microscope parameters were then selected that would *approximately* mimic the experimental setup used on the JEOL 2010F: voltage: 200 kV, defocus: -43.4 mm, Cs: 0.5 mm, temperature: 300 K, Cc: 1.1 mm, convergence angle: 8.5 mrad, dE: 0.8 eV, dwell time: 15.7  $\mu\text{s}$ , and detector inner and outer angles: 60 and 200 mrad, respectively. A total of 30 thermal diffuse scattering (TDS) configurations were averaged to compute the final image that was viewed with an oversampling of 7 and an assumed source

size of 1.3 Å. The final image was from a ~ 3.7 nm thick section, and Poisson (shot) noise was added.

1. Sears, V. F.; Shelley, S. A., Debye-Waller Factor for Elemental Crystals. *Acta Crystallogr. Sect. A* **1991**, *47*, 441-446.

### **9.3 Addendum**

Due to limitations of the transmission electron microscope at NCSU, we were unable to conclusively determine whether the origin of behavior observed in Figure 8 is an effect of the NP composition or a thermodynamically driven phenomenon. A transmission electron microscope that could simultaneously visualize the atomic structure and acquire localized spectroscopic was required. Through the SHaRE (Shared Research Equipment) user facility at Oak Ridge National Laboratory, access was granted to use one of their transmission electron microscopes with the necessary capabilities to address this issue.

#### **9.3.1 Methods**

The same approximately equimolar ( $\text{Fe}_{47}\text{Pt}_{53}$ ) sample introduced previously was analyzed with a JEOL 2200FS TEM/STEM equipped with a CEOS aberration corrector (on the probe forming side). The microscope was operated at 200 kV in STEM mode. For image acquisition, the probe size was  $\sim 1 \text{ \AA}$ , and a HAADF detector was used. For acquiring EDS data, a Bruker-AXS X-Flash 5030 silicon drift detector was used, the probe and beam current were both larger. The EDS data were quantified using a standardless routine in the Bruker software suite.

#### **9.3.2 Results and Discussion**

EDS data were collected from NPs that were mixed phase  $\text{FePt L1}_0/\text{FePt}_3 \text{ L1}_2$ , as well as from the surrounding NPs, even if their phase could not be determined. A total of 26 NPs were measured, for which the results of which are shown in Figure 9. The measurements

support previous reports that a distribution of individual NP compositions exist when Fe and Pt precursors simultaneously decompose.<sup>4,5</sup> The average composition was 57.7 atomic percent Pt ( $\sigma = 3.8 \%$ ), and there was no apparent relationship between NP diameter and composition. This average composition is different from the ICP-OES value of 53 atomic percent Pt. This may be a result of the quantification process or the relatively small sample size. Regardless, a clear trend was present in the data which revealed then origin of the mixed phase,  $L1_0/L1_2$ , NPs.

The average composition of the NPs whose phase could not be determined was 56.5 atomic percent Pt ( $\sigma = 3.1 \%$ ). Since the phase was unknown, it is conceivable that NPs containing the  $L1_2$  phase were present in this subset of NPs. By comparison the average composition of the NPs that were known to contain some of the Pt-rich  $L1_2$  phase was 61.7 atomic percent Pt ( $\sigma = 3.3 \%$ ). A collage of images of this latter set of Pt-rich NPs is shown in Figure 10. The images show varying proportions of the  $L1_2$  phase present. Within this subset of NPs the NPs that contain the lowest amount of Pt generally have the lowest proportion of the  $L1_2$  phase, while the NPs with the most Pt are primarily  $L1_2$  phase NPs. These results support the hypothesis that the mixed phased NPs are a result of the distribution of individual NP compositions and not a thermodynamic phenomenon related to the preferential surface segregation of Pt interfering with the formation of the  $L1_0$  phase.<sup>6,7</sup> NPs that exhibited the  $L1_2$  phase were enriched with Pt in comparison to average over all 26 NPs.

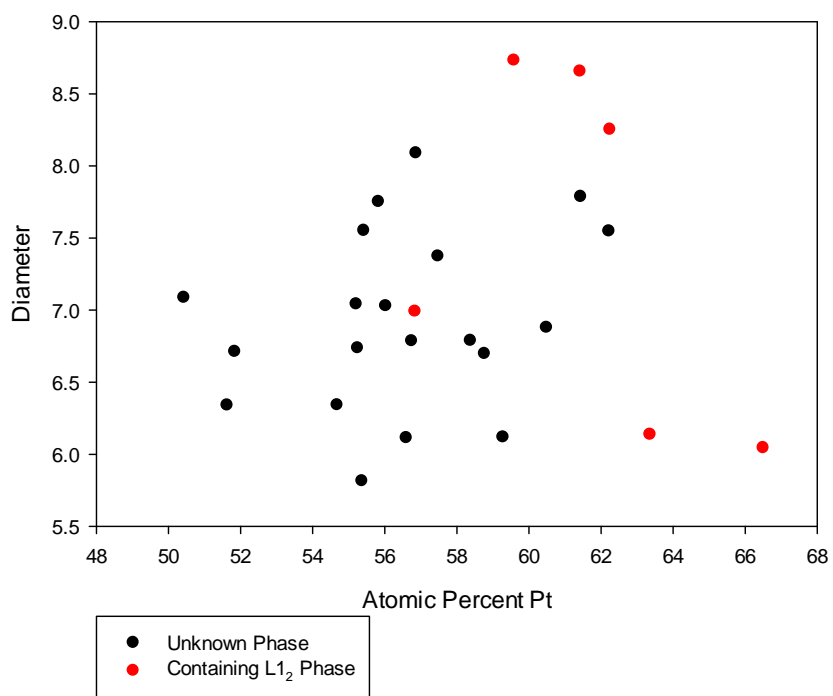


**Figure 9.** A plot of nanoparticle diameter versus composition. The data points in red are those nanoparticles that contain the Pt-rich L<sub>12</sub> phase, while those in black could not have their phase identified because they were not oriented on a zone axis.

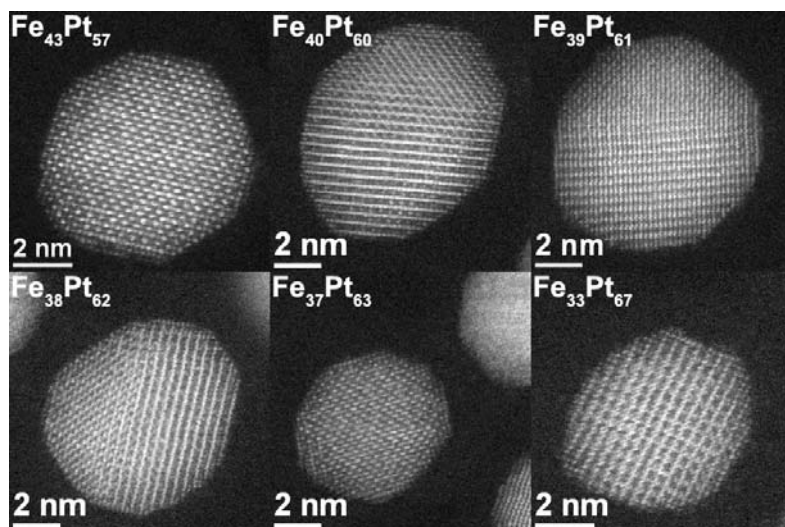


**Figure 10.** Atomic resolution HAADF-STEM images of FePt nanoparticles that contain the Pt-rich L<sub>12</sub> phase. The individual nanoparticle composition is listed with each image.

#### 9.4 Conclusions

The structure and composition of individual phase-converted FePt NPs were investigated using aberration corrected HAADF-STEM and EDS. HAADF-STEM showed the presence of mixed-phase NPs that contain both the L<sub>10</sub> and Pt-rich L<sub>12</sub> intermetallic phases of FePt. EDS results indicate a distribution of individual NP compositions, which leads to the formation of mixed-phase NPs. Phase conversion of chemically-synthesized NPs will likely produce some mixed-phase NPs, even if the ensemble average composition predicts formation of the L<sub>10</sub> phase only. Pure, L<sub>10</sub>-phase NPs are expected to form over a window of compositions (41-57 atomic percent Fe), which can be narrower than the range of compositions expected for chemically-synthesized NPs. This study conclusively shows that precise compositional control during the synthetic process is crucial for producing a product with a homogenous L<sub>10</sub> phase, which is required for NPs to be used in BPM. New synthetic

procedures need to be developed that allow for control of the ensemble average, as well as produce a very narrow distribution of individual NP compositions. Ideally, there would be no composition distribution.

## **9.5 Acknowledgements**

We would like to thank David Cullen (ORNL) for operating the microscope and analyzing and compiling the EDS data. This research was supported in part by Oak Ridge National Laboratory's SHaRE User Facility, which is sponsored by the Scientific User Facilities Division, Office of Basic Energy Sciences, U.S. Department of Energy.

## REFERENCES

- <sup>1</sup> M. F. Sarac, R. M. Wilson, A. C. Johnston-Peck, J. Wang, R. Pearce, K. L. Klein, A. V. Melechko, and J. B. Tracy, *ACS Applied Materials & Interfaces* **3**, 936 (2011).
- <sup>2</sup> X. Wang, P. J. Krommenhoek, P. D. Bradford, B. Gong, J. B. Tracy, G. N. Parsons, T.-J. M. Luo, and Y. T. Zhu, *ACS Appl. Mater. Interfaces*, (2011).
- <sup>3</sup> H. Feng, J. L. Lu, P. C. Stair, and J. W. Elam, *Catalysis Letters* **141**, 512 (2011).
- <sup>4</sup> S. Chandan, E. N. David, and B. T. Gregory, *Journal of Applied Physics* **104**, 104314 (2008).
- <sup>5</sup> C. C. Y. Andrew, M. Mizuno, Y. Sasaki, and H. Kondo, *Journal of Applied Physics* **85**, 6242 (2004).
- <sup>6</sup> B. Yang, M. Asta, O. N. Mryasov, T. J. Klemmer, and R. W. Chantrell, *Acta Materialia* **54**, 4201 (2006).
- <sup>7</sup> M. Müller and K. Albe, *Physical Review B* **72**, 10 (2005).

## CHAPTER 10

### **Phase Transformation of Alumina-Coated FePt Nanoparticles**

The following has been accepted for publication in *J. Appl. Phys.* (as an article in the 2011 Conference on Magnetism and Magnetic Materials proceedings) as “Phase Transformation of Alumina-Coated FePt Nanoparticles” by Aaron C. Johnston-Peck and Joseph B. Tracy. Johnston-Peck’s contribution to the research included synthesizing the FePt NPs, assembling the NP monolayers, depositing the alumina films, heat treating the samples, collecting and analyzing the TEM data, and writing the manuscript.

#### **10.1 Motivation**

As a continuation of the work presented in Chapter 9, the generality of the technique developed was investigated. Extending this technique of creating monolayers of FePt NPs and embedding in alumina to different kinds of NP, deposition processes, and coating materials would make a wide range of potentially useful materials available for various disciplines. Here the deposition technique, was the specific focus. Instead of using ALD, the thin alumina film was deposited by pulsed laser deposition (PLD).

In this research, alloy phase FePt NPs were synthesized and self-assembled into an ordered monolayer. Coating alumina deposited by PLD and subsequent thermal annealing converted the NPs into the intermetallic phase, while maintaining the NP size and the order of the monolayer array.

## 10.2 Abstract

Monolayers of FePt nanoparticles (NPs) were coated with 10 nm-thick layers of Al<sub>2</sub>O<sub>3</sub> by pulsed laser deposition (PLD). The Al<sub>2</sub>O<sub>3</sub> coating prevents diffusion and stabilizes the NP monolayer against sintering. Annealing converts the FePt NPs from an alloy phase (A1) into intermetallic phases. Atomic resolution high-angle annular dark-field scanning transmission electron microscopy (HAADF-STEM) shows that Pt-rich A1 Fe<sub>29</sub>Pt<sub>71</sub> NPs convert into the FePt<sub>3</sub> L1<sub>2</sub> intermetallic phase upon annealing and develop faceted morphologies. HAADF-STEM also reveals the presence of structural defects and Pt-rich shells. These results, in conjunction with prior studies of Al<sub>2</sub>O<sub>3</sub> deposition by atomic layer deposition (ALD), demonstrate that coating arrays of FePt NPs with thin Al<sub>2</sub>O<sub>3</sub> films by PLD or ALD imparts thermal stability and provide comparable results.

## 10.3 Introduction

Areal densities greater than 15 Tbit/in<sup>2</sup> can potentially be achieved using bit-patterned media.<sup>1</sup> Intermetallic FePt nanoparticles with equimolar stoichiometry have the L1<sub>0</sub> structure that gives them extremely high magnetocrystalline anisotropy, which stabilizes their magnetization against thermal fluctuations (superparamagnetism) to diameters as low as 4 nm. Wet-chemical methods produce monodisperse, ligand-stabilized FePt NPs that can be patterned into monolayers through self-assembly<sup>2</sup> and can extend across regions in excess of cm<sup>2</sup>.<sup>3</sup> However, wet-chemical methods generally result in chemically-disordered, alloy (A1) FePt NPs whose magnetic properties are not useful for magnetic storage without conversion into the thermodynamically-favored L1<sub>0</sub> phase.

Annealing converts the A1 phase into intermetallic phases, depending on the composition ( $L1_0$  for equimolar composition or  $L1_2$  for  $FePt_3$  or  $Fe_3Pt$  composition), but the NPs coalesce if no special precautions are taken.<sup>4</sup> Several approaches have been developed for the phase conversion of FePt NPs with minimal sintering.<sup>5-7</sup> We recently reported the atomic layer deposition (ALD) of thin, amorphous  $Al_2O_3$  films on monolayers of FePt NPs supported on SiN membranes.<sup>8</sup> The  $Al_2O_3$  coating serves as a diffusion barrier that prevents the NPs from agglomerating and coalescing, while allowing conversion into the  $L1_0$  or  $L1_2$  phases and facilitating characterization by TEM using the SiN membrane. The group of Kong *et al.* also recently reported closely related results when coating FePt NPs deposited on Si wafers with  $Al_2O_3$  thin films by ALD.<sup>9</sup>

Here, we have use pulsed laser deposition (PLD) for deposition of the  $Al_2O_3$  coating to demonstrate the generality of this approach. In comparison to ALD, PLD has higher deposition rates and is also useful for depositing a wide range of materials.<sup>10</sup>  $Al_2O_3$  deposited by PLD also eliminates sintering between NPs at elevated temperatures. Monolayers of FePt NPs were formed on SiN membranes and subsequently coated in amorphous  $Al_2O_3$  by PLD. Annealing drives conversion of the A1 FePt NPs into the  $FePt_3$   $L1_2$  intermetallic phase. The  $Al_2O_3$  barrier prevents sintering between NPs and maintains translational order within the monolayers. Measurements by high-angle annular dark-field scanning transmission electron microscopy (HAADF-STEM) provide insight into phase transformations within single NPs and reveal unanticipated structures after annealing that are potentially technologically significant.

## 10.4 Experimental Methods

FePt NPs were synthesized by modifying a method reported by Sun, et al.<sup>11</sup> The synthesis was performed using standard airless procedures and commercial reagents without further purification: 200 mg (0.5 mmol) platinum(II) acetylacetonate (97 %, Sigma Aldrich) and 20.0 mL benzyl ether (99%, Acros) were combined in a 100 mL three-necked, round-bottomed flask with a magnetic stir bar. The contents of the flask were degassed for 90 min at room temperature before backfilling with N<sub>2</sub> and heating to 100 °C. Immediately upon reaching 100 °C, 4.0 mL (12.5 mmol) oleic acid (99%, Alfa Aesar), 3.5 mL (10.3 mmol) oleylamine (97%, Acros), and 135 μL (1 mmol) iron pentacarbonyl (99.5%, Alfa Aesar) were added by syringe. The temperature was increased at a rate of 3 °C/min to 200 °C for 2.5 h. The NPs were purified by adding methanol and centrifuging, followed by redispersion in hexanes.

NPs suspended in hexanes (~1 wt%) were drop cast onto SiN membranes (DuraSiN DTF-05523) supplied by Protochips, Inc. The as-received membranes were first treated in a Jelight Model 144-A ultraviolet light with ozone (UVO) cleaner operating at ambient atmosphere for 5 min. After depositing the FePt NPs, the SiN substrates were treated with UVO for another 5 min to remove the ligands and any residual organics. The FePt NP layers were then coated with thin amorphous Al<sub>2</sub>O<sub>3</sub> films via PLD. The deposition chamber was evacuated to a base pressure of  $1.0 \times 10^{-5}$  Torr, while an atmosphere of 20 mTorr Ar was maintained during growth. An Al<sub>2</sub>O<sub>3</sub> target was used, and a target-substrate distance of 9 cm was maintained. For deposition of 10 nm-thick Al<sub>2</sub>O<sub>3</sub> films, 1300 pulses of a KrF excimer laser ( $\lambda = 248$  nm,  $\tau = 20$  ns) with a pulse energy of 150 mJ were applied at a rate of 6 Hz. In

control experiments, the deposition rate was established by growing a thin  $\text{Al}_2\text{O}_3$  film on an Si(100) substrate with a native oxide layer, and measuring the film thickness with a Veeco Dektak 150 profilometer. The samples were annealed in a tube furnace under forming gas (5%  $\text{H}_2$  in 95%  $\text{N}_2$ ) in a step wise fashion, first at 650 °C for 3 h, then at 575 °C for 2.5 h, and finally at 500 °C for 2 h.

Bright-field TEM images and EDS were acquired on a JEOL 2000FX microscope operating at 200 kV. The NP average edge lengths were determined by manually measuring 150 NPs using Image J.<sup>12</sup> The Cliff-Lorimer method was used for quantification of the EDS data. HAADF-STEM images were acquired on a JEOL 2010F microscope operating at 200 kV.

## 10.5 Results and Discussion

Cuboid FePt NPs were synthesized with an average aspect ratio of 1.3 ( $\sigma = 0.3$ ), edge lengths of 7.7 nm ( $\sigma = 1.2$  nm), and composition of  $\text{Fe}_{29}\text{Pt}_{71}$ . The NPs were drop cast onto thermally-robust, electron-transparent SiN membranes. The NPs assembled into monolayers, but the coverage was variable and ranged from sub-monolayers to partial multilayers, where NPs were stacked on top of each other, as observed in TEM images of overlapping NPs (e.g., Figure 1a). The NP monolayers had short-range rather than long-range translational ordering, which may arise from the dropcasting process or the NP size and shape distributions, which can frustrate assembly.<sup>13</sup> The average interparticle spacing between the inorganic surfaces of the NPs is approximately 2-3 nm in close-packed regions.  $\text{Al}_2\text{O}_3$  thin films were deposited onto the NP monolayers by PLD, which gave a ~10 nm-thick film in a

control specimen.

TEM images of the FePt NP monolayers after different stages of processing are shown in Figure 1. After coating with  $\text{Al}_2\text{O}_3$  (panel b) the arrays were unchanged from before the coating was applied (panel a). After annealing (panel c), the NPs and the film morphology were preserved. In comparison, heating an uncoated array of FePt NPs causes extensive agglomeration and coalescence into larger NPs (panel d). Therefore, even after prolonged annealing, the  $\text{Al}_2\text{O}_3$  thin film prevents sintering and thereby maintains the translational order within the array.

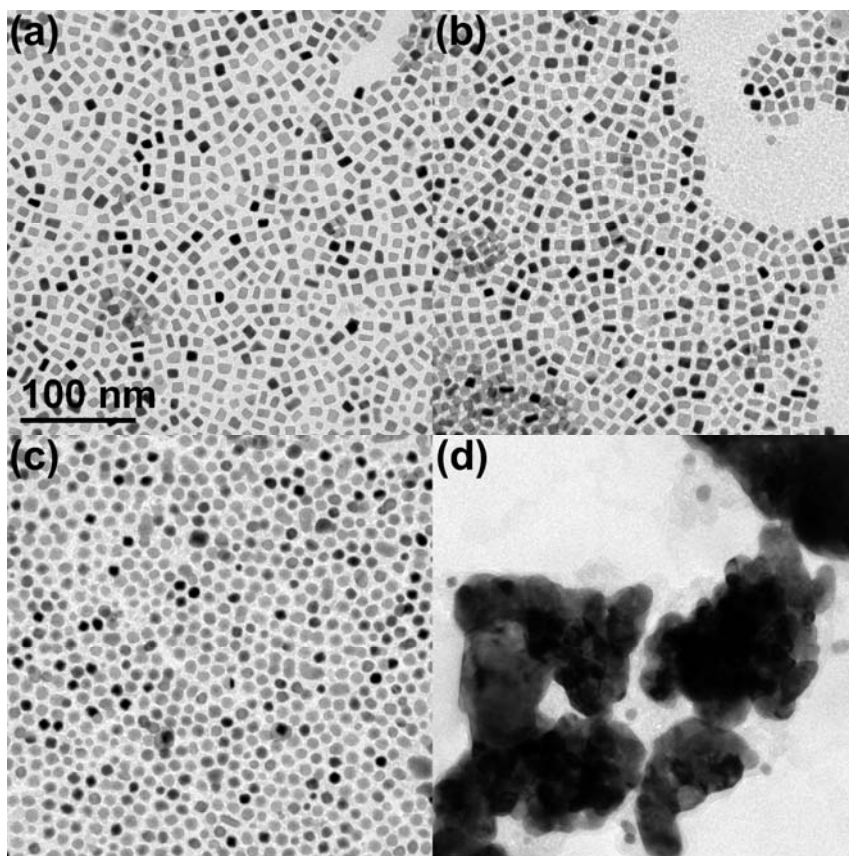


**Figure 1.** TEM images (common scale bar) of monolayers of FePt NPs: (a) before deposition of Al<sub>2</sub>O<sub>3</sub>, (b) with an Al<sub>2</sub>O<sub>3</sub> layer, before annealing, (c) with an Al<sub>2</sub>O<sub>3</sub> layer, after annealing (3 h at 650 °C + 2.5 h at 575 °C + 2 h at 500 °C), and (d) without an Al<sub>2</sub>O<sub>3</sub> layer, after annealing.

Heat treatment induces morphological changes in the FePt NPs. Prior to heating, the NPs are cuboids (projected as rectangles in the TEM images) with an average aspect ratio of 1.3 ( $\sigma = 0.3$ ) that decreases to 1.1 ( $\sigma = 0.1$ ) upon annealing, and the projections of the NPs become an approximately circular shape. Such restructuring was also observed in systems where the NPs were coated with Al<sub>2</sub>O<sub>3</sub> by ALD and likely results from reducing the surface energy when the NP-Al<sub>2</sub>O<sub>3</sub> interface relaxes.<sup>8</sup>

The  $\text{Al}_2\text{O}_3$  coating did not completely eliminate sintering between NPs, which agrees with our previous report.<sup>8</sup> Sintering among NPs that were stacked on top of each other was not prevented. The  $\text{Al}_2\text{O}_3$  film would be unable to grow between the stacked NPs because PLD is a line-of-sight deposition process. Stacked NPs fuse together because  $\text{Al}_2\text{O}_3$  cannot be deposited between them by PLD. Furthermore, stacked NPs were observed prior to heat treatment but rarely after annealing, which is consistent with the disappearance of stacking when the stacked NPs coalesce together. Another potential source of sintering could be residual ligands that were not removed prior to deposition of the  $\text{Al}_2\text{O}_3$  film and prevent complete coating of the NPs. This phenomenon was also observed in a related study that reported sintering of FePt NPs coated by a sputter-deposited layer of  $\text{SiO}_2$ , when the ligands were not completely removed prior to depositing the  $\text{SiO}_2$  layer.<sup>6</sup> Therefore, sintering can be completely eliminated for monolayers that are defect and ligand free.

Annealing causes restructuring of the NP morphology. Three faceted FePt NPs are shown in Figure 2. The morphologies identified were cuboctahedron (Figure 2a and 2c) and truncated octahedron (Figure 2b). From Figure 2, it is clear the cuboctahedron and truncated octahedron are similar in nature; both contain 14 faces, of which 6 are square and the remaining 8 are triangles and hexagons, respectively. The ratio of the edge lengths of the (100)-terminated facets to (110)-terminated facets is greater in the truncated octahedron structure, arising from the different ratios of the surface energies of the (100) and (110) surfaces as dictated by the Wulff construction.<sup>14</sup> The change in surface energies may result from differences in NP composition or differences in surface stress states due to local variations in the interactions with the  $\text{Al}_2\text{O}_3$  matrix, which would allow coexistence of both

morphologies.

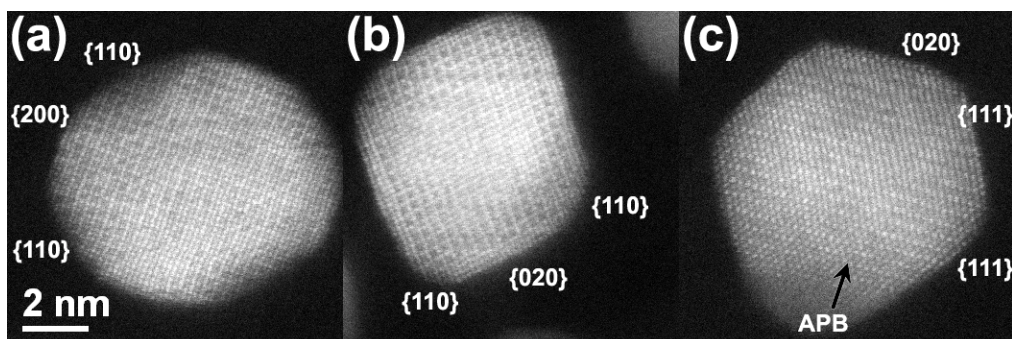


**Figure 2.** HAADF-STEM images (common scale bar) of FePt NPs after annealing: (a) cuboctahedron along [001], (b) truncated octahedron along [001], and (c) cuboctahedron along [101]. An antiphase boundary (planar defect) is indicated in the image, and surface steps are also present.

HAADF-STEM provides the unique ability to perform detailed structural and compositional characterization of individual NPs. For certain zone axes, HAADF-STEM images can be used for phase determination by means of line intensity profiles and fast Fourier transforms (FFTs) in conjunction with simulations using JEMS software.<sup>15</sup> Based on the Fe-Pt phase diagram, these NPs with average composition of  $\text{Fe}_{29}\text{Pt}_{71}$  would be expected to convert into the  $\text{FePt}_3$   $L1_2$  phase.<sup>16</sup> Conversion into the  $L1_2$  phase was generally observed, but there were also significant deviations from  $L1_2$  ordering. For example, in Figure 3, the central region of a NP (marked by a black square) remains in the A1 phase. Intensity profiles from the NPs in Figure 3 show that the NP surfaces are enriched in Pt, which was also observed for the NPs in Figure 2a and 2b (intensity profiles not reported.) For the NP with the [001] orientation in Figure 3, the atomic columns of a perfectly ordered  $L1_2$  structure

would consist solely of Fe or Pt. Therefore in this two-dimensional projection, an Fe atomic column will have 8 neighboring atomic columns of Pt, which appears in HAADF-STEM as a bright square (Pt) with a dark center (Fe), as depicted in the schematic in Figure 3.

Therefore, a measurement of the intensity of atomic columns along a line parallel to the edge of the NP ([100] or [010] direction) would have approximately equal intensity (Pt only columns) or oscillating intensity (alternating between columns of Fe and Pt atoms) after the background intensity is removed. Moreover, the line intensity profiles along neighboring rows of atomic columns should alternate between equal intensity (Pt only) and oscillating (alternating between columns of Fe and Pt). If line intensity profiles for adjacent rows of atomic columns contain only equal atomic column intensities, indicative of columns composed solely of Pt atoms, then that region of the NP can be assigned as an  $\text{FePt}_3 \text{ L}1_2$  phase with a high density of Pt antisite defects (Pt on the Fe sublattice), or simply as a Pt-enriched  $\text{FePt}_3 \text{ L}1_2$  phase. Intensity profile 1, along the edge of the NP, lacks oscillating column intensities, which implies that it is a row of Pt only columns. Therefore, within the  $\text{FePt}_3$  phase, the second and fourth rows of columns from the NP edge (intensity profiles 2 and 4, respectively) would be expected to contain alternating columns of Fe and Pt atoms because of the symmetry and periodicity of the unit cell. However, intensity profile 2 does not show the expected oscillating intensity that is present in intensity profile 4. Therefore, in the second row, the atomic columns of Fe atoms have been partially or wholly replaced by Pt atoms, indicating the presence of a large number of antisite defects, where Pt atoms take the place of Fe atoms. The enrichment of Pt at the surface is likely driven by surface effects that favor having Pt atoms at or near the surface of the NP, such as reduced surface energy or

strain relaxation.<sup>17-20</sup> While potentially of interest for catalysis, these surface effects may complicate ordering and are likely deleterious to the magnetic properties. Diffusion of Pt to the NP surface upon annealing, which has been modeled<sup>18</sup> and observed experimentally,<sup>19,20</sup> can decrease long-range ordering and inhibits the formation of perfectly-ordered NPs if Pt surface enrichment depletes other regions of the NPs such that the Fe:Pt ratio is no longer stoichiometric.<sup>21,22</sup>

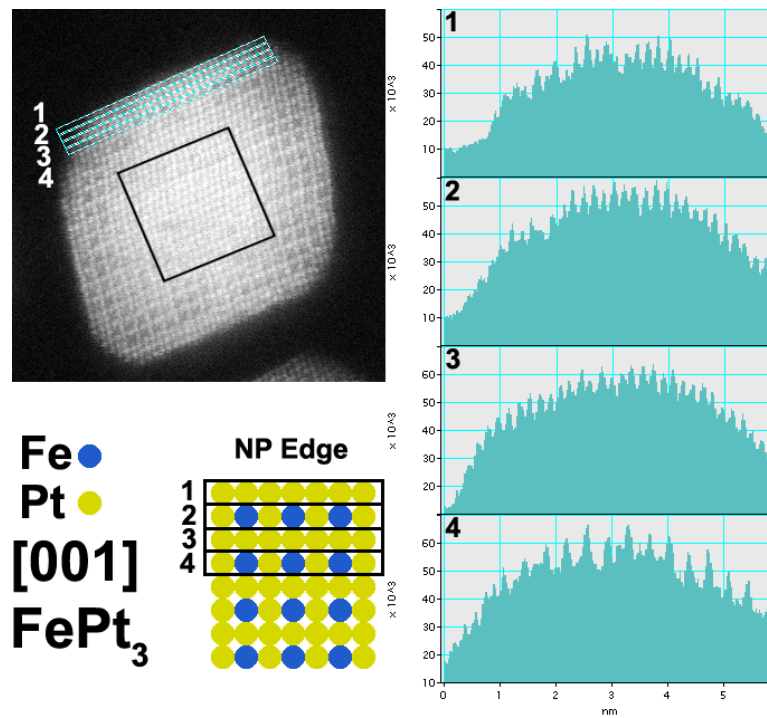


**Figure 3.** HAADF-STEM image with [001] zone axis of an FePt NP and line intensity profiles from rows of atomic columns parallel to the NP edge, beginning with the outermost row: (1) Pt atomic columns only, (2) alternating Fe and Pt atomic columns, containing a high density of Pt antisite defects, (3) Pt atomic columns only, and (4) alternating Fe and Pt atomic columns with few or no Pt antisite defects. The schematic shows the projection of the  $L1_2$  FePt structure along the [001] zone axis without the presence of any defects and indicates the anticipated pattern of atomic columns in the line intensity profiles.

## 10.6 Conclusions

Layers of FePt NPs were coated with thin Al<sub>2</sub>O<sub>3</sub> films by PLD. The Al<sub>2</sub>O<sub>3</sub> barriers prevent diffusion and sintering between NPs and preserve their assembly. Annealing provides the necessary energy for intraparticle atomic diffusion, and the FePt NPs transform from the A1 alloy into the thermodynamically-stable FePt<sub>3</sub> L<sub>12</sub> intermetallic phase. If FePt NPs of equimolar composition were used in this approach, monolayers of L<sub>10</sub> FePt NPs could be produced, which are of significant interest for bit-patterned magnetic media. HAADF-STEM imaging confirms that the Fe<sub>29</sub>Pt<sub>71</sub> NPs transform into the L<sub>12</sub> phase and reveals diverse structures that include Pt-rich shells and incompletely converted A1 cores. The Pt-rich shells may also enhance the catalytic activity of the NPs.

In summary, overcoating FePt NP arrays with Al<sub>2</sub>O<sub>3</sub> films deposited by either ALD or PLD can impart thermal stability against sintering. This approach can likely be extended to other deposition techniques, as well as to other refractory materials that could serve as sinter barriers.

## 10.7 Acknowledgments

This work was supported by the National Science Foundation (CHE-0943975 and CBET-1034374) and startup funds from North Carolina State University. A.C.J.-P. acknowledges support from a GAANN fellowship. We thank Protochips, Inc. for donating the SiN membranes and Jon-Paul Maria for use of his PLD chamber and associated equipment and his students, Elizabeth A. Paisley and Nicole A. Estrich, for training and

assistance with the deposition equipment.

## REFERENCES

- <sup>1</sup> Z. Z. Bandic, D. Litvinov, and M. Rooks, *MRS Bulletin* **33**, 831 (2008).
- <sup>2</sup> S. H. Sun, *Advanced Materials* **18**, 393 (2006).
- <sup>3</sup> A. Dong, X. Ye, J. Chen, and C. B. Murray, *Nano Letters* **11**, 1804 (2011).
- <sup>4</sup> Z. R. Dai, S. H. Sun, and Z. L. Wang, *Nano Letters* **1**, 443 (2001).
- <sup>5</sup> K. Elkins, D. Li, N. Poudyal, V. Nandwana, Z. Q. Jin, K. H. Chen, and J. P. Liu, *Journal of Physics D-Applied Physics* **38**, 2306 (2005).
- <sup>6</sup> Y. Ding, S. A. Majetich, J. Kim, K. Barmak, H. Rollins, and P. Sides, *Journal of Magnetism and Magnetic Materials* **284**, 336 (2004).
- <sup>7</sup> H. B. Wang, M. J. Zhou, F. J. Yang, J. Wang, Y. Jiang, Y. Wang, H. Wang, and Q. Li, *Chemistry of Materials* **21**, 404 (2009).
- <sup>8</sup> A. C. Johnston-Peck, G. Scarel, J. Wang, G. N. Parsons, and J. B. Tracy, *Nanoscale*, Advance Article (2011).
- <sup>9</sup> J. Z. Kong, Y. P. Gong, X. F. Li, A. D. Li, J. L. Zhang, Q. Y. Yan, and D. Wu, *Journal of Materials Chemistry* **21**, 5046 (2011).
- <sup>10</sup> M. N. R. Ashfold, F. Claeysens, G. M. Fuge, and S. J. Henley, *Chemical Society Reviews* **33**, 23 (2004).
- <sup>11</sup> M. Chen, J. Kim, J. P. Liu, H. Fan, and S. Sun, *Journal of the American Chemical Society* **128**, 7132 (2006).
- <sup>12</sup> W. S. Rasband, ImageJ <http://rsb.info.nih.gov/ij/> (accessed November 1, 2010).
- <sup>13</sup> A. C. Johnston-Peck, J. Wang, and J. B. Tracy, *Langmuir* **27**, 5040 (2011).
- <sup>14</sup> P. A. Buffat, M. Flueli, R. Spycher, P. Stadelmann, and J. P. Borel, *Faraday Discussions* **92**, 173 (1991).
- <sup>15</sup> P. Stadelmann, *JEMS - Electron Microscopy Software Java Version* (1999-2011).
- <sup>16</sup> H. Okamoto, *Journal of Phase Equilibria and Diffusion* **25**, 395 (2004).
- <sup>17</sup> M. Müller and K. Albe, *Physical Review B* **72**, 094203 (2005).
- <sup>18</sup> G. Bozzolo, R. A. Lukaszew, and J. E. Garces, *Applied Physics Letters* **88**, 011915 (2006).
- <sup>19</sup> R. M. Wang, O. Dmitrieva, M. Farle, G. Dumpich, H. Q. Ye, H. Poppa, R. Kilaas, and C. Kisielowski, *Physical Review Letters* **100**, 017205 (2008).

<sup>20</sup>L. Y. Han, U. Wiedwald, B. Kuerbanjiang, and P. Ziemann, *Nanotechnology* **20**, 285706 (2009).

<sup>21</sup>J. M. Cowley, *Ultramicroscopy* **27**, 319 (1989).

<sup>22</sup>J. Y. Liu and L. F. Allard, *Microscopy and Microanalysis* **16**, 425 (2010).

## CHAPTER 11

### Conclusions and Recommendations for Further Work

#### 11.1 Summary of Conclusions

This work was motivated by the engineering challenges associated with BPM. In this dissertation, several different projects were presented, but all are connected to BPM. In the most basic terms, these projects address at least one of the three main challenges of BPM media, (1) how to make a bit (2) how to assembly an array of bits (3) how to control a bit's magnetic properties. Solutions and insight were provided to all three challenges, a summary of which follows:

- Size-controlled production of monodisperse Co NPs can be accomplished by varying the chain length of the linear carboxylic acid ligand used during synthesis. The chain length influences the reactivity of the ligand-metal complex intermediates that form, which controls the supersaturation level of the solution before nucleation and dictates the number of nuclei formed and the eventual size of the NPs after growth.
- Size-dependent magnetic behavior of Co(core)/CoO(shell) NPs was observed including the onset of exchange bias in small sizes. This dependence is a result of the changing structure (oxide shell thickness, core volume, Co/CoO interface) of the NPs.

- The size and shell oxide thickness of Ni(core)/NiO(shell) NPs can be controlled through synthetic reaction parameters and post synthesis oxidation routines.
- The magnetic properties of Ni(core)/NiO(shell) NPs are a function of size and oxide shell thickness. Additional oxidation reduces  $T_B$  due to the reduction in ferromagnetic core volume but enhances the  $H_C$  at low temperature from weak exchange bias. The exchange bias does not cause an exchange shift because the structure of the NiO renders the shells unable to support the interfacial pinning strength necessary for an exchange shift. Ordering is determined by NP size and shape and spin-casting conditions.
- Spin-casting is a technique for that can be used for the self-assembly of NP monolayers with coverage greater than square microns.
- Electron-transparent SiN membranes facilitate the assembly of NP monolayers and subsequent characterization by TEM. Image analysis techniques applied to TEM micrographs enable quantifiable analysis of the grain structure and defects in NP monolayers.
- A thin film of amorphous  $\text{Al}_2\text{O}_3$  deposited by either PLD or ALD onto monolayers of FePt NPs coated with a, prevents sintering and preserves assembly of the NPs at elevated temperatures.
- Annealing drives the conversion of  $\text{Al}_2\text{O}_3$ -encapsulated FePt NPs from the A1 alloy, into  $L1_0$  and  $L1_2$  intermetallic phases, depending on the composition.

- Wet-chemistry synthesized FePt NPs have a distribution of individual NP compositions. This distribution leads to the formation of mixed-phase NPs demonstrating the necessity of precise compositional control during the synthetic process if a product with a homogenous  $L1_0$  or  $L1_2$  phase is required.

## 11.2 Recommendations for Further Work

If FePt is to remain the material of choice for BPM, several processing improvements must be made. The compositional distribution of wet-chemistry synthesized FePt NPs needs to be improved; ideally there would not be a distribution but rather each NP would have the same composition. The use of a ligand that forms a metal complex of both Fe and Pt atoms or a novel precursor that initially contains both may narrow the NP composition distribution. Alternatively, microreactors show promise of being able to provide more precise synthetic control. Heat treatments that drive the phase conversion from the alloy to intermetallic phases should be optimized, such that maximum ordering is attained. This will involve a balance between sufficient thermal energy for diffusion while remaining below the order-disorder critical temperature.

Systematic studies of exchange bias on the nanoscale are needed to understand the structure-property relationships. A major challenge is limited ability to precisely and systemically control the size, morphology, etc. of NPs, especially in the case of wet-chemical approaches. For the purpose of establishing these relationships, more controllable techniques such as ALD, which can also be used to deposit transition metals may be more appropriate.

In general, studies to understand the microscopic mechanism of exchange bias would be beneficial. There have been numerous recent developments in the field of TEM that offer great potential to do so. These developments include in-situ holders (apply magnetic field and or electrical bias, heat or cool), direct electron detectors (shorter integration time, improved efficiency and dynamic range), and aberration correction (improved resolution and the potential of  $C_c$  correctors to function as a phase plate for direct imaging of magnetic phase shifts caused by the sample).